A GEOPHYSICAL INVESTIGATION OF THE GULF OF CORINTH, GREECE

A THESIS SUBMITTED TO THE GRADUATE DIVISION OF THE UNIVERSITY OF HAWAI'I IN PARTIAL FULFILLMENT OF THE REQUIREMENTS FOR THE DEGREE OF

MASTER OF SCIENCE

IN

GEOLOGY AND GEOPHYSICS

OCTOBER 2004

By
Jonathan R. Weiss

Thesis Committee:

Brian Taylor, Chairperson
Greg Moore
Steve Martel
Fernando Martinez

ACKNOWLEDGEMENTS

Thank you to my advisor, Dr. Brian Taylor. This project has been a long and sometimes bumpy road but you have guided and supported me through it all. Working with you has stoked my love for the earth sciences. I would like to express my sincere appreciation for contributions from Stephen Martel, Gregory Moore, and Fernando Martinez. I would like to thank Andrew Goodliffe for guidance and patience from day one. Thank you to Alfred Hirn, Maria Sachpazi, Aristofanis Stefatos, and Marie Laigle, without whom this work would not have been possible.

Additionally, I want to thank my family for their overwhelming love and support. Mom, I am fortunate that we are so much alike. Your strength and perseverance are inspiring. Dad, thank you for your advice. Nicholas, Alexander, and Zachary, although I am not there to watch you guys grow up, you are in my heart and mind every day. I love you tremendously.

Finally, thank you to my friends at SOEST who have made my time here in Hawaii unforgettable. You are an amazing bunch and I am excited for what the future holds!

שמע ישראל יהזה אלהינז יהזה אחד.

ABSTRACT

This study provides insight into the process of continental extension and rift basin formation by focusing on the structural geometry, faulting, and sedimentation in the Gulf of Corinth, Greece. The Gulf of Corinth, opening at a rate of 11-16 mm/yr, is the second fastest opening rift on the earth today and has been the locus of 11 Mb=5.0-6.1 earthquakes in the past 30 years, making it an important location for understanding processes related to rapid continental extension. I processed and interpreted a grid of ~50 multi-channel seismic profiles and multibeam bathymetry collected in the Gulf aboard R/V *Maurice Ewing* in the summer of 2001, the first comprehensive MCS investigation of the Gulf of Corinth.

Large-offset, intermediate angle (dips of 30°-50°), right-stepping en echelon to overlapping, north-dipping normal faults bound the southern Gulf margin. The faults are listric and become low-angle (dips of 19-33°) near the base of the synrift section and within the basement but are not imaged extending to depths greater than ~4 km. High angle (dips >50°) normal faults occur within the central basin and on its northern margin. Some of these faults controlled the early rift basin evolution and, in the west, some remain dominant structures today.

The synrift sediment thickness in the Gulf is no greater than 2.5 km, half that predicted by thick elastic plate models of rift flank uplift and footwall subsidence, which take into account sedimentation rates and changing marine levels [e.g. Armijo *et al.,* 1996]. The thickest sediment accumulations occur near

the center, and on the hanging walls, of the major faults. Strata typically exhibit normal drag against the faults. Additional thick sediments occur within hanging wall grabens on the crest of roll over anticlines and in the central basin.

Sediment delivery to the modern depocenter at 850-880 mbsl occurs from all sides: the low-relief northern margin, the subsidiary Gulf of Antikyra in the east, the high-relief southern margin, and by axial channels from the shallower and narrower western basin, but primarily from the latter two. Most rivers that originate many kilometers south of the coastline on the Peloponnesus Peninsula predate the current border fault configuration, maintain their courses, and incise deep canyons on the uplifted footwalls of the active border faults and on the submarine slope. However, Heliki fault footwall uplift redirects flow of the Kratis River towards the ramp between the en echelon Heliki and Derveni faults, which do not overlap. Stratigraphic patterns on the hanging wall of the eastern tip of the Heliki fault indicate lateral and vertical fault propagation similar to subaerial faults in the Suez rift [Gawthorpe *et al.,* 1997]. In general, processes related to faulting and sedimentation in the Gulf of Corinth are not dissimilar from other rift basins despite the unique forearc setting of the Gulf.

The MCS data do not directly image low- or high-angle faults penetrating the seismogenic zone at 6-15-km-depth beneath the Gulf. However, the observations from the Gulf of Corinth presented here contribute to our overall understanding of rift basin formation and emphasize that intermediate to low angle, listric normal faults are active in the Gulf and provide further evidence that low-angle faults are important structures that accommodate rapid extension.

TABLE OF CONTENTS

LIST OF TABLES

LIST OF FIGURES

1. Introduction

Since before the advent of plate tectonics, geologists have sought to understand processes related to extension of the earth's crust. Extension is associated with factors including far-field tectonic forces, gravitational collapse of over-thickened crust, extension of the upper plate above subduction zones, and in bends or steps between strike-slip faults. Extension leads to the formation of rift basins and rift systems where hydrocarbon preservation potential is high and in some cases to the formation of mid-ocean ridges, ocean basins and passive margins. Some rifting, however, does not proceed to ocean basin creation and leaves behind failed rifts. Research on a variety of topics related to rifting includes fault geometry and sedimentation pattern classification and numerical modeling of the mechanical evolution of rift systems. However, questions remain regarding many aspects of rift basin formation. This study attempts to provide insight into the process of continental extension and rift basin formation by investigating the structural geometry, faulting, and sedimentation in one of the most active continental rifts in the world, the Gulf of Corinth, Greece.

The Gulf of Corinth is an excellent place to study processes related to continental extension for a variety of reasons. Geodetic surveying reveals that the Aegean is one of the most rapidly extending continental rift systems in the world (~35 mm/yr) [*Abers*, 2001] and the Gulf is opening at rates approximately one third the Aegean total [*Reilinger et al.*, 1997]. Well-exposed normal faults with large vertical offsets and related synrift sediments exist on the rift flanks

[*Doutsos and Piper*, 1990]. In addition, both modern (last 30 years) and historical (since 480 B.C.) seismicity attest to the activity of the region [*Hatzfeld et al.*, 2000]. Recent studies of micro-seismicity [*Rigo et al.*, 1996] reveal the possible presence of an active, low-angle detachment fault beneath the Gulf, the mechanical feasibility of which has been highly debated in the literature [e.g. Wernicke, 1995]. Yet despite the ideal nature of the Gulf for the study of processes related to rifting, no thorough marine geophysical dataset had been collected prior to the R/V *Maurice Ewing* cruise in the summer of 2001 (EW0108). The purpose of EW0108 was to establish the mechanics of active continental extension from a seismic reflection survey by directly imaging the fault geometry with depth in order to distinguish between the wide variety of proposed deformational styles based on outcrop and seismicity evidence.

The first portion of this thesis is an overview of the tectonic setting of the Gulf of Corinth. Then, using a combination of high-resolution swath bathymetry and a 2-D grid of closely spaced multi-channel seismic (MCS) data, I first examine the morphology of the Gulf and discuss the complex network of on- and offshore drainage pathways and their interactions with the large basin-bounding and smaller synrift faults. I then present the seismic stratigraphy for the Gulf and divide the basin-fill sediments into a thick, early-rift section and a late-rift section composed of five distinct sequences. Next, I divide the Gulf into four segments based on variations in border fault, synrift fault, and sediment fill geometries. MCS lines from each segment clearly reveal that different structural geometries can be present within a single, relatively small rift system and that the rift

architecture can vary significantly over small distances. Subsequently, I review previous conceptual models of the Gulf of Corinth and evaluate these models in light of the MCS data. Finally, I present a new fault map of the Gulf and discuss sedimentation at the centers and ends of each of the border faults. These observations provide insight into the processes of faulting and sedimentation, which can be applied to the analysis of ancient and modern extensional basins, contribute to an overall understanding of the evolution of the Gulf, and further demonstrate the along strike variability and complexity that characterize the Gulf.

2. Tectonic Setting of the Gulf of Corinth

The Gulf of Corinth is located in the tectonically complex eastern Mediterranean region (Figure 2.1). Relative motion of the African and Eurasian Plates has dominated the history of this region since the late Paleozoic (250 Ma) when Greece lay at the western edge of the Gondwana supercontinent, adjacent to the Paleotethys Ocean [*Pe-Piper and Piper*, 2002]. Subduction along the southern margin of Eurasia destroyed this ocean. Subsequent Permian-to-Triassic rifting of the northern margin of Gondwana resulted in the opening of the eastern Mediterranean Neotethys Ocean [*Pe-Piper and Piper*, 2002]. Convergence of the African plate with Eurasia began in early Cretaceous time, creating alpine mountain ranges on the northern Mediterranean margin, thickened crust in the Aegean region, and westward-verging limestone nappes in central Greece [*Pe-Piper and Piper*, 2002].

Subsequent extension throughout the Mediterranean began synchronously in late Oligocene time (~30 Ma) and is probably related to a strong reduction in the absolute motion of Africa towards Eurasia, increasing African slab retreat and resulting extension of the upper (Eurasian) plate [*Jolivet and Faccenna*, 2000]. In the eastern Mediterranean, thinning of the crust in the Aegean brought this region under water by creating regularly spaced, east-west trending rift zones that extend onto mainland Greece and Turkey [*Armijo et al.*, 1996]. The Gulf of Corinth is a young rift in this well-established extensional setting and might be associated with the Northern Anatolia Fault propagating

southwestward into the Aegean at ~2-3 Ma, which caused faster extension and re-activated some segments of the earlier formed rift zones [*Armijo et al.*, 1996].

Global Positioning System (GPS) measurements help to constraint the kinematics of the eastern Mediterranean and the Gulf of Corinth. Investigations of current deformation of the region have used sites throughout Eurasia, Anatolia, and the Aegean Sea [*Jolivet*, 2001; *Le Pichon et al.*, 1995; *McClusky et al.*, 2000] and additional studies have focused on deformation in the Gulf of Corinth region [*Avallone et al.*, 2004; *Billiris et al.*, 1991; *Brace*, 1977; *Briole et al.*, 2000; *Clarke et al.*, 1997; *Le Pichon et al.*, 1995]. Figure 2.2 shows GPS horizontal velocities in a Eurasia-fixed reference frame [*McClusky et al.*, 2000]. Relative to Eurasia, the southern Aegean, including the Peloponnesus Peninsula, can be viewed as a coherent block moving southwest at a rate of 30 ± 1 mm/yr. The increase in velocity towards the trench (length of arrows in Figure 2.2) attests to the importance of slab rollback as subduction at the trench occurs faster than northward convergence of the African Plate and westward extrusion of Anatolia [*McClusky et al.*, 2000].

The north-south-directed displacement rate across the Gulf Corinth varies from 6-10 mm/yr in the east to 13-16 mm/yr in west [*Avallone et al.*, 2004; *Briole et al.*, 2000] resulting in an average displacement rate that is one-third of the 30±1 mm/yr of displacement measured across the entire Aegean region [*Jackson et al.*, 1982; *McClusky et al.*, 2000]. GPS measurements show that extension is concentrated in a band offshore that becomes as narrow as 10 km in the west near Aigion [*Avallone et al.*, 2004] and is more diffuse to the east [*Briole et al.*,

2000]. This has led authors to propose that although current displacement rates are greater in the west, the total amount of accumulated displacement is greater in the east [*Briole et al.*, 2000].

Figure 2.3 shows the locations of Holocene volcanoes in the Aegean region that define a volcanic arc typical of the upper plate above subduction zones. The Gulf of Corinth is located trench-ward of these volcanoes in a fore-arc position and represents fore-arc extension whereas rift basins north of the volcanic arc represent back-arc extension. Recent (1964-present) earthquakes are also shown to emphasize the current activity of the region and to illustrate the different styles of deformation associated with the tectonic plate boundaries (Figure 2.3). Earthquake focal mechanisms are from the HCMT catalogue and include thrust-related events associated with subduction north of the trench, strike-slip events associated with the Anatolian fault system, and extension-related earthquakes along the northern margin of the Gulf of Corinth.

Since ancient times destructive earthquakes occurred in the Gulf of Corinth and the locations of modern events supports the notion that deformation is currently concentrated along the boundaries of the Gulf (Figure 2.4, Table 2.1). In the last 30 years eleven major earthquakes (Mb ≥ 5.0) including the 1981 cluster of events have shaken the region (Figure 2.4). In the western Gulf, the 1965 (34°), 1970 (23°), 1992 (30°), and 1995 (33°) events are located at 7-10 km depth beneath the northern Gulf margin and are characterized by low-angle (23-34°), north-dipping nodal planes and a high-angle, south-dipping plane [*Rigo et al.*, 1996]. In the east, the 1981 cluster of events are located in and around the

Alkyonides sub-basin at 7-15 km depth, and characterized by steeper, north-dipping nodal planes (41-45°) (Figure 2.4, Table 2.1). Relocated micro-earthquakes along northward dipping planes have been cited as evidence for an active low-angle detachment in the central-western Gulf [*Rietbrock et al.*, 1996; *Rigo et al.*, 1996]. Analysis of refracted arrivals of seismic waves generated aboard EW0108 and received at seismic stations onshore seem to confirm the presence of a shallow, northward dipping interface beneath the Gulf [*Pi Alperin et al.*, 2004]. Hatzfeld (2000), however, suggests that the clusters of small events represent the brittle-ductile transition at 8-12 km depth and not an active low-angle fault.

In summary, the tectonic setting of the Gulf of Corinth is complex. Regional GPS measurements and seismicity confirm that the Aegean is one of the most active continental rift systems in the world [*Abers*, 2001]. The modern Gulf of Corinth, located in a fore-arc setting, accommodates nearly one-third of the 30±1 mm/yr measured displacement rate across the Aegean and is experiencing north-south directed extension due to a combination of “rollback” of the African Plate and extrusion of Anatolia to the southwest. GPS measurements reveal that the displacement rate increases from east to west across the Gulf. Earthquake focal mechanisms (Figure 2.2) suggest different styles of deformation affect the western and eastern Gulf. The locations of micro-earthquakes suggests the presence of an active low-angle detachment beneath the Gulf.

FIGURE CAPTIONS

Figure 2.1 Regional setting of the Gulf of Corinth showing major tectonic features in the eastern Mediterranean region. Currently, the African Plate subducts beneath the Eurasian and Anatolian Plates. The Dead Sea transform fault is a strike-slip boundary between the African and Arabian Plates. Extrusion of the Anatolian plate occurs along the Anatolian fault segments. The Hellenic Trench acts as a backstop for sediment accumulating on the Mediterranean Ridge. The Aegean Sea is currently extending. The Gulf of Corinth (boxed) is a young rift within this extensional setting.

Figure 2.2 Geodetically determined horizontal velocities (arrows) and their 95% confident ellipses for a Eurasia-fixed reference frame. GPS measurements are from McClusky et al., 2000. Relative to Eurasia, Anatolia and the southern Aegean, including the Peloponissos Peninsula (PP), is a coherent block moving southwest, away from Eurasia, at a rate of 30 ± 1 mm/yr. The factors contributing to the observed Anatolian motion include the southward migration of the Hellenic arc as subduction at the trench occurs faster than northward convergence of the African Plate [McClusky et al., 2000] and the southwestward extrusion of Anatolia along the North and East Anatolian Faults [Armijo et al., 1996]. The increase in measured velocities towards the trench (length of arrows) attests to the importance of the first factor. Tectonic features are the same as in Figure 2.1 and a velocity scale is in the bottom right hand corner of the plot.

Figure 2.3 Grayscale shaded relief map of recent seismicity (1964-present) and Holocene volcanism in the Aegean region. Focal mechanisms are from the HCMT catalogue and are color-coded. Events >40 km have blue compression regions whereas those <40 km have black compression regions. Most of the deep quakes are subduction related events. Volcanoes that define the volcanic arc typically found on the upper plate above subduction zones are red stars. The Gulf of Corinth is in a fore-arc position. The abundance of earthquakes attests to

the tectonic activity of the region. Note the large number of extension-related events along the northern margin of the Gulf of Corinth.

Figure 2.4 Shaded relief map of the Gulf of Corinth showing modern, recorded (focal mechanisms) and historical (white circles), large magnitude (Mb>5) earthquakes. North-dipping nodal planes in the western Gulf have lower dips than those in the western Gulf suggesting a variation in styles of deformation across the Gulf. The most recent large event, in June 1995, severely damaged the city of Aigion on the southern coast. Two thousand buildings were rebuilt. See Table 2.1 for source depths, magnitudes, focal plane information, and earthquake location references.

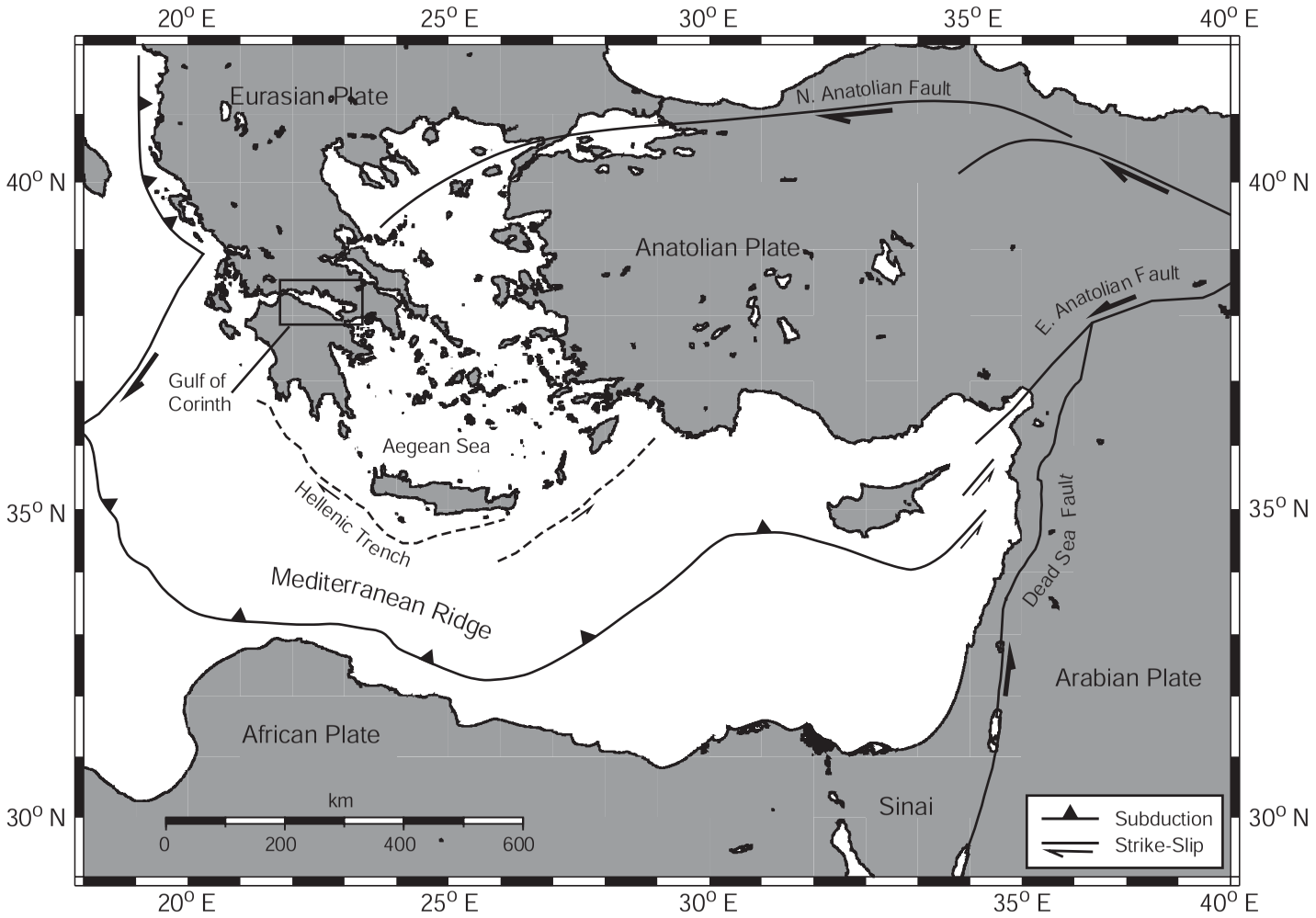
20° E
25° E
30° E
35° E
40° E
40° N
35° N
30° N
Eurasian Plate
N. Anatolian Fault
Anatolian Plate
E. Anatolian Fault
Gulf of Corinth
Aegean Sea
Hellenic Trench
Mediterranean Ridge
Dead Sea Fault
Arabian Plate
African Plate
Sinai
km
0
200
400
600
Subduction
Strike-Slip

Figure 2.1

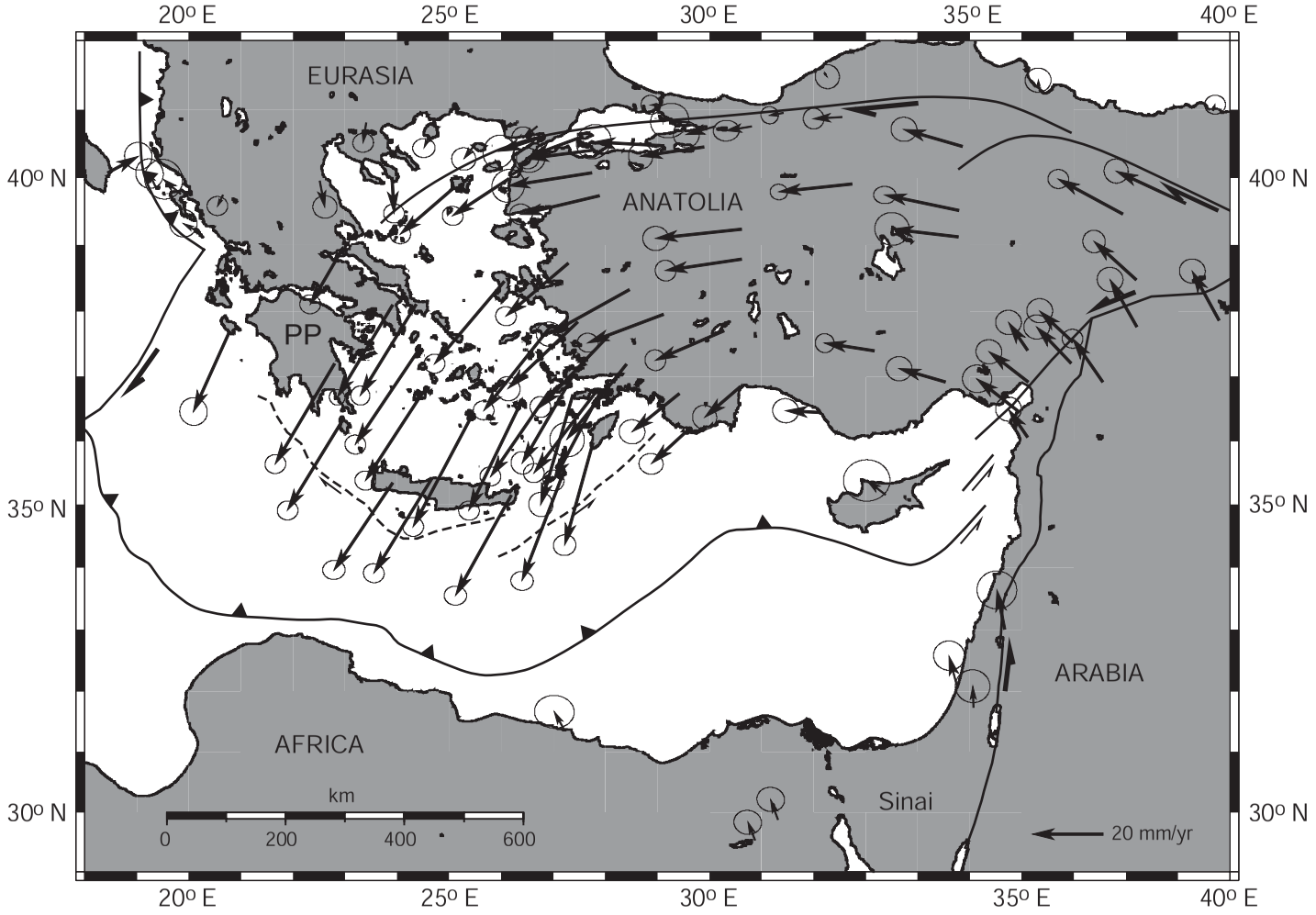
20º E
25º E
30º E
35º E
40º E
40º N
35º N
30º N
EURASIA
ANATOLIA
PP
ARABIA
AFRICA
Sinai
km
0
200
400
600
20 mm/yr

Figure 2.2

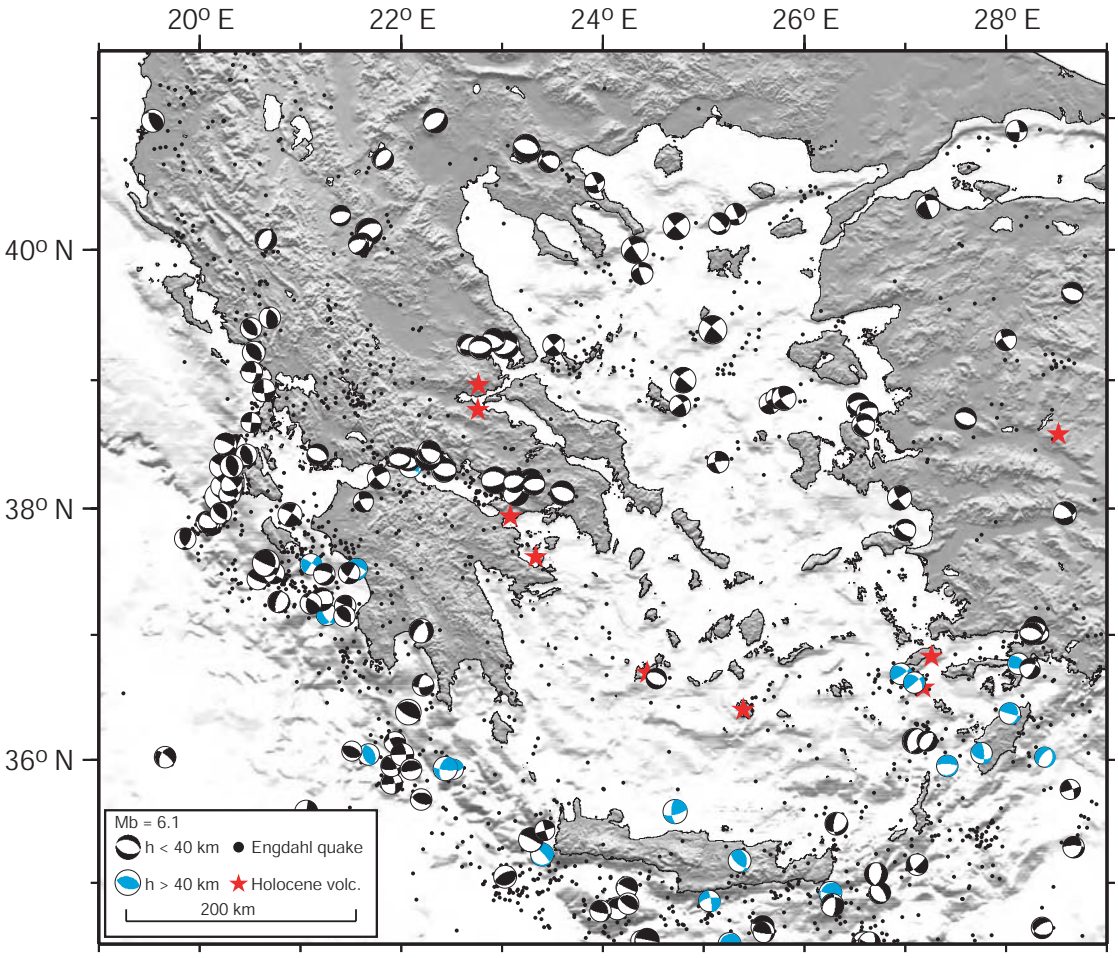
20º E
22º E
24º E
26º E
28º E
40º N
38º N
36º N
Mb = 6.1
h < 40 km
Engdahl quake
h > 40 km
Holocene volc.
200 km

Figure 2.3

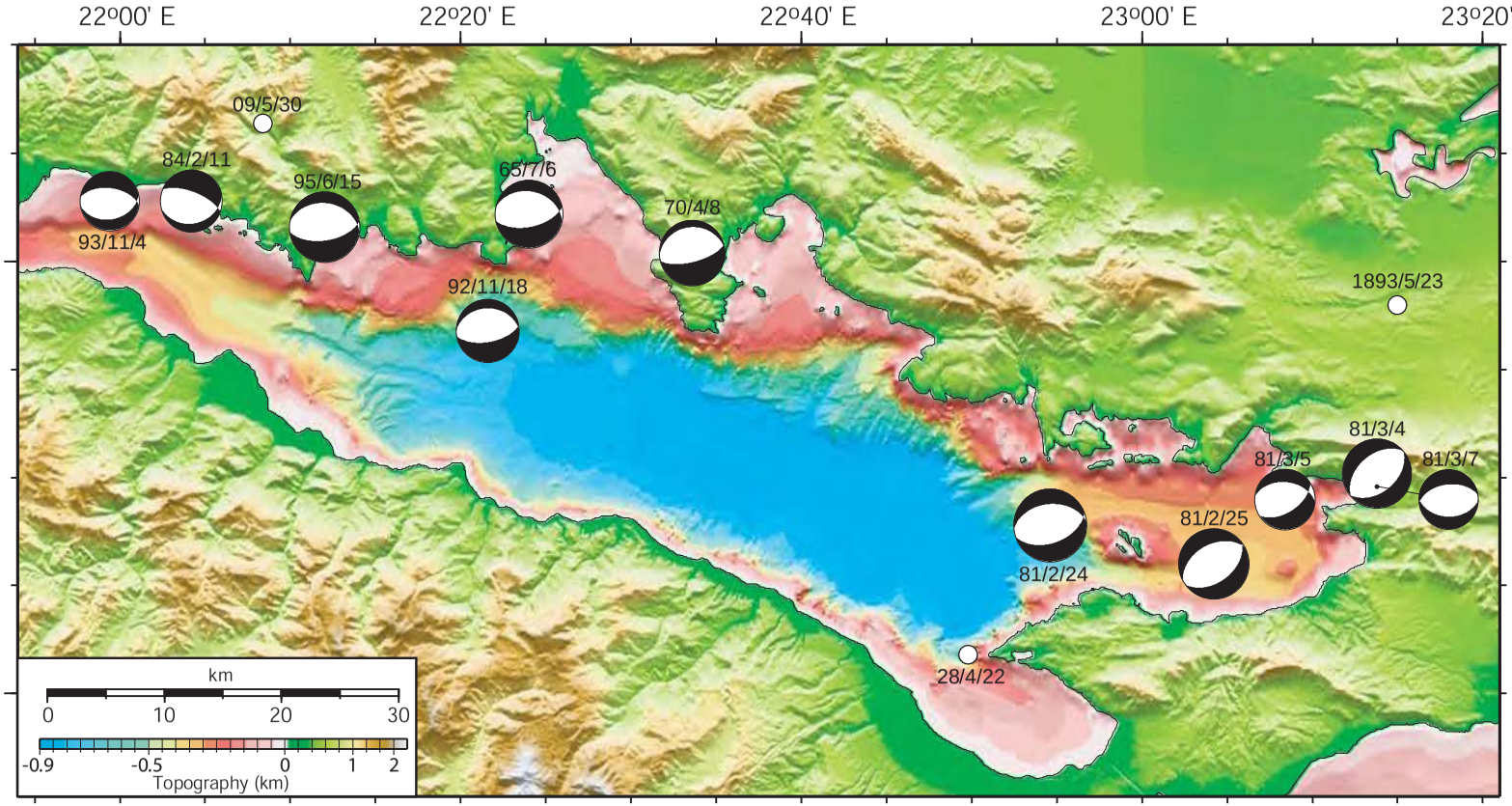
22º00' E
22º20' E
22º40' E
23º00' E
23º20' E
38º20' N
38º00' N
09/5/30
84/2/11
95/6/15
65/7/6
70/4/8
93/11/4
92/11/18
1893/5/23
81/3/4
81/3/5
81/3/7
81/2/25
81/2/24
28/4/22
km
0
10
20
30
-0.9
-0.5
0
1
2
Topography (km)

Figure 2.4

Table 2.1 Modern earthquakes in the Gulf of Corinth, Greece (Mb > 5.0).

Date (yyyy/mm/dd)	Lat (°N)	Lon (°E)	Mb	Ms	Mo (10^{16})	Mw*	Depth (km)	Strike	Dip	Rake	Slip Azimuth	Location Ref.	Solution Ref.
1893/05/23	38.30	23.25	-	6	-	-	10	270	45	-90	-	1	1
1909/05/30	38.44	22.14	6.9	6.3	-	-	10	30	74	-115	-	1	1
1914/10/17	38.34	23.46	-	6.2	-	-	10	100	45	-90	-	1	1
1928/04/22	38.03	22.83	6.4	6.3	-	-	9	285	40	-70	-	1	1
1930/04/17	37.82	23.06	-	5.9	-	-	6	270	45	-90	-	1	1
1965/07/06	38.37	22.40	5.8	6.4	167	6.08	10	281	34	-71	169	2	2
1970/04/08	38.34	22.56	5.8	6.2	91	5.91	9	265	23	-81	345	2	2
1981/02/24	38.13	22.91	6.1	6.7	875	6.56	12	264	42	-80	340	6	6
1981/02/25	38.10	23.08	5.7	6.4	397	6.33	8	241	44	-85	351	6	6
1981/03/04	38.17	23.23	5.8	6.3	270	6.22	7	50	45	-90	140	6	6
1981/03/05	38.15	23.14	5.3	5.3	18	5.43	15	276	43	-59	-	6	4
1981/03/07	38.16	23.24	5.4	5.4	15	5.38	15	91	41	-84	-	6	4
1984/02/11	38.38	22.07	5.3	5.5	33	5.61	15	77	28	-121	-	4	4
1992/11/18	38.28	22.36	5.9	5.7	90	5.68	7.4	270	30	-81	-	3	5
1993/11/04	38.38	21.99	5.1	5.2	11	5.29	9	79	37	-105	-	7	7
1995/06/15	38.36	22.20	6.0	6.2	390	6.33	10	277	33	-77	-	3	3

Mw*=(logMo-9.1)/1.5

References for earthquake hypocenters and focal mechanisms:

1. Ambraseys & Jackson, 1990
2. Baker, et. al, 1997
3. Bernard, et. al, 1997
4. Ekstrom & England, 1989
5. Hatzfeld, et. al, 1996
6. Taymaz, et. al, 1991
7. ISC & HCMT

3. Overview of the GOC Geology and Morphology

Geologic Setting

The NNW-trending Hellenic mountain chain, composed of nappe thrust sheets, is the dominant topographic feature spanning the length of Greece. East-west trending rift basins related to the current phase of Aegean extension, including the Gulf of Corinth, cut this topography obliquely. The Corinth Rift is the largest of these basins and the submarine portion occupies an area slightly larger than half of the entire rift [*Ori*, 1989; *Sorel*, 2000; *Stefatos et al.*, 2002]. The Gulf separates central Greece from the Peloponnesus Peninsula (PP in Figure 2.2). The Gulf communicates with the Mediterranean Sea through the narrow and shallow (~ 62 mbsl) Rio Straits in the west and with the Aegean Sea through the man-made Corinth Canal in the east (Figure 3.1).

Figure 3.2 is a simplified geologic map of the Gulf of Corinth showing major and minor faults and the extent of Pliocene-Quaternary rift-related sediments near the Gulf. The map highlights the variations between the northern and southern Gulf margins, the most noticeable of which is the asymmetric distribution of Pliocene-Quaternary synrift sediments. On the Peloponnesus Peninsula normal faults cut through the limestone basement and create over 3 km of structural relief from the Gulf of Corinth floor to Mt. Khelmos (2341 m) in the south (Figure 3.1). Most of these faults strike N90°E to N110° E, nearly perpendicular to the structural grain of the mountain chain. The faults are segmented along strike and in rare cases, terminate against faults that strike N-S

[*Doutsos and Piper*, 1990; *Doutsos and Poulimenos*, 1992; *Ghisetti and Vezzani*, 2004] (figure 3.2). Evidence including a down-dip decrease in fault dip, curved fault geometries in cross section, and back tilting and internal deformation of hanging wall blocks indicate that some of the major faults are listric [*Doutsos and Piper*, 1990; *Doutsos and Poulimenos*, 1992; *Ghisetti and Vezzani*, 2004]. In addition, many of the major faults, including the large, recently active border faults along the southern Gulf margin, are right-stepping en-echelon (Figure 3.2). Most of the faults on the PP are inactive and it is thought that both faulting and sedimentation have migrated northward and are currently focused beneath the Gulf [*Ori*, 1989; *Sorel*, 2000].

Previous workers have described the northern coast of the Gulf of Corinth as the down-flexed hanging wall to the major system of north-dipping faults on the south [*Brooks and Ferentinos*, 1984; *Heezen et al.*, 1966]. Despite the relative lack of synrift sediments (Figure 3.2), south-dipping faults along the northern margin of the Gulf are active, abundant [*Jackson et al.*, 1982; *Moretti et al.*, 2003] and have played a major role in the evolution of the Gulf. Many of the faults are offshore.

Additional and important contrasts between the northern and southern Gulf margins are the length of sediment delivery pathways (i.e., rivers) and the size of drainage areas (Figure 3.3). In simple half graben systems, the footwalls of the major border faults typically are drained by short rivers with small drainage areas, and the down-flexed, hanging wall is drained by long rivers with larger drainage basins [*Leeder and Jackson*, 1993]. In the Corinth Rift, however, the

case is not so simple. The southern margin is drained by long rivers such as the Selinus, Kratis, and Sithas Rivers, all of which originate many kilometers south of the Gulf margin in the uplifted footwalls of the oldest faults (Figure 3.3). Shorter rivers such as the Krios, Skoupeikos, and Agiortikos Rivers that originate only a few kilometers south of the Gulf margin also occur (Figure 3.3). Many of the river channels terminate at fan deltas at the Gulf edge or canyons on the steep submarine slope that in turn terminate in large submarine fans at the base of the slope.

With the exception of the Itea River (Figure 3.3), short rivers drain the headlands and peninsulas of the northern rift margin. The rivers end at long submarine channels where broad shelves are present. Otherwise, the rivers end at short channels, which incise canyons across the highly eroded and faulted submarine slope. Although not well imaged in the available bathymetric data, channels probably traverse the floors of the subsidiary Gulfs (Itea, Antikyra, Lechaio, and Alkyonides) before joining the canyons imaged >250 mbsl (Figures 3.1 and 3.3).

Submarine Morphology

The Gulf of Corinth stretches 130 km from the Alkyonides Gulf in the east to the Rio Straits in the west (Figure 3.1) and reaches a maximum width of ~30 km near Derveni (Figure 3.3A). The depth of the basin gradually increases from <100 meters below sea level (mbsl) at the Rio Straits eastward to >850 mbsl in the central-eastern Gulf (Figure 3.1). Three shallow sub-basins (the Gulfs of Lechaio, Itea, and Antikyra) reach maximum depths of ~200 mbsl (Figure 3.1).

The largest sub-basin, the Alkyonides Gulf, reaches depths >350 mbsl.

Previous studies have divided the Gulf floor into physiographic provinces including shelf, slope, rise and abyssal plain similar to that of the major ocean basins [*Heezen et al.*, 1966]. This convention simplifies discussions of specific locations on the seafloor. The shelf lies between sea level and ~200 mbsl and is narrow except in the subsidiary Gulfs of Itea and Antikyra. In the main basin (Figure 3.3A), the shelf is wide both southeast of Eratini and southeast of Aigion where large fan deltas are at the shoreline. Thin packages of sediment incised by channels and many small faults are present on the shelf (Figure 3.3B). Pre-rift basement structures oriented oblique to the trend of active faults are also present (not shown).

In the Gulf of Lechaio (Figure 3.1) MCS lines reveal a thick (~2 km) sediment package cut by large, ~EW-striking, south-dipping normal faults that offset the seafloor. It is difficult to correlate this package of sediment with that in the central Gulf due to the lack of age control on individual horizons within the sub-basin. However, the section is probably late Pleistocene-Holocene and related to the exposures in the Corinth Canal [*Collier*, 1990; *Collier et al.*, 1992].

The submarine slope lies between ~200 and ~750 mbsl and is steep and narrow along the southern margin and generally wider and more subdued along the northern margin except where headlands are present (Figure 3.3A). This difference was noted by early investigators [*Brooks and Ferentinos*, 1984; *Heezen et al.*, 1966] and attributed to the southern margin being on fault footwalls and the northern margin being on fault hanging walls.

Seafloor bathymetry (Figure 3.3A) illustrates the prominence of submarine canyons and channels on the submarine slope. The largest canyons are mostly associated with onshore rivers (Figure 3.3B) and are imaged in the MCS data as seafloor troughs. Rivers that do not have offshore canyons might not carry high enough concentrations of sediment to incise the submarine slope [*Ferentinos et al.*, 1988]. Large canyons along portions of the southern margin cross the border faults controlling the margin. Canyons and channels along the northern margin are more abundant and contribute to the heavily eroded appearance across much of the northern margin (Figure 3.3). Gullies are also prominent on both the northern and southern slopes.

The submarine rise lies between ~750 and ~850 mbsl and varies in width around the basin. The rise is created by the growth of broad submarine fans [*Ferentinos et al.*, 1988] that tend to coalesce at the base of the slope. The size and extent of the fans varies around the basin, but the largest are found adjacent to the southern margin on the hanging walls of the large border faults. On the northern slope, no large fans are present. Channels exploit gaps between faults, such as south of the Pangalos Peninsula, or erode and create breaks in the uplifted footwalls of faults blocks, such as along the Antikyra fault scarp (Figures 3.2 and 3.3B). Pathways also terminate against fault blocks or change direction as they encounter faulted topography. The best example occurs on the southern margin where the Kratis River changes course approaching the large Heliki border fault (Figure 3.3).

The slope and rise along the northern margin developed interdependently. The lack of large fans indicates that either sediment is dispersed over the entire basin floor rather than at the base of the slope and/or that not a large amount of sediment is entering the Gulf from the northern margin. The slope-rise morphology along the northern margin varies over time due to the growth of the large number of small faults there. Where faults are active, drainage is controlled by fault-related topography except when incision outpaces fault growth. When faults become inactive or where they are not present, the slope erodes.

The shelf-slope-rise in the west central Gulf differs from other parts of the basin and is modified by the presence of subaerial fan deltas composed of course-grained alluvium adjacent to the shoreline. These fans are developed on the hanging walls of the Aigion and Heliki Faults (Figures 3.2 and 3.3).The submarine slope in the west central Gulf is incised by a system of well-developed submarine canyons and channels that dominate the seafloor including a large axial channel that drains eastward to at least the 750-mbsl contour (Fiigure 3.3).

The shelf-slope-rise in the eastern Gulf (Figure 3.2) is unique in that two large canyons enter the main basin from the Alkyonides Gulf, one from north of the Alkyonides Islands and one from the south through the Strava graben, bounded on the south by the Strava fault [*Papatheodorou and Ferentinos*, 1993]. Both of these pathways are parallel to the major border faults and may be pathways through which sediment accesses the main basin from the east.

Generally, the abyssal plain is the portion of the Gulf >850 mbsl with the exception of the central Gulf where it begins at 800 mbsl. The abyssal plain is

nearly flat with a slight eastward slope and is the largest portion of the Gulf. The long axis of the abyssal plain strikes WNW, parallel to the southern Gulf margin, rather than parallel to the EW strike of major border faults. Fault scarps are rarely resolved in the bathymetric data at these depths.

FIGURE CAPTIONS

Figure 3.1 Three-dimensional perspective view of the Gulf of Corinth looking north from 45° elevation. Major features and locations referred to in the text are labeled. Vertical exaggeration = 4.

Figure 3.2 Simplified structure and geology of the Gulf of Corinth. Geology and onshore faults are from various authors. Submarine faults are from this study except for those bordering the subsidiary Alkyonides Gulf. AIG=Aigion fault; ANT=Antikyra fault; CB=Corinth Basin; DER=Derveni fault; DOM=Domvous fault; EAL=eastern Alkyonides fault; ERA=Eratini fault; HEL=Heliki fault; ITE=Itea fault; KAP=Kaparelli fault; KIA=Kiato fault; LOU=Loutraki fault; MB=Megara Basin; PER=Perahora fault; PSA=Psatha fault; PSP=Psathopyrgos fault; SIT=Sithas fault; WAL=western Alkyonides fault; XYL=Xylocastro fault.

Figure 3.3 Uninterpreted (A) and interpreted (B) shaded relief maps of the Gulf of Corinth. The area shown in Figure 3.3A is slightly smaller than in Figure 3.3B to provide a closer look at the bathymetric data collected aboard EW0108. Figure 3.3B includes major faults (same as in Figure 3.1) and drainage interpreted from the topographic and bathymetric data and from Landsat ETM+ images of central Greece. Major rivers are labeled.

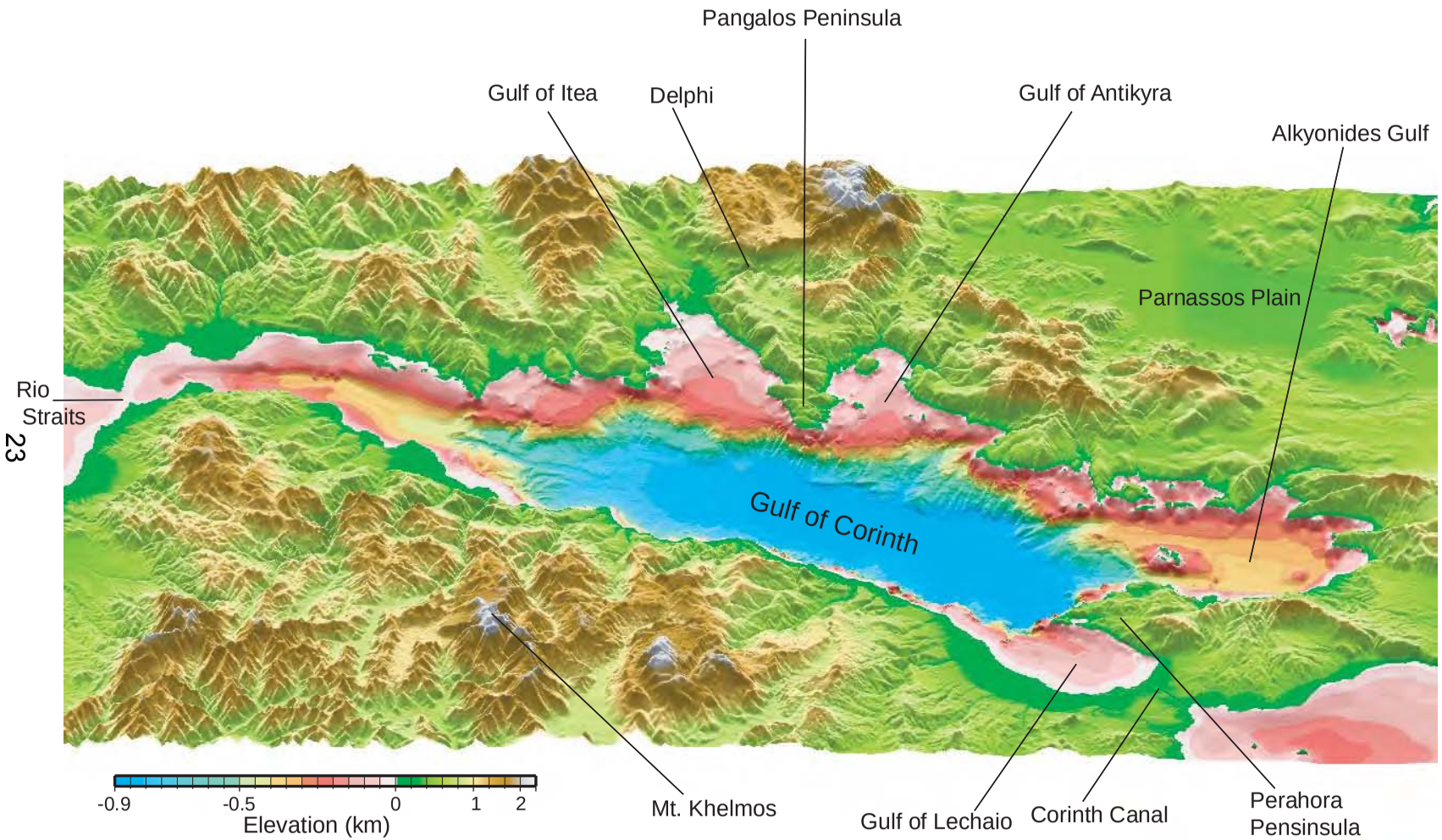
Pangalos Peninsula
Gulf of Itea
Delphi
Gulf of Antikyra
Alkyonides Gulf
Parnassos Plain
Rio
Straits
Gulf of Corinth
-0.9
-0.5
0
1
2
Elevation (km)
Mt. Khelmos
Gulf of Lechaio
Corinth Canal
Perahora
Pensinsula

Figure 3.1

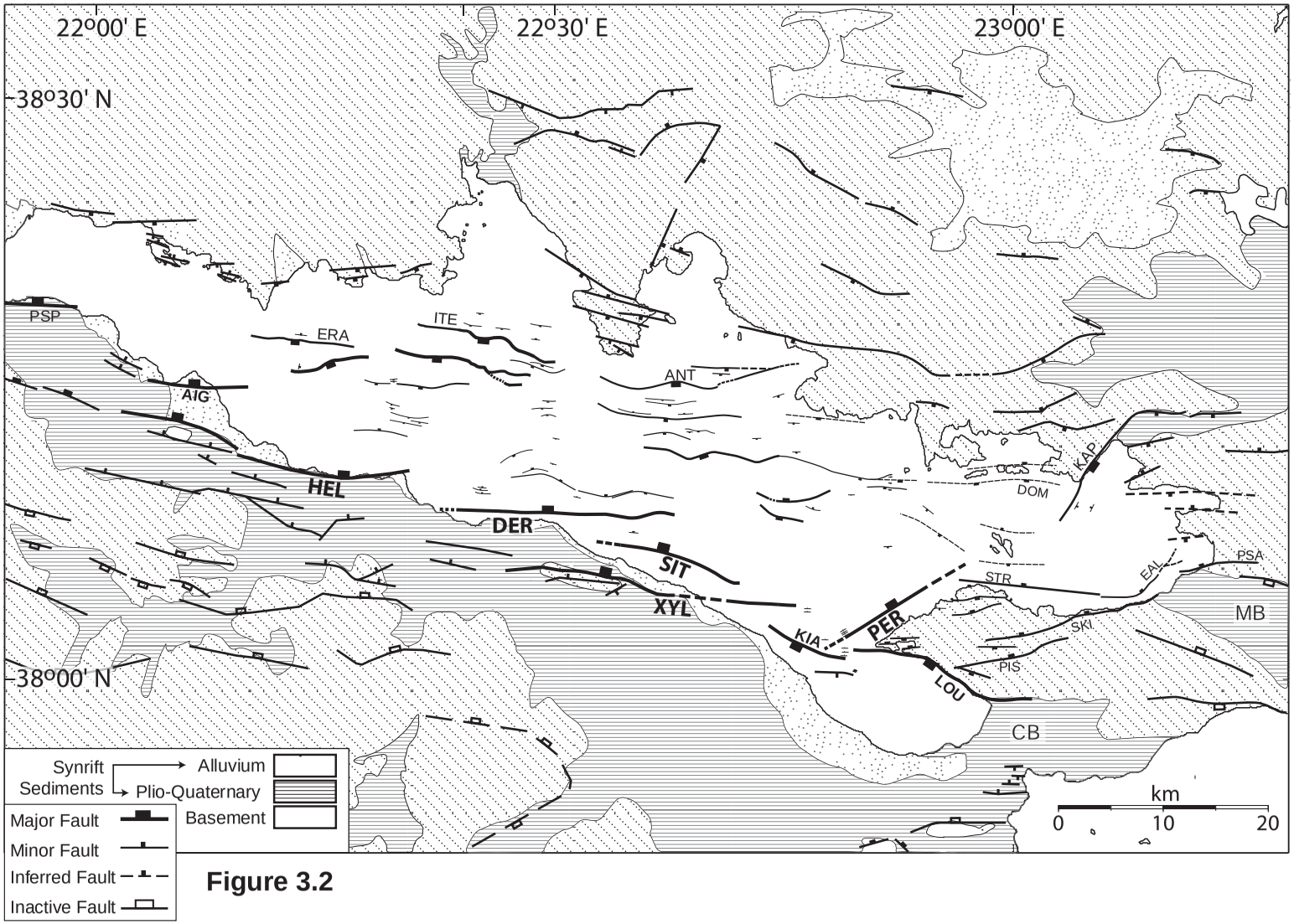
22°00' E
22°30' E
23°00' E
38°30' N
38°00' N
PSP
ERA
ITE
ANT
AIG
HEL
DER
SIT
XYL
KIA
PER
LOU
KAP
DOM
STR
EAL
PSA
SKI
PIS
MB
CB
km
0
10
20
Synrift Sediments
Alluvium
Plio-Quaternary
Basement
Major Fault
Minor Fault
Inferred Fault
Inactive Fault

Figure 3.2

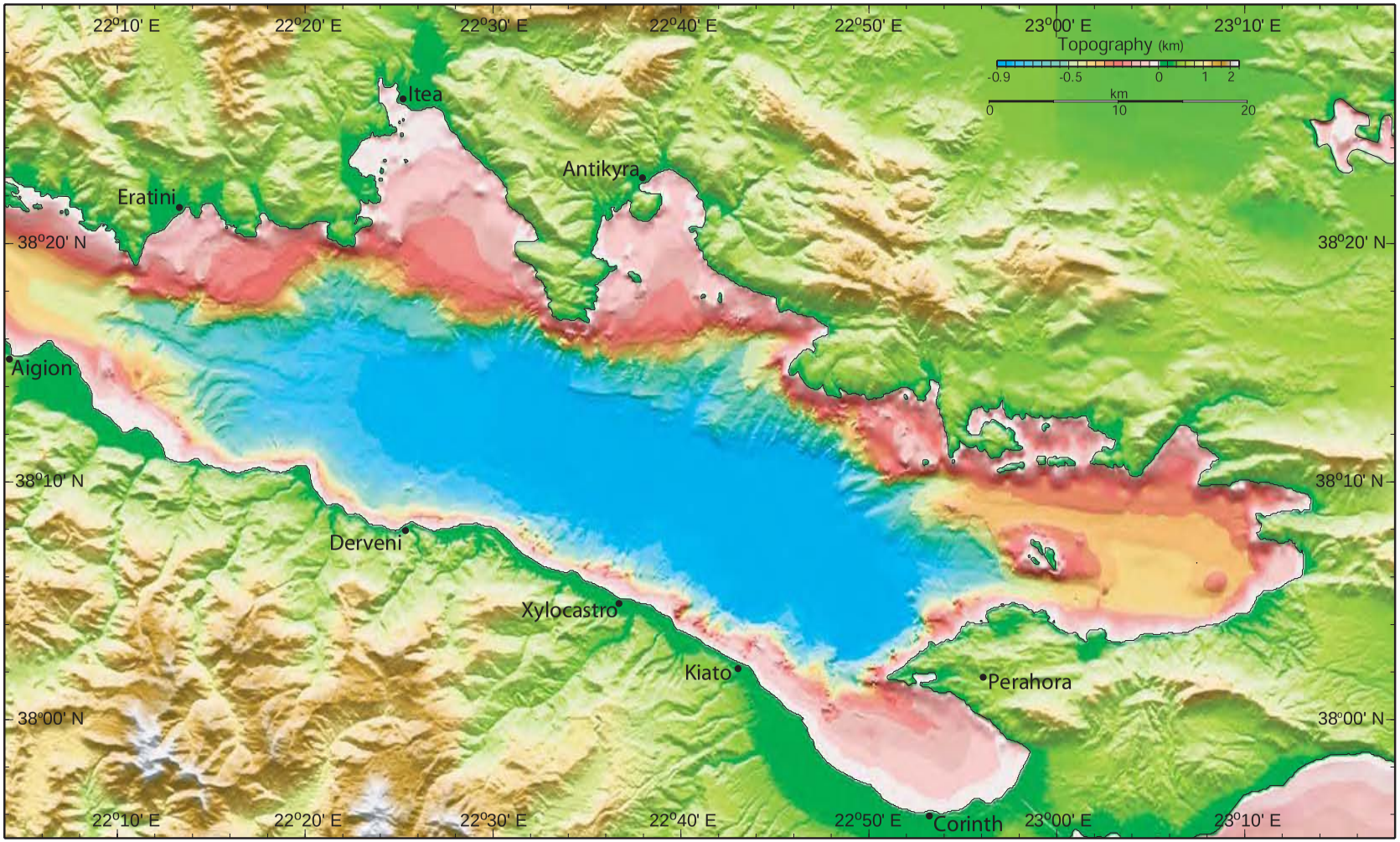
22°10' E
22°20' E
22°30' E
22°40' E
22°50' E
23°00' E
23°10' E
Topography (km)
-0.9
-0.5
0
1
2
km
0
10
20
Itea
Antikyra
Eratini
38°20' N
Aigion
38°10' N
Derveni
Xylocastro
Kiato
Perahora
38°00' N
Corinth

Figure 3.3A

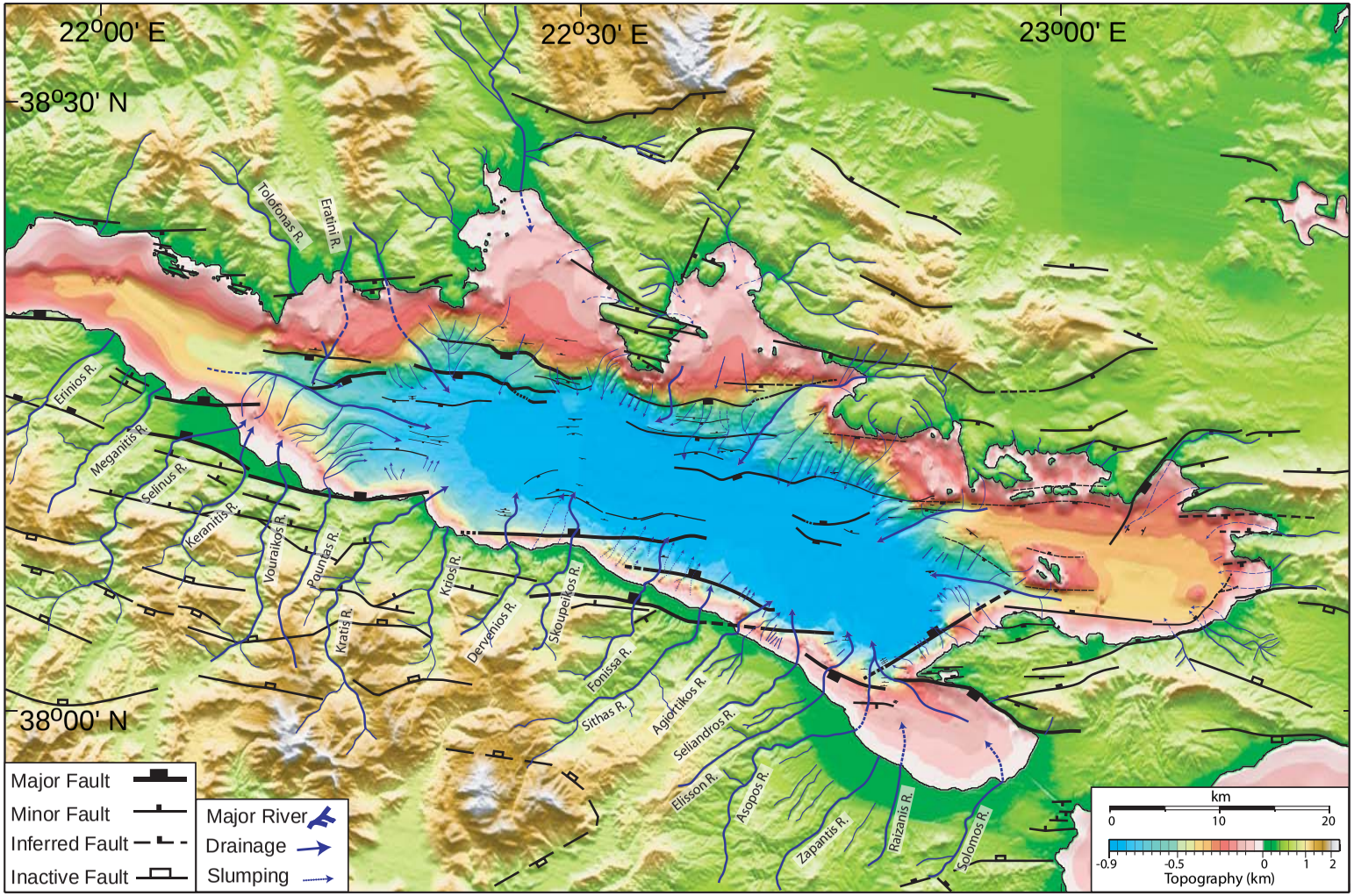
22°00' E
22°30' E
23°00' E
38°30' N
38°00' N
Tolofonas R.
Eratini R.
Erinios R.
Meganitis R.
Selinus R.
Keranitis R.
Vouraikos R.
Pounitas R.
Kratis R.
Krios R.
Derveñios R.
Skoupeikos R.
Fonissa R.
Sithas R.
Agiortikos R.
Seliandros R.
Elisson R.
Asopos R.
Zapantis R.
Raizanis R.
Solomos R.
Major Fault
Minor Fault
Inferred Fault
Inactive Fault
Major River
Drainage
Slumping
km
0
10
20
-0.9
-0.5
0
1
2
Topography (km)

Figure 3.3B

4. Seismic Stratigraphy

The basin fill in the Gulf of Corinth (GOC) is composed of a lower, early-rift sequence/section and an upper, late-rift sequence/section characterized by alternating semi-transparent and highly reflective acoustic units (4.1). Only the upper part of the early-rift section has these; below that are transparent to semi-transparent strata that vary spatially from horizontal and continuous to discontinuous and chaotic. Overall, the poorly imaged early-rift section does not contain distinct high-amplitude correlatable reflectors except in a few locations where horizons are back-tilted against faults or else lie on basement highs where the sequence is thin. Strata within the early-rift sequence fill the basement deeps and lap onto and/or drape basement highs. The lack of correlatable, seismic stratigraphic sequences in the early-rift section forces a grouping of this section into one depositional unit spanning a large time interval during which resolution and/or correlation of discrete tectonic events is difficult.

In contrast, the late-rift section is divisible into five depositional sequences numbered 1-5 from bottom to top, separated by basin-wide correlatable unconformities (Figure 4.1). These five sequences span the majority of the central basin and each consists of a basal, highly reflective unit and an upper semi-transparent unit. The basin-wide correlatable unconformities coincide with the bases of the highly reflective units. The highly reflective units are composed of doublets or triplets of high-amplitude, continuous, parallel reflectors. The semi-transparent units are composed of low amplitude, continuous, parallel reflectors

(Figure 4.1). Typically, the semi-transparent units are thicker than the highly reflective units and both change thickness along and across the strike of major structures in the basin. The division of the late-rift section proposed here is roughly consistent with that of previous workers [*Clement*, 2000; *Sachpazi et al.*, 2003] although it might be possible to further subdivide the 5 late-rift depositional sequences proposed here.

Towards the southern edge of the basin, late-rift strata terminate abruptly against major bounding faults or merge with chaotic packages of dipping reflectors that are probably slump material eroded from the fault footwalls and/or deposited on rapidly subsiding fault hanging wall blocks. To the north, strata at the base of the late-rift sequence lap onto the basement reflector and/or the top of the early-rift sequence and, up section, sequentially reach further to the north until terminating against south dipping faults and/or inter-fingering with material on the submarine slope. In addition to these general basin fill characteristics, isolated packages of convoluted, hummocky reflectors are present throughout the late-rift section. These are interpreted to represent earthquake-induced turbidity and debris-flow deposits, which, in addition to storm-generated debris surges, and hemi-pelagic sedimentation, and river-fed sediments, constitute the entire budget of sediment supplied to the Gulf floor.

A time scale based on global sea-level fluctuations can be tentatively proposed to explain the seismic character of sequences in the late-rift section and to date tectonic events in the GOC. In the absence of drill-hole data, this is the best method available for approximately dating the Gulf sediments. Currently

sedimentation keeps the seafloor nearly flat and horizontal on the abyssal plain. Therefore, horizons spanning the entire Gulf can be considered as having formed the seafloor at the time of deposition [*Sachpazi et al.*, 2003]. The basin-wide extent of these sequences and their cyclic nature suggests control by externally-induced changes such as global sea-level fluctuations rather than discrete tectonic events [*Sachpazi et al.*, 2003]. Marine deposits on subaerial terraces have been correlated with global high sea-level stands over the past 500 ka [*Armijo et al.*, 1996; *Keraudren and Sorel*, 1987] and sea-level cycles have also been recognized on the northern submarine slope and in the central basin from shallow penetration seismic data [*Lykousis*, 1998; *Perissoratis et al.*, 2000]. Therefore, global sea-level fluctuations have affected sedimentation in the basin.

During sea-level low stands, the Gulf of Corinth has been a lake limited by the 62 m sill depth in the Rio Straits, at the western entrance to the Gulf (Figure 3.1). Sedimentation then was dominated by flows that generate turbidity currents and course grained, river-fed material resulting in the deposition of acoustically well-stratified sediments in the main basin [*Perissoratis et al.*, 2000]. During sea-level high stands, marine conditions prevailed in the Gulf of Corinth and deposition was dominated by fine-grained material dispersed through sediment plumes resulting in the deposition of acoustically weakly stratified sediments in the main basin [*Perissoratis et al.*, 2000]. Coarse-grained material was trapped on the shelf and in delta fans. Therefore, the seismic sequences defined in the late-rift section may record the transition from lacustrine (highly reflective) to marine (semi-transparent) conditions and the sequence boundaries represent

erosion associated with rapid drops in sea level. Furthermore, each sequence may reflect the 100 ka frequency of glacio-eustatic sea-level cycles over the past 500-600 ka [*Gawthorpe et al.*, 1994; *Sachpazi et al.*, 2003].

FIGURE CAPTIONS

Figure 4.1 Small portions of three, EW oriented MCS lines used to illustrate the seismic stratigraphy of the synrift section in the Gulf of Corinth. The MCS line locations are shown in the small inset maps. The basin fill is divided into an early-rift and a late-rift sequence. The late-rift sequence is further sub-divided into sequences 1-5. Each sequence is separated by a basin-wide correlatable unconformity. See text for a further discussion of the basin-fill character.

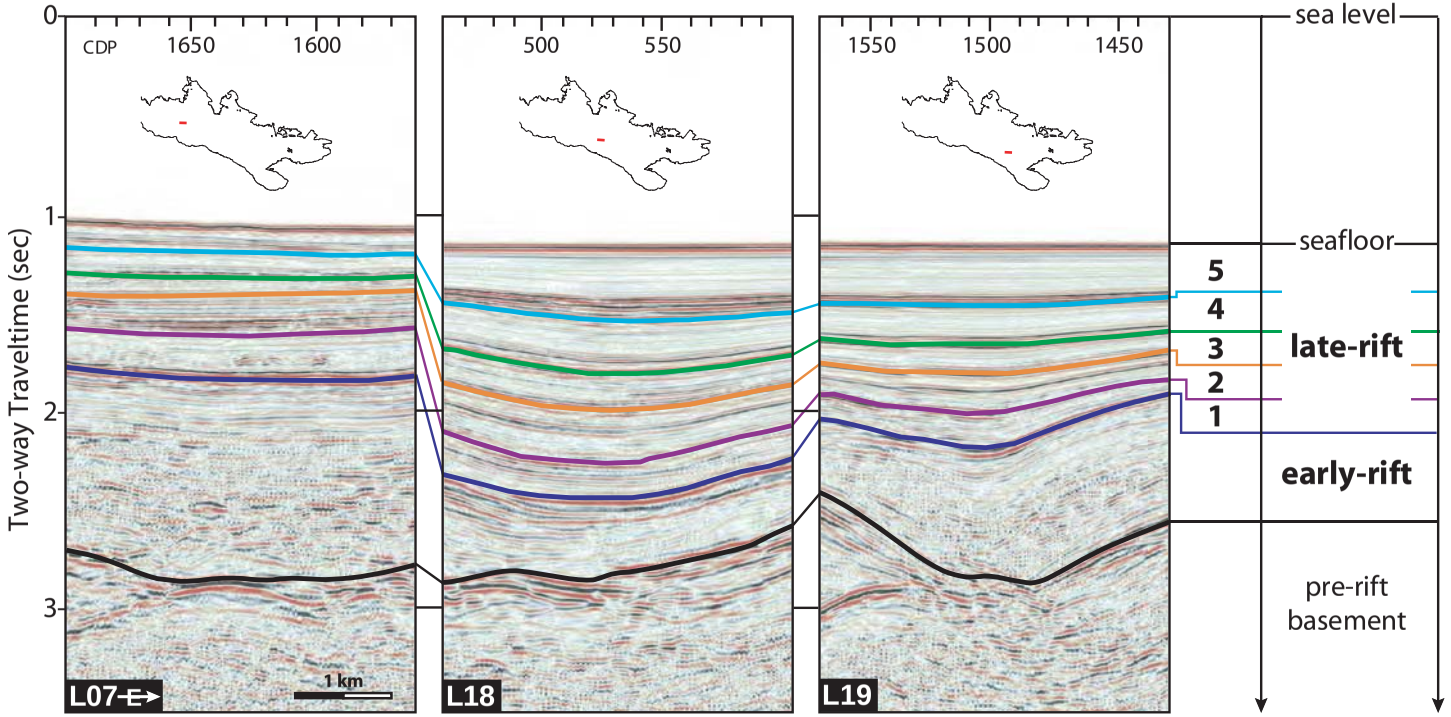
0
1
2
3
Two-way Traveltime (sec)
CDP
1650
1600
500
550
1550
1500
1450
1 km
L07-E
L18
L19
sea level
seafloor
5
4
3
2
1
late-rift
early-rift
pre-rift
basement

Figure 4.1

5. Along-strike structural and stratigraphic variations in the Corinth submarine rift

Introduction

The style of deformation in the Gulf of Corinth has been debated in part because of the variations in earthquake focal mechanisms. In the east, the 1981 earthquake sequence on faults bounding the Alkyonides sub-basin, indicated north-northwest directed normal slip on fault planes dipping ~45° [*Hatzfeld et al.*, 2000; *Hubert et al.*, 1996; *King et al.*, 1985]. However, in the central and western parts of the Gulf the 1965, 1970, 1992, and 1995 earthquakes all occurred on planes dipping ~30° north [*Baker et al.*, 1997; *Bernard et al.*, 1997; *Hatzfeld*, 1996]. In addition, studies of micro quakes and aftershocks in the western Gulf suggest motion on very shallow planes (10-25°) [*Bernard et al.*, 1997; *Rietbrock et al.*, 1996; *Rigo et al.*, 1996].

These observations have resulted in essentially two different deformational models for the region. One model interprets the low-angle earthquakes and clusters of micro quakes as the brittle-ductile transition and suggests that high-angle faults at the surface are active and connect to a lower crust undergoing ductile deformation [*Armijo et al.*, 1996; *Hatzfeld et al.*, 2000]. The other model proposes that high angle faults at the surface ntersect an active, low-angle (~15°) normal detachment [*Doutsos and Poulimenos*, 1992; *Sorel*, 2000]. Since the mechanical feasibility of slip on low-angle fault planes is controversial and earthquakes in the Gulf have been interpreted to suggest such a structure, an intense amount of effort has focused on the area.

The motivation behind the *R/V Maurice Ewing* geophysical investigation of the Gulf of Corinth in the summer of 2001 (EW0108) was to collect a closely spaced grid of deep penetration, multi-channel seismic (MCS) data and directly image active normal faults and the style of deformation in the Gulf. However, the data are only able to image faults that penetrate to a maximum depth of ~4 km i.e., above the seismogenic zone. Despite the inability to image the faults at greater depths, the EW0108 data can be used to infer how the rift has evolved over time, how sediments have accumulated in the rift, and how faulting and sedimentation interact in this setting. In addition, the EW0108 data can be used to evaluate the proposed structural models for the Gulf.

I divide the surveyed portion of the Gulf into four segments that roughly coincide with the locations of major border faults along the southern Gulf margin. I base these divisions on similarities in basement geometry, synrift deformation, and overall basin architecture. The segments are the Heliki segment, the Derveni segment, the Sithas segment, and the Xylocastro-Perahora segment, named after the five major border faults on the south side of the Gulf imaged by the EW0108 survey (Figure 5.1). I present observations from selected MCS lines in each segment and discuss these observations from a structural and stratigraphic standpoint. This approach emphasizes the complexity that characterizes the Gulf and bears upon the proposed models of extension for central Greece and rift basin formation in general.

The Heliki Segment

The Heliki segment is the portion of the Gulf bordered to the south by the Heliki fault and is the westernmost segment in the EW0108 survey (Figure 5.1). The architecture of the Heliki segment varies along strike. Multi-channel seismic (MCS) lines reveal that the main basin widens and deepens eastward across the Heliki segment (Figure 5.2). Additionally, faulting becomes more abundant and the synrift section increases in thickness from west to east across the Heliki segment.

The Heliki border fault (H) controls the southern margin across the Heliki segment (Figure 5.1) except for where L50 (Figure 5.2) images the basin between the Heliki and Derveni faults (Figure 5.1). Since most of the Heliki fault outcrops onshore along the southern margin the MCS profiles in Figure 5.2 image the deeper portion of the fault as a northward dipping basin bounding structure near the southern Gulf margin. Within the basement, the Heliki fault is not a clear reflector and the fault disappears beneath the base of the synrfit section. Additionally, a few large, south-dipping northern faults offset the basement, cut the seafloor, and create scarps and breaks in slope along the northern margin in the Heliki segment.

In L27 (Figure 5.2), both sediment and the basement south of common depth point (CDP) 300 tilt to the north above a large, south dipping fault (CDP 325, Figure 5.2). The maximum sediment thickness reaches ~1.1 km on the hanging wall of this fault. The basement shallows towards the southern margin and resolution is lost as the MCS line turns in the hanging wall of the Heliki fault

(Figure 5.2). North of the fault at CDP 300, the sediment section is thin (<500 m) before the basement steps up across a small horst block onto the shelf south of Eratini. The shallow basement and basin geometry in this area are confirmed by two high resolution seismic surveys [*McNeill et al.*, 2003; *Stefatos et al.*, 2002]. The entire synrift section is present in L27 although channels erode the shallow late-rift sequences.

Approximately 5 km east of L27, large normal faults are clear along both the northern and southern basin margins (L28, Figure 5.2). The sediment section reaches a maximum thickness of ~1.6 km on the hanging wall of the Heliki fault and thins gradually to the north before thinning rapidly across the fault that has a prominent seafloor scarp at CDP 350 (L28, Figure 5.2). From CDP 450-650, the basement is irregular and stair-steps across what I interpret as fault bounded basement blocks. Deep, early-rift strata dip towards and terminate against the southern sides of the blocks, which might be the fault-bounded sides of these blocks. The faults, however, appear to be inactive and do not extend up into the sediment section. Above the irregular basement blocks, high-angle, south-dipping faults cut through the sediment section and do not clearly intersect the basement or reach the seafloor. Late-rift strata are back-tilted across some of these faults.

In L24 (Figure 5.2), approximately 5.25 km to the east of L28, the basement reflector is unclear between CDP's 450 and 500. I infer that the basement is deepest in this location and underlies ~2.5 km of sediment. To the south, there is some indication that the Heliki border fault intersects a low-angle

planar reflector near the base of the synrift section although this reflector is poorly imaged (Figure 5.2). Seismic sequences create a broad monocline above the Heliki fault where it approaches the seafloor. The central basin imaged in L24 lacks basement highs and abundant synrift faulting. The basement steps up to the north across a large fault that reaches the top of the early-rift sequence near CDP 300. To the north, an additional fault reaches from the basement up to the seafloor where it creates a small scarp at CDP 250. The entire late-rift is either thin or absent north of the fault (see gray sediments in L24, Figure 5.2).

L50 is the easternmost line from the Heliki segment (L50, Figure 5.2). I infer that the top of the basement is deepest in the central basin where the basement reflector is unclear, between CDP 200 and CDP 400. Three, high-amplitude, south-dipping reflectors are present above the basement in this location. Basement-parallel horizons dip to the north and terminate against the high-amplitude reflectors. I interpret the south-dipping reflectors as inactive faults and the north-dipping, basement-parallel horizons as early-rift strata deposited on the hanging walls of these faults. In L50, many faults in the synrift section neither reach the basement nor extend above the base of sequence 1. Similar to other MCS lines that image the Heliki segment, L50 contains a large northern fault that steps the basement up to the north. A seafloor scarp associated with the fault is present up dip from the fault termination at CDP450.

A major difference between L50 and the rest of the Heliki segment is the slope of the basement approaching the southern margin. The apparent dip is much less than in adjacent lines and sequences are horizontal and do not thin

before interpretation becomes difficult south of the turn at CDP 50. These observations suggest that L50 images a structural ramp between the tips of the Heliki and Derveni border faults rather than either of the faults.

Line 07 (Figure 5.6) provides an along-strike view of the Heliki segment, which crosses the central Gulf and intersects each of the lines shown in Figure 5.2. The along strike view of the basin confirms that top of the basement deepens eastward and east of L28 deepens rapidly to CDP 1600 where the synrift section in this segment reaches a maximum thickness of nearly 2.5 km. The early-rift sequence comprises more than half of this thickness and late-rift sequences progressively show less pronounced thickening. Line 07 does not reveal the presence of any major structures such as strike-slip or transfer faults oriented oblique to the general EW strike of the majority of faults in the Gulf.

The Derveni Segment

The Derveni segment is the portion of the Gulf south of and including the subsidiary Gulf of Itea (south of Itea in Figure 5.1). Across this segment, there are 10 MCS lines from EW0108 with an average spacing of ~1 km between lines. The Derveni fault (D) dips north along the southern margin, extends into the basement, and becomes low-angle and/or merges with a low-angle, planar reflector beneath the synrift section. That reflector loses definition in the basement by 4 km total depth. The basin fill is consistently thick (>2 km) across the entire segment and is cut by many faults, all of which disappear and/or sole into sub-horizontal reflectors within the early-rift section. The large faults approaching the northern margin offset the basement and the relative

thicknesses of the early- and late-rift sections imply that the early-rift basin was, across portions of the Derveni segment, controlled by these large northern margin faults.

In general, the dip of the Derveni fault decreases with depth and is low-angle (<30°) in the basement. In L15 and L49 the border fault geometry is listric but in L48 the border fault geometry is bi-planar and the shallow portion of the Derveni fault intersects a low-angle, planar reflector, which extends from ~4 km depth up-dip to the south but becomes obscured before the end of the MCS line. In both L15 and L49 (Figure 5.3) a similar bi-planar geometry is suggested by the difference in dip between the shallow and deep portions of the Derveni fault. However, no up-dip portion of the planar reflector is clearly imaged in either of these MCS profiles. The southern margin border structure in L14 (Figure 5.3) is less steep than the Derveni fault plane reflector imaged in adjacent lines. This difference is due to the position of L14 at the western tip of the Derveni fault, near the structural ramp between the Heliki and Derveni faults (Figure 5.1).

The top of the basement in the Derveni segment is bowl-shaped in the west (L14) but to the east, the top of the basement becomes deeper towards the southern margin (L49 and L48). This results from the decrease in size and/or absence of large faults along the northern margin of the eastern Derveni segment. To the west, however, the large-offset faults along the N margin continue from the Derveni into the Heliki segment.

Across the Derveni segment and portions of the Heliki segment, the early-rift structural segmentation in the Gulf was different from now. In the Derveni

segment, most of the faults that cut the late-rift section in the central basin disappear or sole into sub-horizontal reflectors within the early-rift sequence such as at CDP 950 in L15 (Figure 5.3). Additionally, subtle changes in the relative thicknesses of the early-rift and late-rift sections in the Derveni segment illustrate contrasts in deposition over time.

In L14, the early-rift section is consistently thick across the central basin from north to south whereas the late-rift section thickens to the south, towards the Derveni fault. Within the early-rift section, strata are back-tilted to the north (black in L14) indicating the presence of inactive, south-dipping faults (dashed red in L14) (Figure 5.3). The apparent dips of these faults are <30°. In contrast, the apparent dips of the high angle faults that cut the late-rift section and approach the seafloor are >45°. This relationship suggests that perhaps the inactive faults were once high angle and subsequently rotated >15° northward to inactive orientations.

In L15, the early-rift section thickens to the north towards the large fault that steps the basement up to the north near CDP 700. The late-rift section thickens to the south, towards the Derveni fault. These differences imply a ‘flip flop’ in the location of maximum subsidence and border fault growth from the northern margin during deposition of the early-rift sequence to the southern margin during deposition of the late-rift section. In L24, L50 (Figure 5.2), L14, and L15 (Figure 5.3) the early rift history was dominated by the large faults along the northern margin and, therefore, the rift segmentation was controlled by these

large faults rather than the current configuration, controlled by border faults along the southern margin.

Line 49 provides an excellent example of the Derveni segment structure. The Derveni fault reaches the seafloor at CDP 725 and becomes low-angle, near the base of the synrift section as it extends into the basement. North-south variations between the early- and late-rift sections characterize the basin fill in L49. The early-rift section is slightly thicker to the north and an on-lap surface, at the base of the section near the northern margin, may be a debris flow related to once active faults on the Pangalos Peninsula. In contrast, the late-rift section clearly thickens towards the southern margin. A rollover anticline and crestal graben, located above where hanging wall basement is pulled off the footwall are present near CDP 550. North of the graben, late-rift sequences are back-tilted against many faults that cut the late-rift section. These faults disappear within the early-rift section and do not clearly offset the basement.

Line 48 images transitional basin architecture. The large northern faults that step basement up to the north are no longer present and the top of the basement is deepest and bowl-shaped in the southern part of the basin where the synrift section reaches a maximum thickness of ~2.8 km. The basement steps up and the synrift section thins across a large, south-dipping fault near CDP 250. Additionally, low-angle (<30°) faults create a series of small basement blocks approaching the northern margin but major changes in sediment thickness do not occur across the faults. In the deep, central basin, high-angle faults cut the late-rift section but disappear within the early-rift sequence. North of CDP 250

these faults intersect but do not offset the top of the basement. Approaching the northern margin the basement gradually becomes shallow and late-rift sequences lap onto the top of the early-rift sequence indicating a slight narrowing of the sediment depocenter during late-rift sediment deposition.

Along the southern margin in L48, the steeply dipping portion of the Derveni fault intersects a low-angle, planar reflector which extends up-dip and off section to the south. The low-angle, planar reflector is imaged to ~4.5 km depth (3.5 sec TWT). The hanging wall basement block of the Derveni fault intersects the planar reflector ~2 km north of where the steep portion of the fault intersects the reflector (CDP 150 vs. CDP 75) indicating that the hanging wall block of the Derveni fault is moving to the north on the low-angle portion of the fault.

Both L07 and L09 (Figure 5.6) image the across-strike structure of the Derveni segment. Line 07 is located near the northern part of the central basin and the basement gradually becomes shallow across the Derveni segment as the MCS line nears the northern slope. Line 09 is located very close to the southern margin and an examination of L15, L49 and L48 reveals that their intersection with L09 coincides with the down-dip portion of the Derveni fault. Therefore, the broad basement high in L09 between L15 and L48, is the Derveni fault.

The Sithas Segment

The Sithas segment (Figure 5.4) differs significantly from the two western segments. No longer do the majority of late-rift faults disappear within the early-rift section. Instead, faults cut the entire basin fill and intersect or offset the top of

the basement. Additionally, intra-basement faults are imaged extending to greater depths and most faults along the northern margin are significantly smaller than similar faults in the west. The Sithas fault is high angle near the seafloor and intersects a low-angle reflector (L34), cuts a low-angle reflector (L35), or is listric (L41). In addition, the down dip portion of the Xylocastro fault, which outcrops subaerially on the PP, is imaged south of the Sithas fault in L35 and L41. The basin fill in the Sithas segment does not record a complex, early-rift history and is thinner than the late-rift section, which is thickest adjacent to the Sithas fault and within a central graben partially created by the Derveni fault.

In L34 (Figure 5.4), the Sithas fault (S) replaces the Derveni fault as the major structure along the southern margin. South of CDP 100, a turn at the southern end of L34 makes the shallow interpretation difficult. The turn also causes the Sithas fault to appear to ‘roll over’ rather than intersect the seafloor. North of the turn, however, the down-dip portion of the Sithas fault intersects a low-angle planar reflector, which extends up-dip beneath the Sithas fault a short distance and down-dip to >4 km (>3.5 sec TWT).

Although the Derveni fault is no longer the major border fault across the Sithas segment, it extends into the central basin where the orientation of the coastline changes near 22°30’ E and forms the southern boundary of an EW-trending graben (DFG, Figure 5.4) outboard of the Sithas fault (Figure 5.1). Across the entire Gulf, sequence 5 is thickest within this graben in the location of L34 (DFG, Figure 5.4). The basement steps up gradually to the north of the central graben across south-dipping, planar faults, some of which reach the

seafloor and create scarps (Figures 5.1 and 5.4). One such fault, just north of the intersection with L07 (CDP 520), creates the long, linear scarp imaged in the bathymetry (Figure 5.1).

A major difference between the Sithas segment and segments further west is the relative thicknesses of the early- and late-rift sections. The early-rift section in L34 is thinner and occupies a narrower portion of the Gulf than further west. The late rift section in L34 is thickest across the DFG rather than adjacent to the southern margin, is cut by fewer faults, and is generally thicker than further west. This difference is apparent when comparing L34 (Figure 5.4) and L48 (Figures 5.3).

Line 35 (Figure 5.4) images the Sithas segment near the center of the Sithas fault, which intersects the seafloor at CDP 1140. Similarities in the basin architecture exist between L35 and L34. For example, the top of the basement gradually deepens to the south without large steps across faults until intersecting the Sithas fault. However, the synrift section reaches a maximum thickness of ~2.3 km on the immediate hanging wall of the Sithas fault, where strata exhibit normal drag, rather than across the DFG, which is still present but less pronounced and created by many, various sized faults, none of which reach the seafloor.

At the southern margin, the Sithas fault maintains a constant dip of ~45° from the seafloor to beneath the base of the synrift section. A low-angle (~25°), north-dipping reflector intersects the Sithas fault where it meets the top of the basement and extends down-dip a short distance on L34. South of the Sithas

fault in L35 (Figure 5.4), two large canyons incise the seafloor on the submarine shelf. Beneath these canyons, a strong but discontinuous, north-dipping reflector between CDP's 1200 and 1310 underlies a thick sediment section. L35 is nearly coastline-parallel south of CDP 1200. This reflector might be a down dip portion of the Xylocastro fault (X), which is located onshore just south of L35 (Figure 5.1). North of the turn, the dip of the reflector increases but it is only imaged to ~2 sec TWT.

In L41 (Figure 5.4), the maximum sediment thickness is ~1.6 km, nearly one kilometer less than in the adjacent L35. Additionally, a series of north dipping faults in L41 creates basement blocks similar to those imaged in L48 (Figure 5.3). However, these blocks are close to the southern margin whereas those imaged in L48 are further to the north. The blocks in L41 form the top of the basement across the deep, central basin. The block-bounding faults are high angle where they cut through the sediment section and become low angle as they extend into the basement (Figure 5.4).

Along the southern margin in L41 the Sithas fault (S) is listric and has a constant, high-angle dip (~47°) until beneath the synrift section where it becomes low-angle (~20°) at 3 sec TWT. The basement block-bounding faults are listric and oriented similar to the Sithas fault. Similar to L35, the Xylocastro fault (X) approaches the seafloor south of the Sithas fault. A small basement or rider block, overlain by ~1 km of uncorrelated sediments, is present between the two faults. The Xylocastro fault plane reflector becomes obsucured as it approaches

the incised seafloor south of the turn. However, I propose that the Xylocastro fault extends offshore into the Gulf and crosses the Gulf margin in this location.

In the synrift section, the central graben (DFG) is still present east of the surface traces of the controlling faults. North of the graben, the synrift thickness is relatively constant before sequences terminate abruptly against a large south-dipping fault (CDP 600) that steps basement up to the north onto the incised submarine slope. This fault and the Sithas fault border the deep, central basin. They are the primary faults that create seafloor scarps in the central basin in L41 (Figure 5.4), although smaller offset faults at CDP 750, 840, and 900, reach the seafloor on the north slope.

The Xylocastro-Perahora Segment

The Xylocastro-Perahora segment includes portions of the Gulf controlled along the southern margin by the Xylocastro and Perahora faults and the area north of and including the mouth of the Gulf of Lechaio (Figure 5.1). This segment has been the focus of a considerable amount of research after the 1981 series of earthquakes activated subaerial and submarine faults on and around the Perahora Peninsula and Alkyonides Gulf (Figure 2.4) [*Armijo et al.*, 1996; *Jackson et al.*, 1982].

The architecture of the Xylocastro-Perahora segment is unique from other segments and variable across the segment (Figure 5.5). Where crossed by L37, nearly 2.5 km of synrift sediments are present within the intra-rift graben (CDP's 740–1040) on the hanging wall of the Xylocastro fault, which is >30 km-long and in this location is a submarine basin bounding fault (Figure 5.1). Strata terminate

against the Xylocastro fault without significant rotation (drag) except at the base of the late-rift section (Figure 5.5). The Xylocastro fault decreases dip with depth from 45° to 30° before it disappears beneath the synrift section. Within the intra-rift graben, a few faults cut the sediment section and cause changes in sequence thicknesses but none reaches the seafloor. However, further north, high-angle, planar faults offset the basement and create the ~E-W trending horst block between CDP's 590 and 740. Strata are thicker on the downthrown blocks than on top of the horst indicating that these are growth faults, active during synrift sediment deposition. Sequences are equally thick across the intra-rift graben and the deeper late-rift sequences sag near its center (CDP 850). Therefore, the graben appears to subside uniformly with respect to each of the bounding faults and may act as a keystone between the Xylocastro and antithetic bounding faults, which appear to intersect at ~4 km depth on an adjacent MCS line (not shown). A south dipping fault at CDP 480 limits the northern extent of the correlatable sequences. This same fault appears at CDP 600 in L41 (Figure 5.4). The basement offset across this fault in L37 (~700 m) is less than in L41 (~500 m).

L05 (Figure 5.5) images the Gulf between the Xylocastro and Perahora faults (Figure 5.1) where the maximum synrift sediment thickness has decreased substantially to ~1.5 km at CDP 410. The southern basin margin imaged in L05 is different from any other part of the Gulf. The contact between the basement and the sedimentary fill between CDP's 550 and 650 dips ~20° north and early-rift strata do not terminate against but are conformable with this contact and possibly

correlate with the sedimentary fill in the Gulf of Lechaio. The late-rift sequences in the main basin sag and lap onto the top of the early-rift sequence approaching the southern margin. Additionally, the seafloor slope in L05 is subdued and no steep scarp is present when compared to adjacent lines. The western tip of the Perahora fault may be present in L05 (CDP 750, Figure 5.5) but it is not apparent that a large, north-dipping, submarine border fault controls the southern margin north of the Gulf of Lechaio (Figure 5.1). However, the late-rift sagging adjacent to the southern margin and the series of south-dipping faults between CDP 475 and 575 imply extension that might be associated with a structural ramp or zone of deformation between the ends of the Xylocastro and Perahora faults similar to near the eastern tip of the Heliki fault (Figure 5.2).

The central basin in L05 contains a series of south-dipping faults that do not clearly intersect the basement south of CDP 500. The northernmost of these faults borders a basement horst block (CDP's 450-500) that creates a "trap-door." The early-rift section is thickest on the downthrown sides of the horst whereas the late-rift section is unaffected by the structure. The fault that borders the northern side of the block is important for a number of reasons. 1) The intersection of this fault and the top of the basement (CDP 425) is along-strike from the intersection of the Xylocastro fault and the top of the basement in L37 (Figure 5.5) implying a possible relationship between the two faults. 2) An on-lap surface within the early-rift section, north of the fault, indicates fault-related subsidence and filling of fault-generated topography. 3) The late-rift section thickens and sags above the on-lap surface but no shallow, brittle faulting is

associated with this thickening. Although the fault does not extend above the early-rift section, it may still be affecting late-rift sedimentation. Otherwise, the sagging in the central basin, far from major border faults, might be associated with ductile extension, which would result in basin subsidence and filling without accompanying brittle deformation. Finally, it is worth noting that no large faults reach and/or offset the seafloor in the central basin in L05.

L06 (Figure 5.5) images a rather simple basin architecture. The Perahora fault, which creates a prominent seafloor scarp, is the major border fault along the southern margin (Figure 5.5). The late-rift section thickens and dips to the south before terminating against the fault and shallow sequences (1-4) exhibit normal drag. Late-rift sequences progressively decrease in width across the basin. For example, sequence 5 maintains its thickness from north to south, across the entire Gulf whereas sequence 1 is thick in the south, thins to the north, and is more or less absent near the northern margin. These observations suggest that deposition has narrowed over time because motion stopped or slowed on the northernmost basin bounding faults as the Perahora fault continued to accumulate slip.

Both the Perahora fault and a large synthetic fault to the north affected early-rift sedimentation. The fault to the north, which only slightly offsets late-rift sequences and terminates at the base of sequence 1 (CDP 425), is the same fault imaged in L05 and is possibly related to the Xylocastro fault. The synrift section reaches a maximum thickness of ~1.5 km above this fault and the early-rift section is thickest on the hanging wall of the fault. Early-rift strata terminate

against the fault, and the top of the basement is deepest and tilted towards the fault. Sagging in the late-rift section (see L05) is not associated with the portion of the fault imaged in L06. It appears that the northern fault was the major structure in this part of the basin and that an early depocenter was located on the hanging wall of the fault.

Line 09/22 and L19 (Figure 5.6) image the along-strike architecture of the Xylocastro-Perahora segment. Beneath the deep (>850 mbsl), flat seafloor imaged in L19, the basement is characterized by pronounced depth variations. The western basement deep in L19 (centered at CDP 1500) is located within the intra-rift graben on the hanging wall of the Xylocastro fault (L37). The synrift section is thickest and sags across this deep. Early-rift strata lap onto the edges of and are horizontal above the adjacent basement high, and the late-rift sequences are horizontal and maintain their thicknesses across the high. The early-rift section is thickest across the adjacent deep, centered at CDP 1000, which is associated with the early-rift fault in the central basin (L06). The intra-basement reflectors in L19 are complex. The east-dipping reflector between CDP 1600 and 1750 is the Sithas fault and/or its down-dip, low-angle extension. This reflector appears to merge with the top of the basement at CDP 1525 via a short, west-dipping reflector, which may still be the Sithas fault. The Xylocastro fault, which is the border fault in L37, is not a clear intra-basement reflector in L19. Further east, a concave-up, intra-basement reflector (CDP 1200-1375, L19) is probably the north-dipping fault in the central basin (L05 and L06) that creates a

basement ‘lozenge’. The basement high above this reflector is the hanging wall of the fault.

Line 09/22 images the Xylocastro-Perahora segment ~4 km north of L19 and provides an oblique view of the central basin horst block between CDP’s 250 and 450. Both the top of the basement and the seafloor become shallow approaching the Alkyonides Gulf in the east.

An important characteristic of the Xylocastro-Perahora segment is the presence of large, south-dipping faults and a thick sediment section (>1 km) in the Gulf of Lechaio. These large faults cut the footwalls of the Xylocastro and Perahora border faults and suggest the presence of additional faults and a thick basin fill throughout the Gulf of Lechaio. Several previous studies ignored these features, which affect the relative motions of fault blocks in the eastern Gulf and the Xylocastro and Perahora faults in particular.

Discussion

The descriptions above show that structure in the Gulf of Corinth varies along strike. A few key points result from these descriptions. The Heliki segment changes along strike from a narrow, shallow basin in the west to a deep graben, controlled by large normal faults along both margins in the east. The Derveni segment varies from a symmetric graben in the west to a more asymmetric graben in the east due to the presence and subsequent absence of large steps in basement across south-dipping normal faults along the northern Gulf margin. The Sithas segment varies from a half graben in the west to a graben in the east, clearly controlled by the Sithas fault along the southern margin and a large fault

along the northern margin. The Xylocastro-Perahora segment is more or less an asymmetric half-graben controlled along the southern margin by the Xylocastro and Perahora faults. Additional faults are variably developed. Large, south-dipping faults and a thick sediment section are present on the submarine shelf between the Xylocastro and Perahora faults and in the northern Gulf of Lechaio.

In addition to the variations in structural geometry, variations in synrift sediment thickness characterize the Gulf of Corinth and provide clues to the structural evolution of the basin. The thickness of the sedimentary fill increases from <1.5 km in the westernmost portion of our survey area (L27, Figure 5.2) to ~2.5 km in the eastern Heliki segment. Most of this increase in thickness occurs within the early-rift section. The synrift section then thins gradually to the east but generally remains thick (≥2 km) in the Derveni and Sithas segments. However, the relative thicknesses of the synrift sections change and the late-rift section is substantially thicker than the early-rift sequence in the Sithas segment. In the Xylocastro-Perahora segment, the maximum basin fill thickness is ~2.5 km and the early- and late-rift sections are equally thick on the hanging wall of the Xylocastro fault (L37, Figure 5.5). The sediment thickness decreases to <1.5 km on the hanging wall of the Perahora fault although L19 (Figure 5.6) images a substantial early-rift depocenter east of L06. An old fault in the central Gulf, possibly related to the Xylocastro fault, controls this depocenter.

The thick early-rift sequence in the Derveni and eastern Heliki segments lacks continuous horizons and clear faults. In a few locations, such as L14 (Figure 5.3), early-rift horizons are north-tilted more than late-rift horizons. The

poorly imaged faults associated with the tilting appear unrelated to steeper faults that cut the late-rift section and die out in the upper early-rift section. Reflectors in the early-rift section in L50 (Figure 5.2) are less clear but otherwise similar to those imaged in L14 (Figure 5.3). Additionally, the top of the basement in L28 and L48 contains structures that imply an early-rift history different from the late-rift history. In L28 (Figure 5.2), the stair-stepping basement is a series of blocks bordered by faults that dip more gently than the late-rift faults, which die out above the basement. In L48 (Figure 5.3), north-dipping, low-angle (<<30°) faults offset the basement but do not extend up into the sediment section. Instead, high-angle faults intersect the basement, cut the sedimentary fill, and approach the seafloor (Figure 5.3).

Fault-block rotation helps explain some of these observations because slip on a set of parallel, high-angle faults results in rotation of the fault bounded blocks (Figure 5.7) [*Gibbs*, 1984; *Martel*, 1999]. I infer that sediment accumulates on the fault hanging walls and continued slip results in further rotation of the faults until they lock. A new set of high-angle faults forms and replaces the locked set of faults as extension continues and the same process can repeat [*Forsyth*, 1992]. This type of fault evolution aids in explaining the orientations of early-rift strata and basement blocks across portions of the Derveni and Sithas segments and considering the multiple fault and strata orientations that can develop during this evolution, the model helps explain imaging difficulties in the early-rift section.

If the interpretation above is correct, then the current basin geometry in portions of the Heliki and Derveni segments, controlled primarily by large faults along the southern Gulf margin, does not reflect the early-rift basin geometry. In particular, the large, south-dipping normal faults along the northern margin were controlling structures early in the rift deposition. The southern border faults, which are the controlling structures today, were small and/or absent early in the rift deposition. Line 15 (Figure 5.3) images the clearest example of early-rift thickening and tilting towards the large fault along the northern margin in the Derveni segment. In contrast, the late-rift sequences thicken towards the southern border faults and the early-rift complexities are absent in the Sithas and Xylocastro-Perahora segments. The orientations of strata in these eastern segments suggest that the current fault geometry and structural segmentation has been in place since the early-rift history.

Post-migration depth converted MCS lines

It is extremely important for seismic hazard assessment and an overall understanding of how deformation occurs in the Gulf that the geometry of major faults be accurately constrained. Proposed fault geometries have suffered due to the rather sparse data available. Although we do not image faults extending to depths much greater than 4 km, we image their shallow geometries across the entire Gulf. Figure 5.8 includes representative post-migration, depth-converted MCS lines from each of the rift segments. The interpreted versions (Figure 5.8B) do not include the portions of the MCS lines in turns at the southern margin because they do not contain accurate dip information. These lines provide

accurate sediment thickness and fault dip information, which in combination with the architecture of the basin help constrain some of the proposed models for the Gulf of Corinth. Appendix 1 provides a detailed explanation of the processing used to convert time sections to depth.

The important information revealed by the depth converted MCS profiles in Figure 5.8 is the geometry of the major border faults along the southern margin. The dips of the portions of these faults that border the synrift section are variable. They range from ~53° in the Sithas segment to ~22° in the Heliki segment. The dip of a single fault consistently varies along-strike. For example, the Derveni fault dip increases from ~30° in L14d to ~35° in L49d over a distance of ~7.5 km. The Heliki and Sithas faults also vary in dip along their lengths. However, faults in the basement along the southern margin are all low-angle with dips that vary from 19-33° (Figure 5.8). In no location do the intra-basement portions of the southern border faults dip greater than 33°. Variably developed faults other than those along the southern margin are much higher angle (40-70°) except for those that create basement blocks in L28d. Another important observation from the depth converted MCS profiles is that most of the southern border faults are imaged to depths no greater than ~4 km and in some cases, the major border faults are not imaged clearly beneath the base of the synrift section.

Comparisons to previously proposed models for the Gulf of Corinth

Previous models of basin evolution and seismicity deep beneath the Gulf were handcuffed by a lack information about the stratigraphy and basement

structure in the Gulf. Figure 5.9 presents a few of these models that I will discuss in light of the EW0108 MCS data.

Sorel [2000] proposed the low-angle detachment model for the Gulf shown in Figure 5.9A based on onshore observations of the progressive northward decrease in fault age and rift-related sediments on the PP. In his model, the southernmost and earliest fault on the PP was, at one time, the subaerial expression of the active detachment currently beneath the Gulf. Progressively younger faults formed to the north and the southern part of the detachment became inactive and stranded. Therefore, the high angle, inactive faults onshore as well as the active, submarine basin bounding faults are secondary structures above the master detachment.

The MCS data are compatible with aspects of the low-angle detachment model. For example, in some locations the southern margin geometry is similar to the boxed area in Figure 5.9A and consists of a steep border fault that intersects a low-angle planar structure at the base of the synrift section. For example, the geometry imaged in L48 (Figure 5.3) consists of an intermediate angle (30-45°) Derveni fault, which intersects a low-angle planar feature that extends down-dip beneath the synrift section and up-dip out of the plane of the MCS section. Line 34 (Figure 5.4) images a similar bi-planar geometry although the low-angle structure does not extend up dip to the south.

Despite some similarities, evidence from the EW0108 MCS data that supports the shallow, low-angle detachment model [e.g. Clement, 2000; Sorel, 2000] is far from substantial. The model does not include or account for the large,

south dipping faults imaged on the northern Gulf margin that appear to have played an important role during early-rift sedimentation. Rather, the model proposes a simple northward progression of faulting and a simple down-flexed northern hanging wall. The data do not image a bi-planar geometry with respect to faults south of the current Gulf edge. In locations where more than one fault is imaged, such as the Xylocastro and Sithas faults in L35 and L41 (Figure 5.4), the low angle portion of the Sithas fault does not extend up dip to the south and the Xylcoastro fault plane reflector does not extend deep into the basement.

Rigo *et al.* [1996] proposed a deep detachment model for the Gulf of Corinth based on the results of a dense seismological experiment in the western Gulf of Corinth in 1991 (Figure 5.9B). They observed microseismicity between 6- and 11-km-depth and the focal mechanisms of well-constrained earthquake events indicate a 10-25° north-dipping nodal plane and a steep south-dipping plane. Rigo *et al.* [1996] propose that the major, high-angle surface faults root in a deep, shallow-dipping detachment and that much of the observed microseismicity occurs at the junction between the high-angle surface faults and the detachment (Figure 5.9B).

The location of the seismicity study, west of Heliki, falls outside of the EW0108 survey area where the submarine rift is narrow and the majority of faulting occurs on the PP (Figure 5.1). Line 27 (Figure 5.2) provides the only glimpse of this part of the Gulf and reveals a large, south-dipping submarine fault and a synrift section back-tilted to the north. East of L27 the majority of faults are located in the submarine portion of the rift.

The model in Figure 5.9B requires major border faults to remain high angle from the surface to 6-11-km-depth, which is not the case in the Gulf of Corinth. Considering the lack of information about the down dip geometry of the faults exposed on the PP, the deep detachment model may be valid for the western Gulf where clusters of micro earthquakes define a low-angle zone and where the rift architecture differs from the surveyed portion of the Gulf.

Figures 5.9C-E include a suite of models that differ from those just described. None invokes active low-angle faulting. Rather, the models propose that high-angle faults at the surface extend to the base of the brittle crust with very little change in dip.

Westaway [2002] (Figure 5.9C) reinterprets the cross section from Sorel [2000] and suggests that the outcrop evidence indicates multiple generations of high-angle faults rather than an active low-angle detachment. Westaway [2002] suggests that the rotation of fault blocks, in a manner similar to what I infer for portions of the Heliki and Derveni segments, better explains the outcrop evidence than the low-angle detachment model. Furthermore, Westaway [2002] suggests that the active low-angle fault arguments based on clustering geometries of micro earthquakes [*Hatzfeld et al.*, 2000; *Rietbrock et al.*, 1996; *Rigo et al.*, 1996] are inconclusive because the clusters may represent fault block reorientation, not major active structures and that the large earthquakes are just as likely to have occurred on the steep, south-dipping fault planes. The EW0108 data clearly reveal the presence of a number of very large, south dipping faults (Figures 5.2

and 5.3) that reach the seafloor along the northern Gulf margin. It is difficult to directly correlated any of these faults with the large earthquakes in Figure 2.4.

Figure 5.9D is a model for the Gulf proposed by Jackson *et al.* [1982] based on teleseismic, local seismic, surface faulting, and geomorphological data after major destructive earthquakes occurred in the eastern part of the Gulf of Corinth in February and March 1981 (Figure 2.4). In their examination of surface faulting, Jackson *et al.* [1992] suggest that the major Gulf faults are listric based on fault plane solutions that have nodal dips of 40-50°, nearly vertical surface fault dips, and deformation in the hanging walls of the faults. They propose that faulting on the north side of the Gulf is antithetic to major faulting on the south and accommodates internal deformation of the hanging wall.

It is important to note that Jackson *et al.* [1982] base their model on surface faulting and earthquakes from in and around the Alkyonides sub-basin rather than from the main basin where imaged border faults have dips <50° near the surface and ≤30° near the base of the synrift section and in the basement. For example, the Perahora fault (L06d, Figure 5.8) decreases in dip from 45° near the surface to 33° in the basement. Although many of the southern border faults are listric, the faults along the northern margin are too large to be solely the result of hanging wall deformation above the southern border faults. Therefore, a high angle fault model based on focal mechanisms from the Alkyonides Gulf is not valid for the main basin primarily because southern border faults in the main basin are significantly lower angle than those observed by Jackson *et al.* [1982].

It seems that the deformational style in and around the Alkyonides sub-basin is different from the main basin.

The last model I will discuss is the thick-elastic-plate model of rift flank uplift based on the flight of marine terraces exposed on the PP (Figure 5.9E). The model, proposed by Armijo *et al.* [1996], assumes that the edges of the terraces lie in the footwall of the Xylocastro fault bounding the Corinth rift. The fault in the model is high-angle (50°) from the surface to the base of the brittle crust and extends across the entire mouth of the Gulf of Lecahio. The modeled geometry of the Xylocastro fault is incorrect (see Figure 5.1) and the model greatly over predicts the sediment thickness in the main basin. The model also ignores the south-dipping faults and thick (>1 km) sediment section in the Gulf of Lechaio.

A major difficulty arises when attempting to relate onshore observations, seismicity, and the MCS data into a simple model for deformation in the Gulf of Corinth. Although faults along the southern margin are all low-angle in the basement, none of the MCS profiles image the faults extending beneath ~4 km and the high angle faults along the northern margin rarely extend beneath the top of the basement. Since all of the large earthquakes occur 6-12 km beneath the Gulf it is not yet possible to directly relate the imaged faults to the large earthquakes and the microseismicity.

Important questions remain concerning how and why the Gulf of Corinth is so structurally complex. Clearly, none of the proposed models adequately explains the structural variations in the Gulf. A somewhat ignored factor is the

unique tectonic setting of the Gulf Corinth. The Gulf is located in a forearc setting above the foundering African slab, which subducts northward along the curved Hellenic trench (Figure 2.1). The distance between the Corinth rift and the trench increases eastward. Near the Rio Straits, where the Gulf is narrow, shallow, and faulting extends onshore to the south, the Gulf is close to the trench. Near the Perahora Peninsula, the Gulf is far from the trench. Although the development of low-angle faults is contrary to standard rock mechanic theory, low-angle faults might form under extreme conditions, where dramatic lateral variations in the state of stress exist across the extending region [*Westaway*, 1999]. Scenarios modeled by Westaway [1999] include slab rollback, which is partially responsible for the formation of the Gulf of Corinth rift [*McClusky et al.*, 2000].

The thickness and rheology of the lithosphere is another important factor in rifting. In the Gulf of Corinth region, the crust thins from >40 km at ~22° E to ~25 km at the Perahora Peninsula [*Zelt et al.*, submitted]. These are post-rift estimates but reflect the over-thickened crust related to the NW trending Hellenic mountains that form the backbone of Greece. Previous studies suggest that lithosphere with over-thickened crust is substantially weaker than lithosphere with thinner crust of the same composition [*Vink et al.*, 1984]. Therefore, the presence of many inactive faults onshore in the west and multiple generations of faults in the Heliki and Derveni segments may be a response to the preferential rifting of over-thickened crust just as the eastward deepening of the submarine basin probably reflects eastward thinning of the crust beneath the Gulf. However, the locus of maximum thickening is located tens of kilometers to the west (~22° E) of

the Heliki and Derveni segments, where there is very little evidence for an abundance of rift-related structures.

Conclusions

The Gulf of Corinth is a series of asymmetric grabens controlled by right stepping, en-echelon faults along the southern margin. Faults along the northern margin that create seafloor scarps and contribute to the overall morphology of the Gulf are variably developed. I divide the basin in the area of our MCS data into four rift segments based on the locations of the southern border faults, which are intermediate to high angle near the seafloor (typically 30-50°) and become lower-angle (19-30°) near the base of the sediment section in a listric and sometimes bi-planar fashion.

The Gulf architecture changes dramatically within and between segments due to the faults along the northern margin and in the central basin. In portions of the Gulf, northern margin faults are large and early-rift sediments thicken towards these faults indicating they were important structures in the early evolution. In other locations, the late-rift section thickens towards northern margin faults. Across the entire Gulf, the late-rift sediments generally thicken towards the southern margin. Therefore, the relative offsets on the controlling faults have changed through time. Patterns developed in the basin fill reflect these changes and confirm the intimate relationship between faulting and sedimentation. Strike-slip or transfer faults are not present between the ends of major border faults.

The comprehensive view of the Gulf provided by the MCS data aid in evaluating previously proposed models that tend to make assumptions about the

deep structure of the rift. The high angle fault models [*Armijo et al.*, 1996; *Jackson et al.*, 1982] do not work for the main basin and there is little direct structural evidence in support of the deep, low-angle detachment model [*Rigo et al.*, 1996]. The Gulf is not simply underlain by a single detachment fault that controls the evolution of the rift or bordered by high-angle, planar faults that extend from the surface to the base of the seismogenic zone.

This study provides a view of the architectural variations that characterize the Gulf of Corinth and record the collapse of the upper crust in response to extension of the lower crust. The data do not reveal structures that link the shallow deformation to the deep extension: the border faults along the southern margin become 19-33° above 4-km-depth and the prominent planar faults on the north are rarely imaged beneath the base of the synrift section. However, it is apparent that the along-strike evolution of the Gulf has varied due to the differences in timing and offset of the large faults along the southern and northern Gulf margins.

FIGURE CAPTIONS

Figure 5.1 Illuminated topography and bathymetry of the Gulf of Corinth. Major faults are included (nomenclature same as in Figure 3.2). The EW0108 grid of multi-channel seismic (MCS) lines is in light gray and MCS lines discussed in the text are in blue. Black numbers denote selected common depth points (CDP's), small blue dots denote every 50th CDP, and large dots denote every 1000th CDP. CDP interval=25m.

Figure 5.2 Un-interpreted (A) and interpreted (B) MCS lines across in the Heliki segment. The east west oriented tie line L07 (Figure 5.6) aligns each of the MCS lines shown in the Heliki segment. Labeled turns occur at the southern ends of the MCS lines. Small arrows denote the slip direction on major faults. Colors in the sedimentary fill are the seismic sequences defined in Figure 4.1. Most of the faults in the synrift section are not clear beneath the base of the sediment section. H=Heliki fault.

Figure 5.3 Un-interpreted (A) and interpreted (B) MCS lines across the Derveni segment. Labels are the same as in Figure 5.2. D=Derveni fault.

Figure 5.4 Un-interpreted (A) and interpreted (B) MCS lines across the Sithas segment. Labels are the same as in Figure 5.2. X=Xylocastro fault; S=Sithas fault.

Figure 5.5 Un-interpreted (A) and interpreted (B) MCS lines across the Xylocastro-Perahora segment. Labels are the same as in Figure 5.2. X=Xylocastro fault; K=Kiato fault; P=Perahora fault; L=Loutraki fault; PP=Peloponnesus Peninsula.

Figure 5.6 Un-interpreted (A) and interpreted (B) east west oriented tie lines across the Gulf of Corinth. These three MCS lines provide a view of the variable

along-axis architecture of the Gulf. Note the locations of thick sediment sections and sags as well as intra-basement reflectors (i.e. CDP 550, L07).

Figure 5.7 Block model illustrating fault rotation. When extension is initiated, a set of parallel, high angle normal faults form. Slip results in the rotation of these faults in the 'domino block' style of extension and sediment accumulates on the fault hanging walls. Eventually, the faults rotate to an orientation in which they can no longer slip and a new, high-angle set of faults forms resulting in complex interactions between the old and new faults and sediments [e.g. Gibbs, 1984].

Figure 5.8 A) Un-interpreted and B) interpreted post-migration, depth-converted MCS lines from each segment in the Gulf. Interpreted features in Figure 5.8B include major faults, the basement, and the seafloor. These depth conversions aid in showing the 'true' dips of structures, synrift sediment thicknesses, and depths to and beneath the basement. Apparent dips are labeled on L06d because the MCS line orientation is oblique to the strike of the Perahora fault.

Figure 5.9 Previous models for deformation in the Gulf of Corinth. A) Shallow, low-angle detachment model [Sorel, 2000]. Top diagram is a geologic cross section from the Peloponnesus Peninsula. Bottom diagram shows the inferred location of the detachment fault extending beneath the Gulf and defined by micro earthquakes. Some of the EW0108 MCS data resembles the boxed region. B) Deep detachment model [Rigo *et al.,* 1996] based on microseismicity and geologic mapping in the western Gulf. High angle faults extend from the surface to 6-11-km-depth where they intersect an active detachment fault. The clusters of micro-earthquakes might defined the region where the high angle faults intersect the detachment. C) Westaway [2002] reinterpreted the geologic cross section from Figure 5.9A without invoking a shallow, low-angle detachment. Instead, Westaway [2002] proposes multiple generations of cross-cutting, high-angle faults. D) Model of surface deformation associated with high-angle normal faulting based on the sequence of large earthquakes in 1981 in the eastern Gulf

of Corinth [Jackson *et al.,* 1982]. E) Armijo *et al.* [1996] modeled rift flank uplift and the formation of the flight of marine terraces on the PP using a thick elastic plate with a planar, high-angle (~50°) fault that cuts through the entire brittle crust. See the text for a more detailed discussion of these models with respect to the EW0108 MCS dataset.

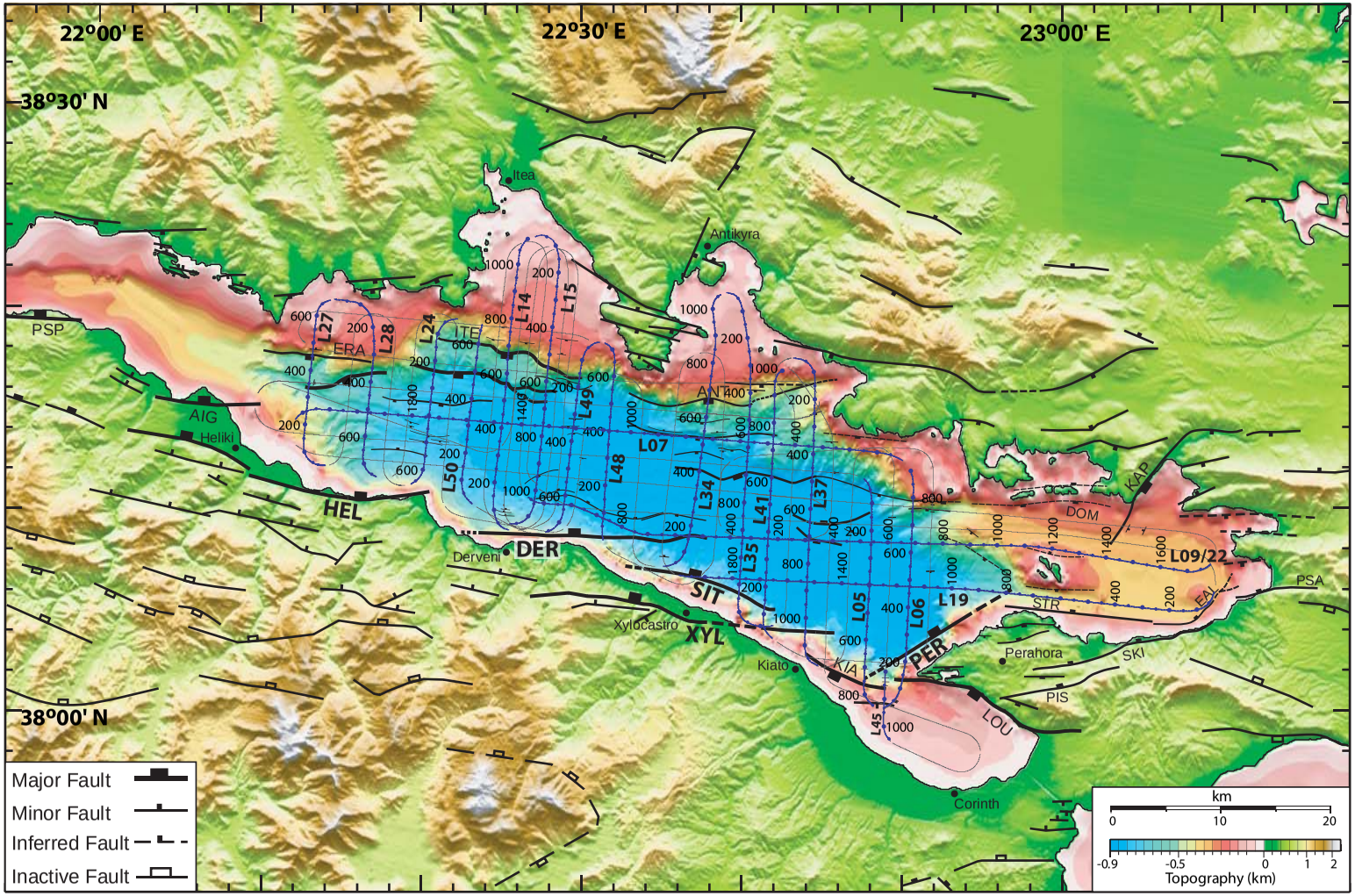
22°00' E
22°30' E
23°00' E
38°30' N
38°00' N
Itea
Antikyra
PSP
ERA
ITE
ANT
AIG
Heliki
HEL
Derveni
DER
SIT
Xylocastro
XYL
Kiato
KIA
PER
Perahora
SKI
PIS
LOU
Corinth
KAP
DOM
L09/22
PSA
EAI
STR
L19
L27
L28
L24
L14
L15
L49
L07
L48
L50
L34
L41
L37
L35
L05
L06
L45
Major Fault
Minor Fault
Inferred Fault
Inactive Fault
km
0
10
20
-0.9
-0.5
0
1
2
Topography (km)

Figure 5.1

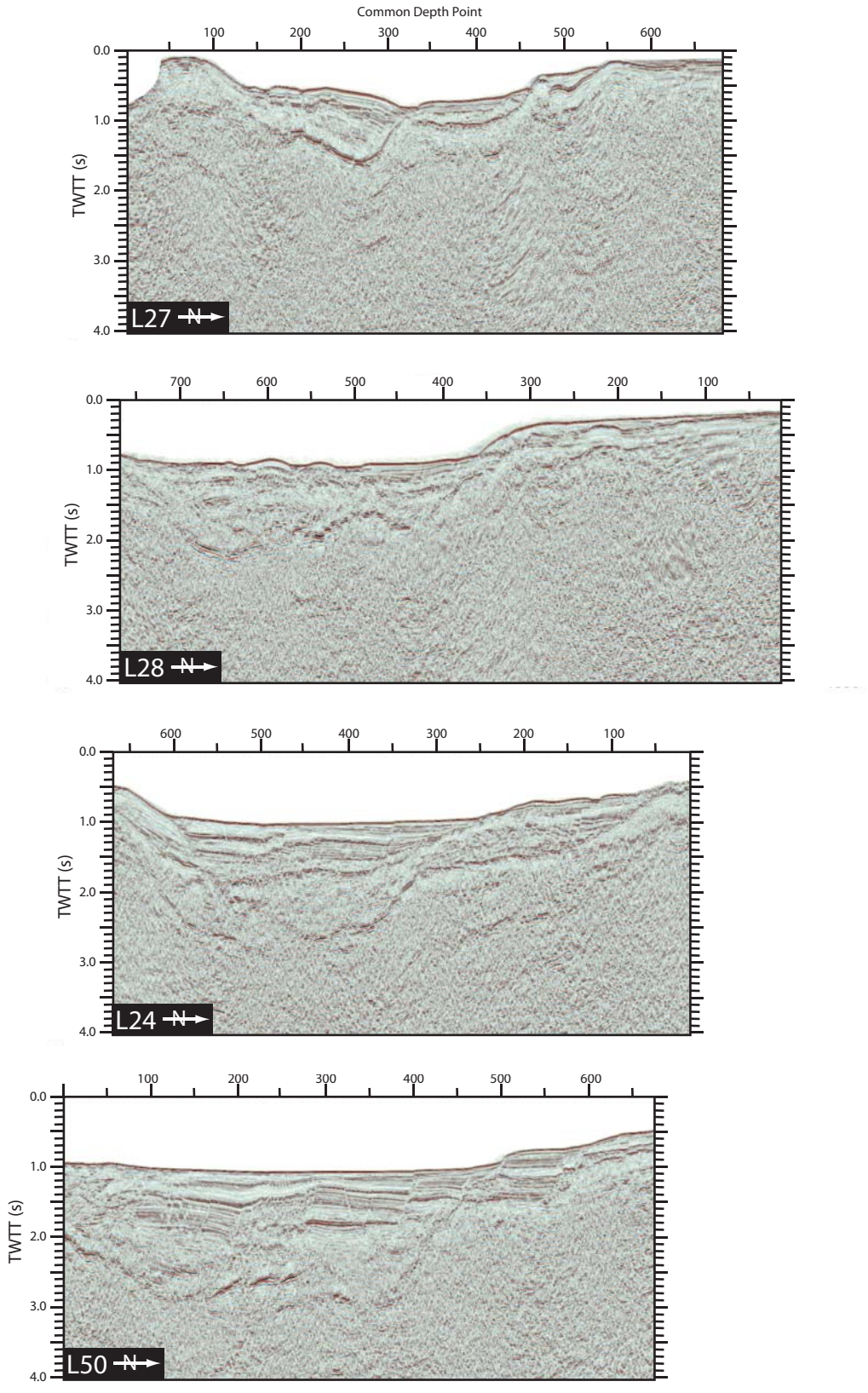
Common Depth Point
100
200
300
400
500
600
0.0
1.0
2.0
3.0
4.0
TWTT (s)
L27
N
700
600
500
400
300
200
100
L28
L24
L50

Figure 5.2A

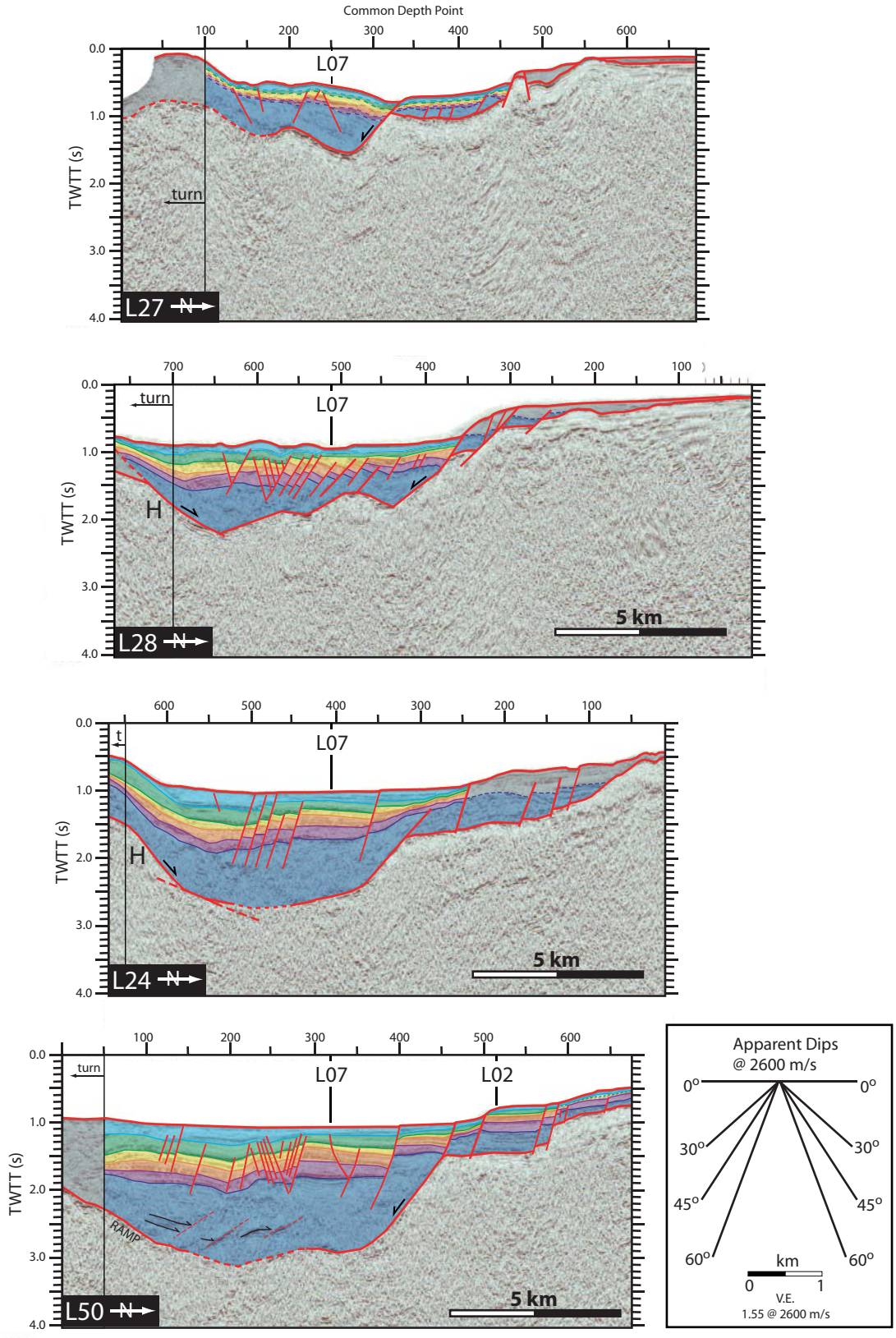
Common Depth Point
100
200
300
400
500
600
0.0
1.0
2.0
3.0
4.0
TWTT (s)
L07
turn
L27
N
700
600
500
400
300
200
100
turn
L07
H
L28
N
5 km
600
500
400
300
200
100
t
L07
H
L24
N
5 km
100
200
300
400
500
600
turn
L07
L02
RAMP
L50
N
5 km
Apparent Dips
@ 2600 m/s
0°
0°
30°
30°
45°
45°
60°
60°
km
0
1
V.E.
1.55 @ 2600 m/s

Figure 5.2B

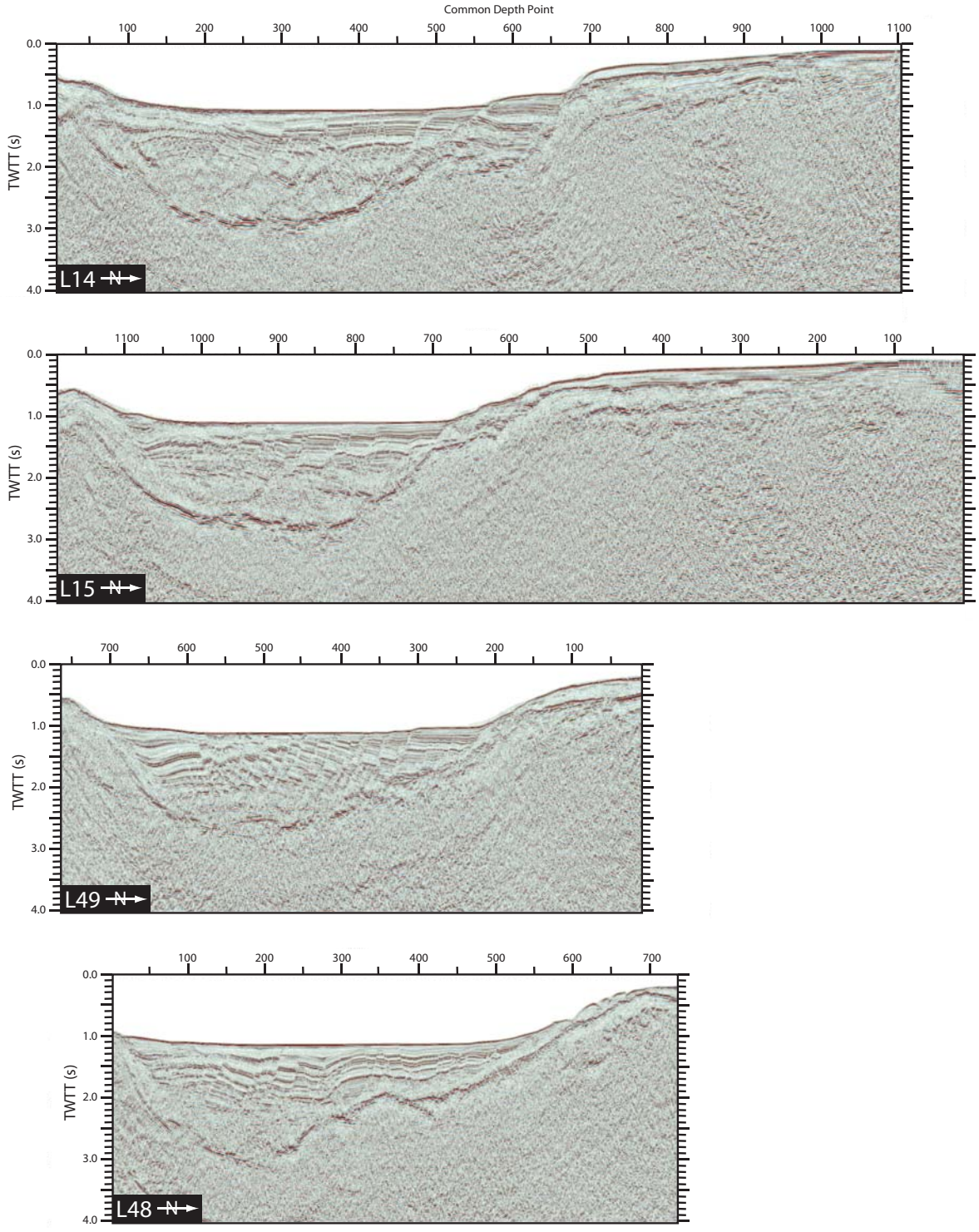
Common Depth Point
100 200 300 400 500 600 700 800 900 1000 1100
0.0 1.0 2.0 3.0 4.0
TWTT (s)
L14 N
1100 1000 900 800 700 600 500 400 300 200 100
0.0 1.0 2.0 3.0 4.0
TWTT (s)
L15 N
700 600 500 400 300 200 100
0.0 1.0 2.0 3.0 4.0
TWTT (s)
L49 N
100 200 300 400 500 600 700
0.0 1.0 2.0 3.0 4.0
TWTT (s)
L48 N

Figure 5.3A

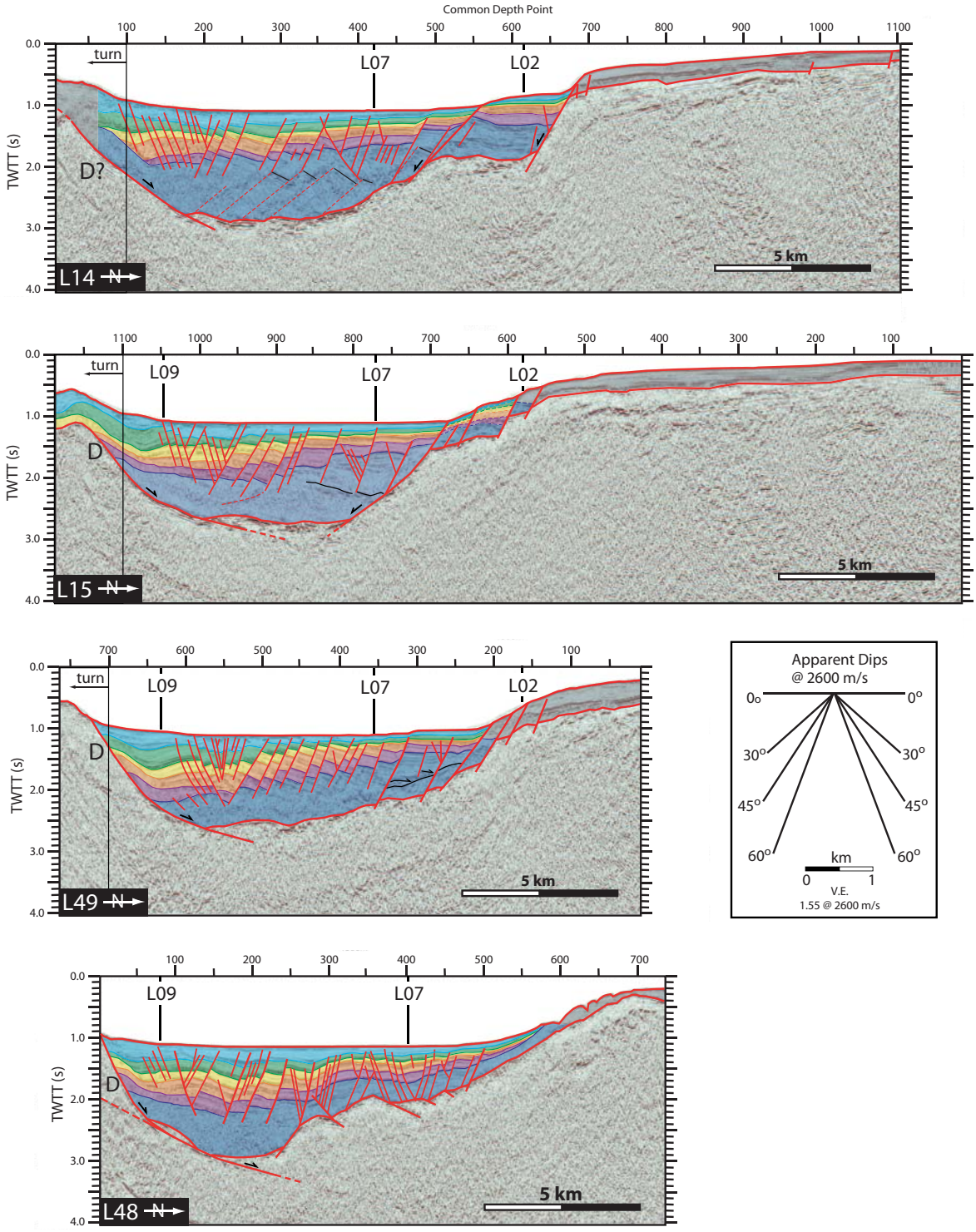
Common Depth Point
100
200
300
400
500
600
700
800
900
1000
1100
turn
L07
L02
D?
TWTT (s)
0.0
1.0
2.0
3.0
4.0
5 km
L14
N
1100
1000
900
800
700
600
500
400
300
200
100
turn
L09
L07
L02
D
TWTT (s)
5 km
L15
N
700
600
500
400
300
200
100
turn
L09
L07
L02
D
TWTT (s)
5 km
L49
N
Apparent Dips
@ 2600 m/s
0o
0°
30°
30°
45°
45°
60°
60°
km
0
1
V.E.
1.55 @ 2600 m/s
100
200
300
400
500
600
700
L09
L07
D
TWTT (s)
5 km
L48
N

Figure 5.3B

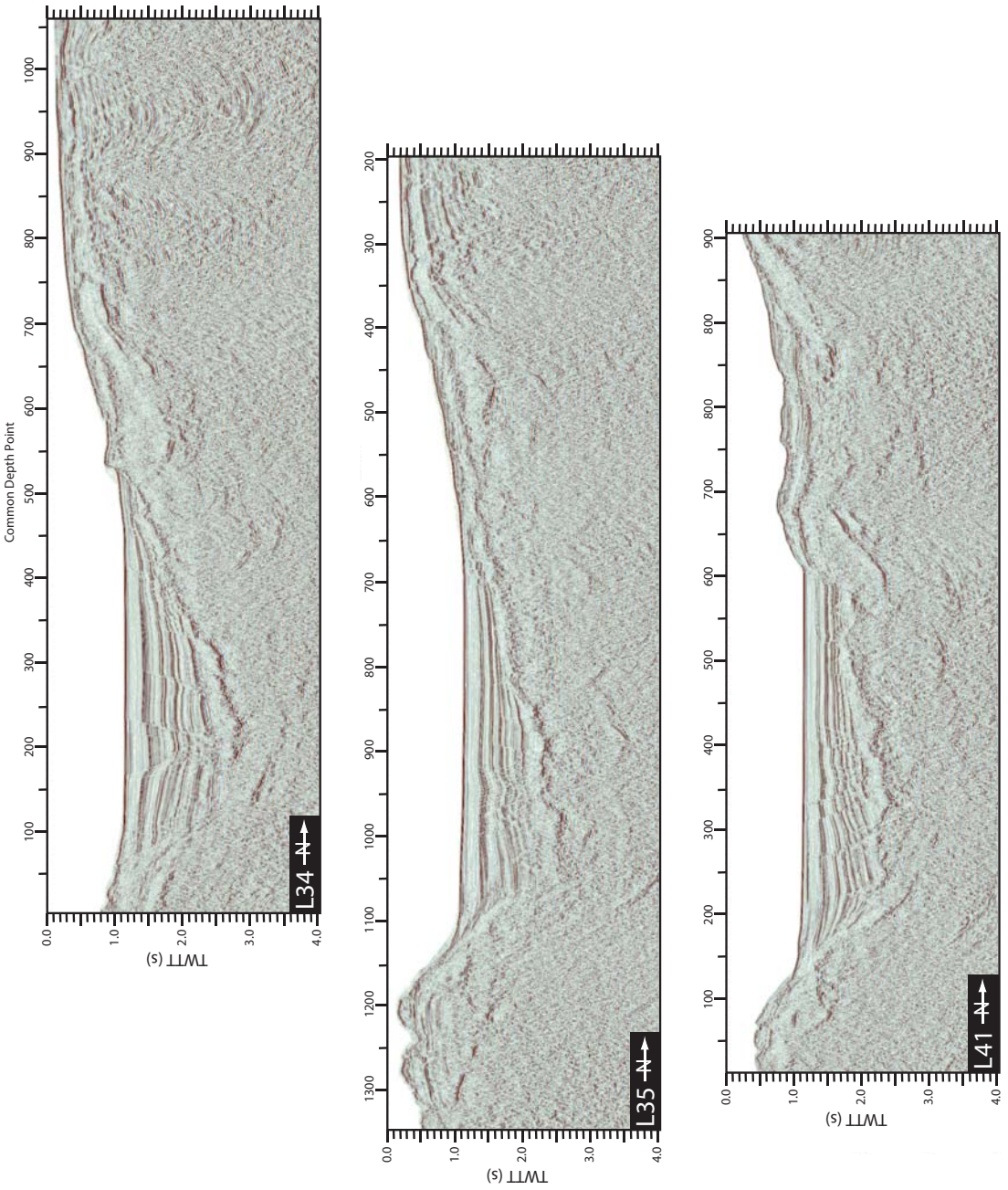
Common Depth Point
100
200
300
400
500
600
700
800
900
1000
TWTT (s)
0.0
1.0
2.0
3.0
4.0
L34
100
200
300
400
500
600
700
800
900
1000
1100
1200
1300
TWTT (s)
0.0
1.0
2.0
3.0
4.0
L35
100
200
300
400
500
600
700
800
900
TWTT (s)
0.0
1.0
2.0
3.0
4.0
L41

Figure 5.4A

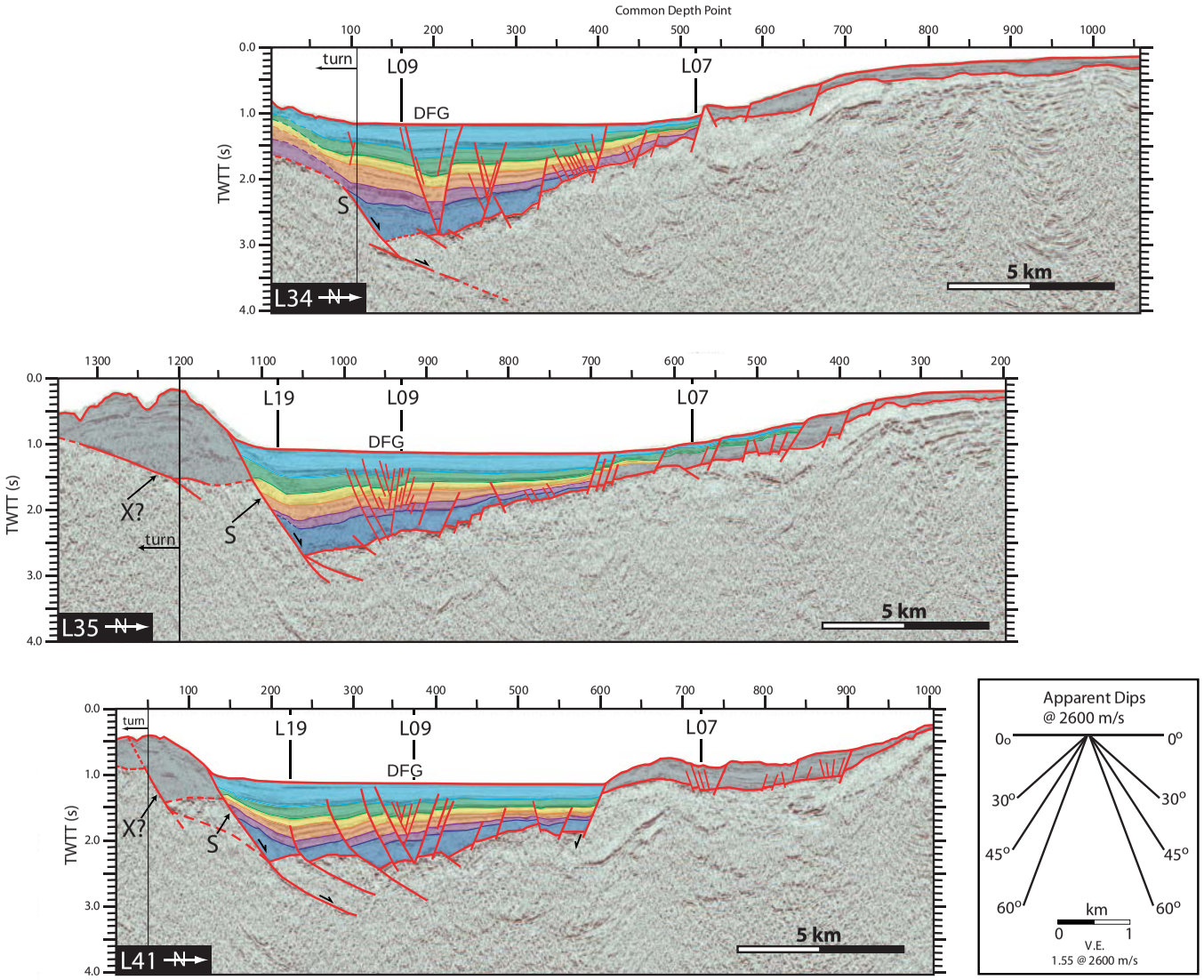
Common Depth Point
100
200
300
400
500
600
700
800
900
1000
0.0
1.0
2.0
3.0
4.0
TWTT (s)
turn
L09
L07
DFG
S
L34
N
5 km
1300
1200
1100
1000
900
800
700
600
500
400
300
200
L19
L09
L07
DFG
X?
S
turn
L35
N
5 km
100
200
300
400
500
600
700
800
900
1000
turn
L19
L09
L07
DFG
X?
S
L41
N
5 km
Apparent Dips
@ 2600 m/s
0o
0°
30°
30°
45°
45°
60°
60°
km
0
1
V.E.
1.55 @2600 m/s

Figure 5.4B

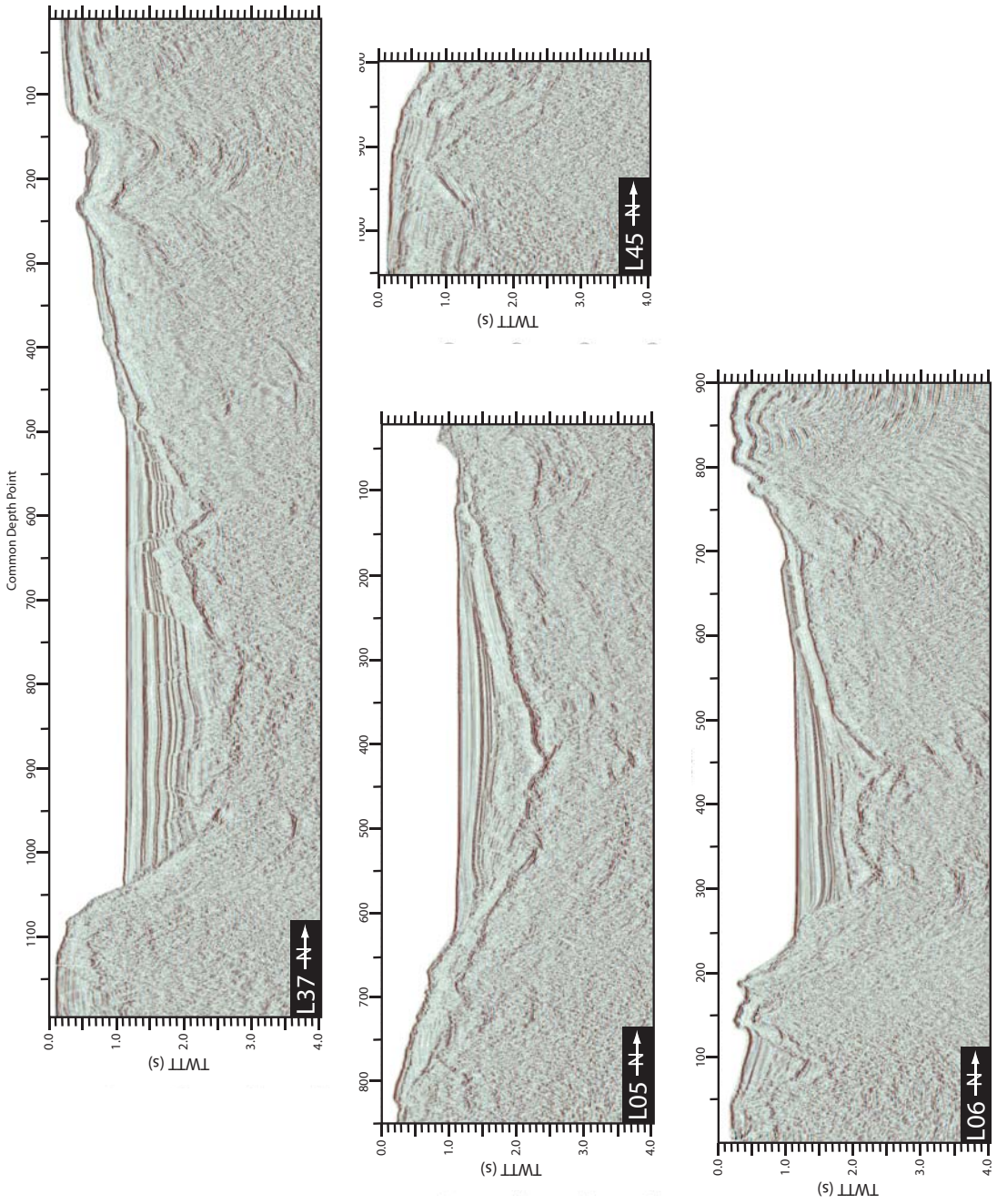

Figure 5.5A

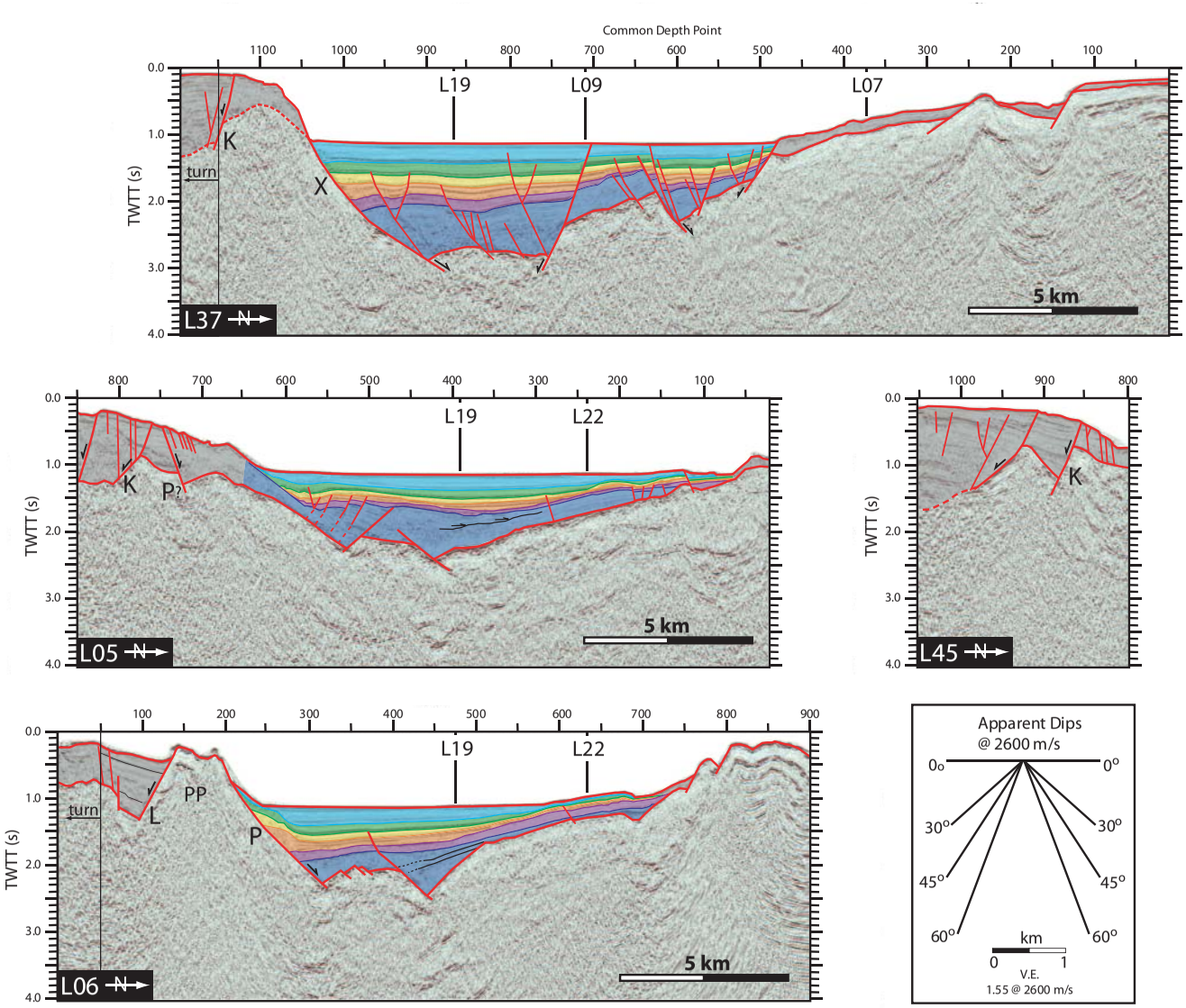
Common Depth Point
1100
1000
900
800
700
600
500
400
300
200
100
0.0
1.0
2.0
3.0
4.0
TWTT (s)
L19
L09
L07
K
turn
X
5 km
L37
800
700
600
500
400
300
200
100
L19
L22
K
P?
5 km
L05
1000
900
800
K
L45
100
200
300
400
500
600
700
800
900
L19
L22
turn
L
PP
P
5 km
L06
Apparent Dips
@ 2600 m/s
0o
0°
30°
30°
45°
45°
60°
60°
km
0
1
V.E.
1.55 @ 2600 m/s

Figure 5.5B

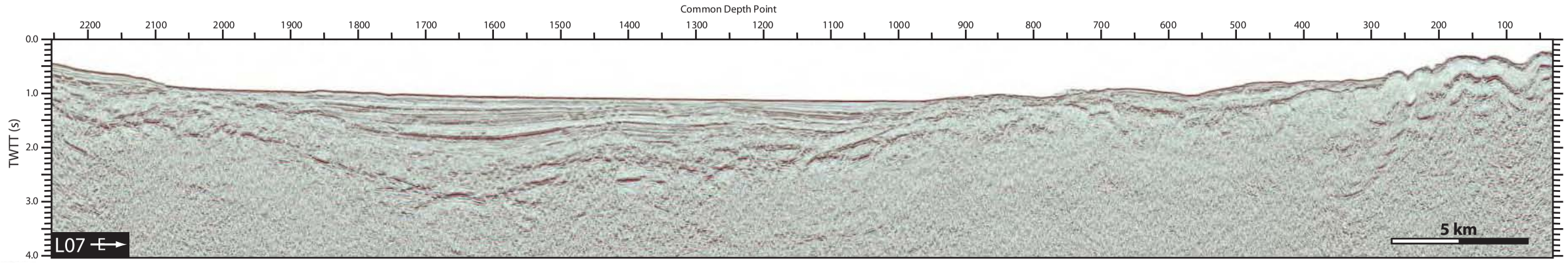
Common Depth Point
2200 2100 2000 1900 1800 1700 1600 1500 1400 1300 1200 1100 1000 900 800 700 600 500 400 300 200 100
TWTT (s)
0.0 1.0 2.0 3.0 4.0
L07
5 km

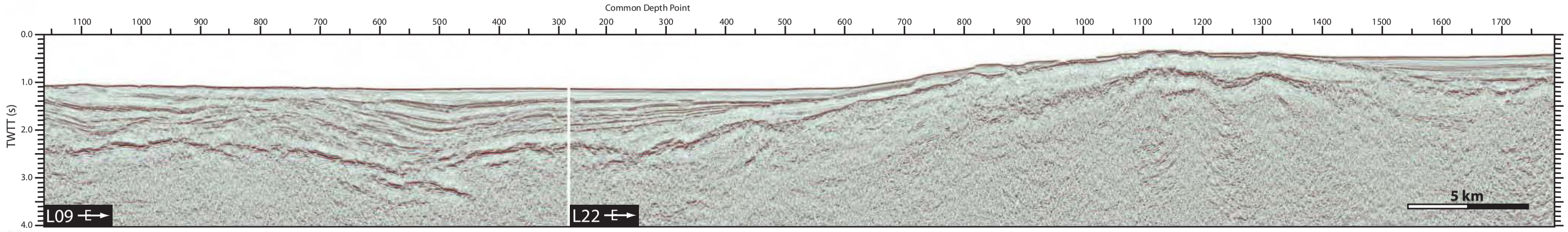
Common Depth Point
1100 1000 900 800 700 600 500 400 300 200 300 400 500 600 700 800 900 1000 1100 1200 1300 1400 1500 1600 1700
TWTT (s)
0.0 1.0 2.0 3.0 4.0
L09
L22
5 km

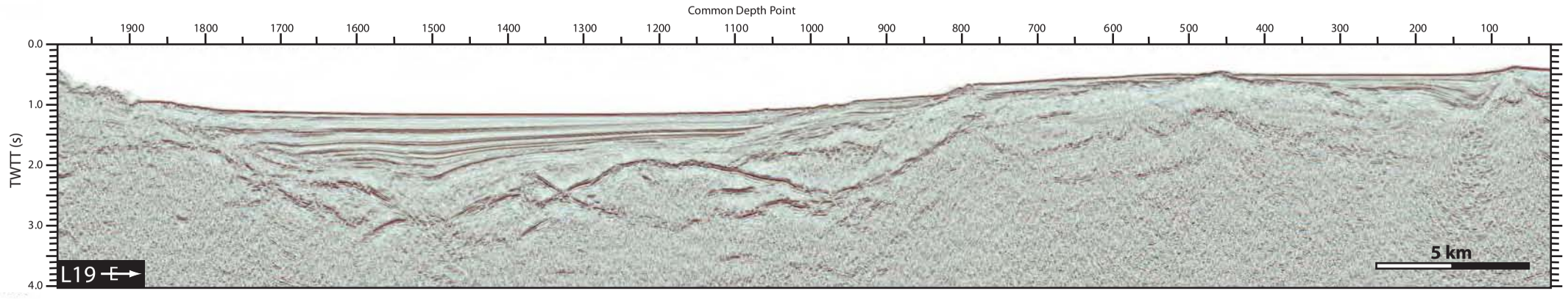
Common Depth Point
1900 1800 1700 1600 1500 1400 1300 1200 1100 1000 900 800 700 600 500 400 300 200 100
TWTT (s)
0.0 1.0 2.0 3.0 4.0
L19
5 km

Figure 5.6A

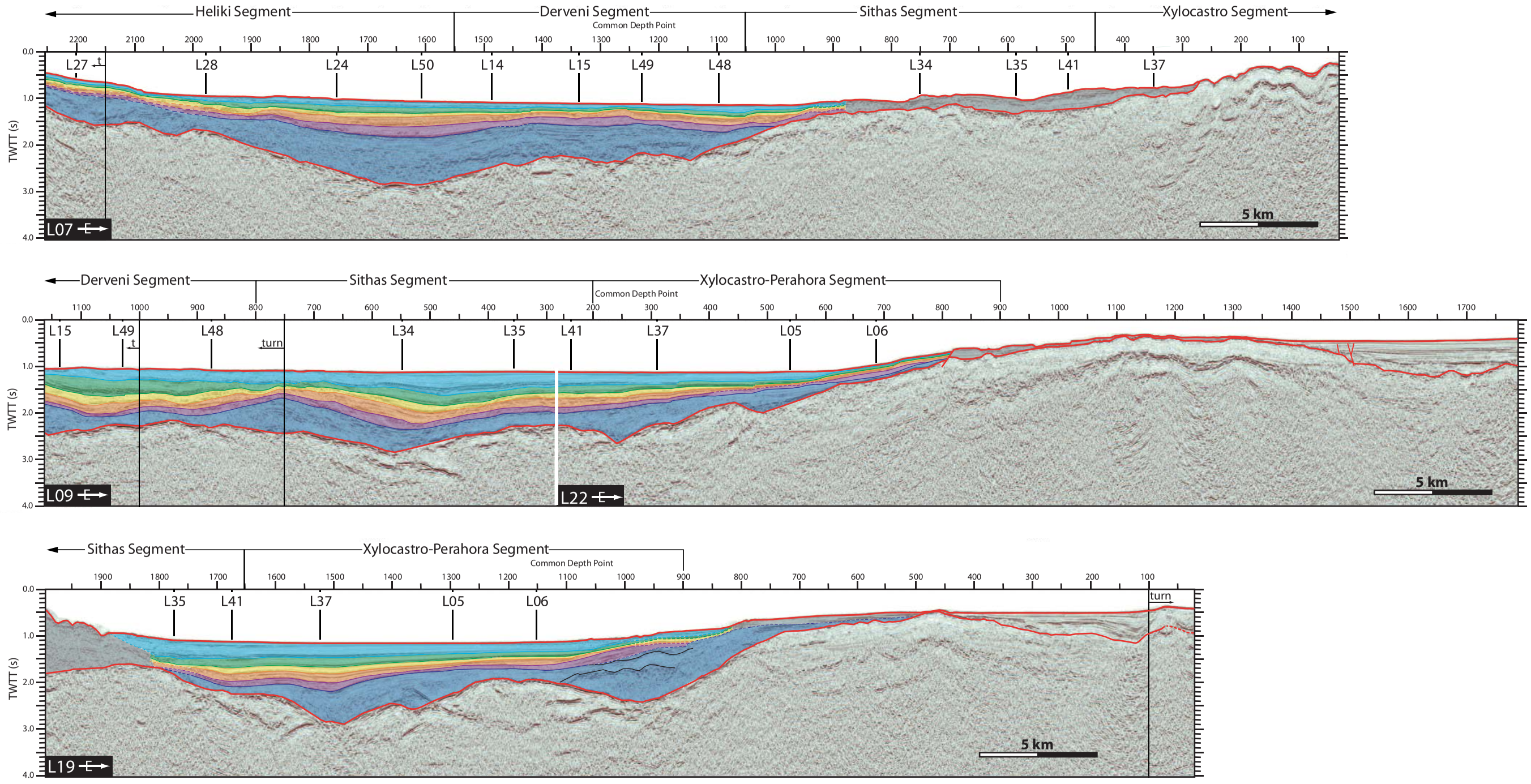
Heliki Segment
Derveni Segment
Sithas Segment
Xylocastro Segment
Common Depth Point
2200 2100 2000 1900 1800 1700 1600 1500 1400 1300 1200 1100 1000 900 800 700 600 500 400 300 200 100
L27
t
L28
L24
L50
L14
L15
L49
L48
L34
L35
L41
L37
TWTT (s)
0.0
1.0
2.0
3.0
4.0
L07
5 km
Derveni Segment
Sithas Segment
Xylocastro-Perahora Segment
Common Depth Point
1100 1000 900 800 700 600 500 400 300 200 300 400 500 600 700 800 900 1000 1100 1200 1300 1400 1500 1600 1700
L15
L49
t
L48
turn
L34
L35
L41
L37
L05
L06
L09
L22
5 km
Sithas Segment
Xylocastro-Perahora Segment
Common Depth Point
1900 1800 1700 1600 1500 1400 1300 1200 1100 1000 900 800 700 600 500 400 300 200 100
L35
L41
L37
L05
L06
turn
L19
5 km

Figure 5.6B

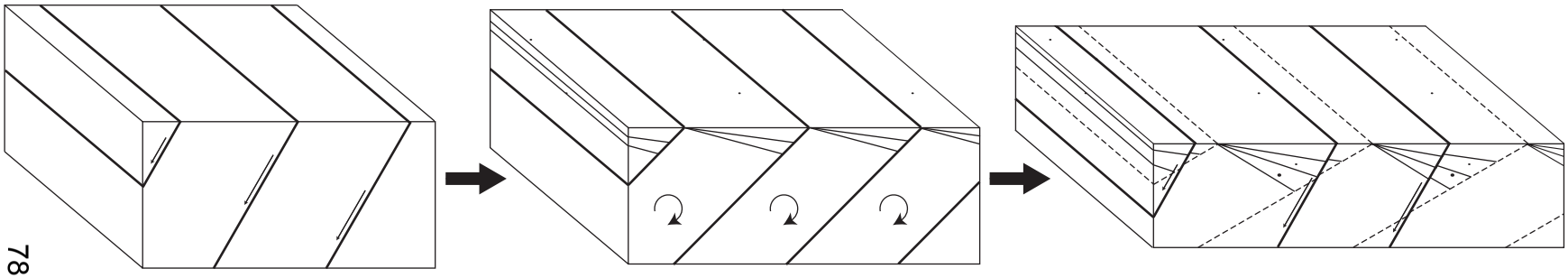

78

Figure 5.7

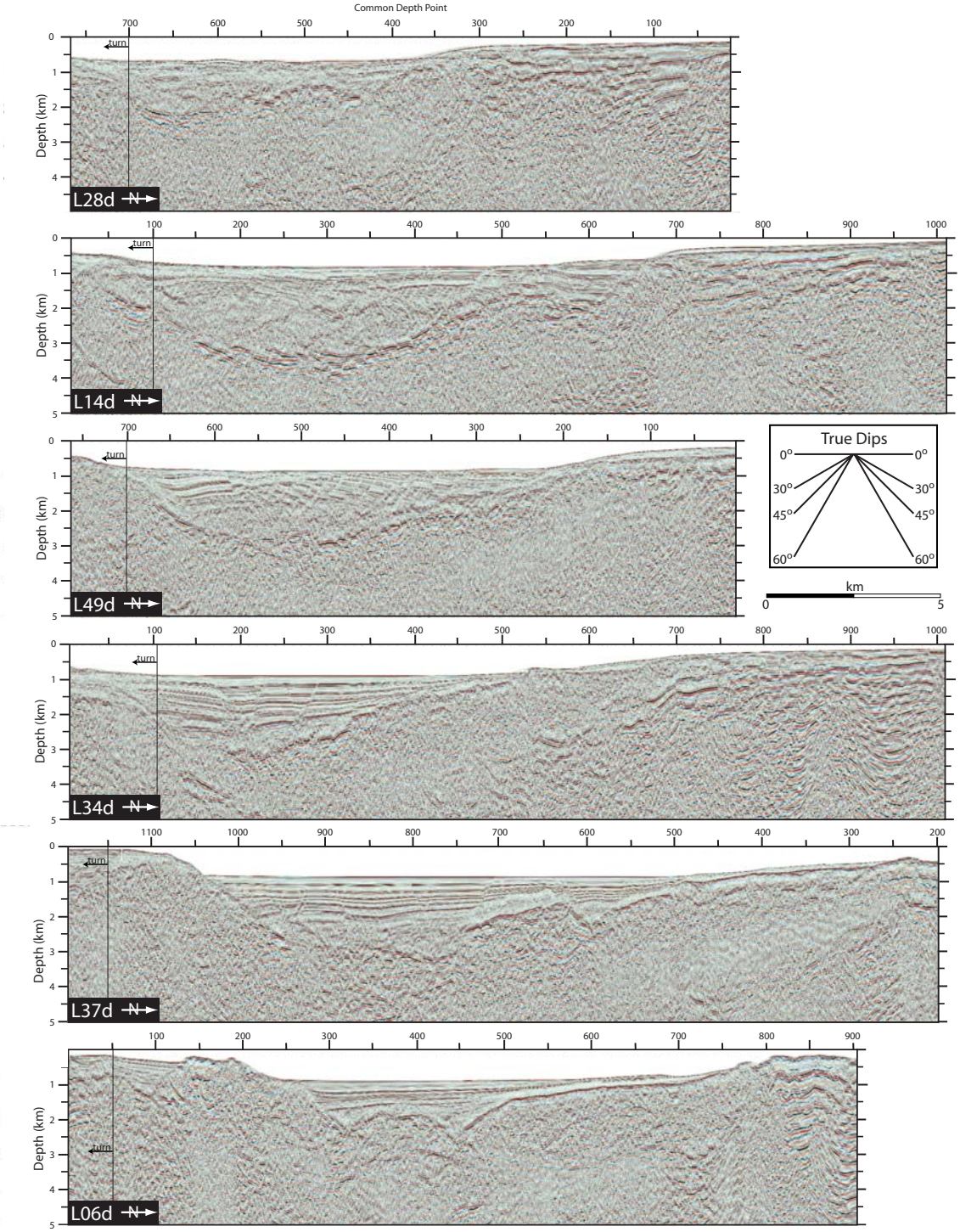
Common Depth Point
Depth (km)
turn
L28d
L14d
L49d
L34d
L37d
L06d
True Dips
0°
30°
45°
60°
km
0
5

Figure 5.8A

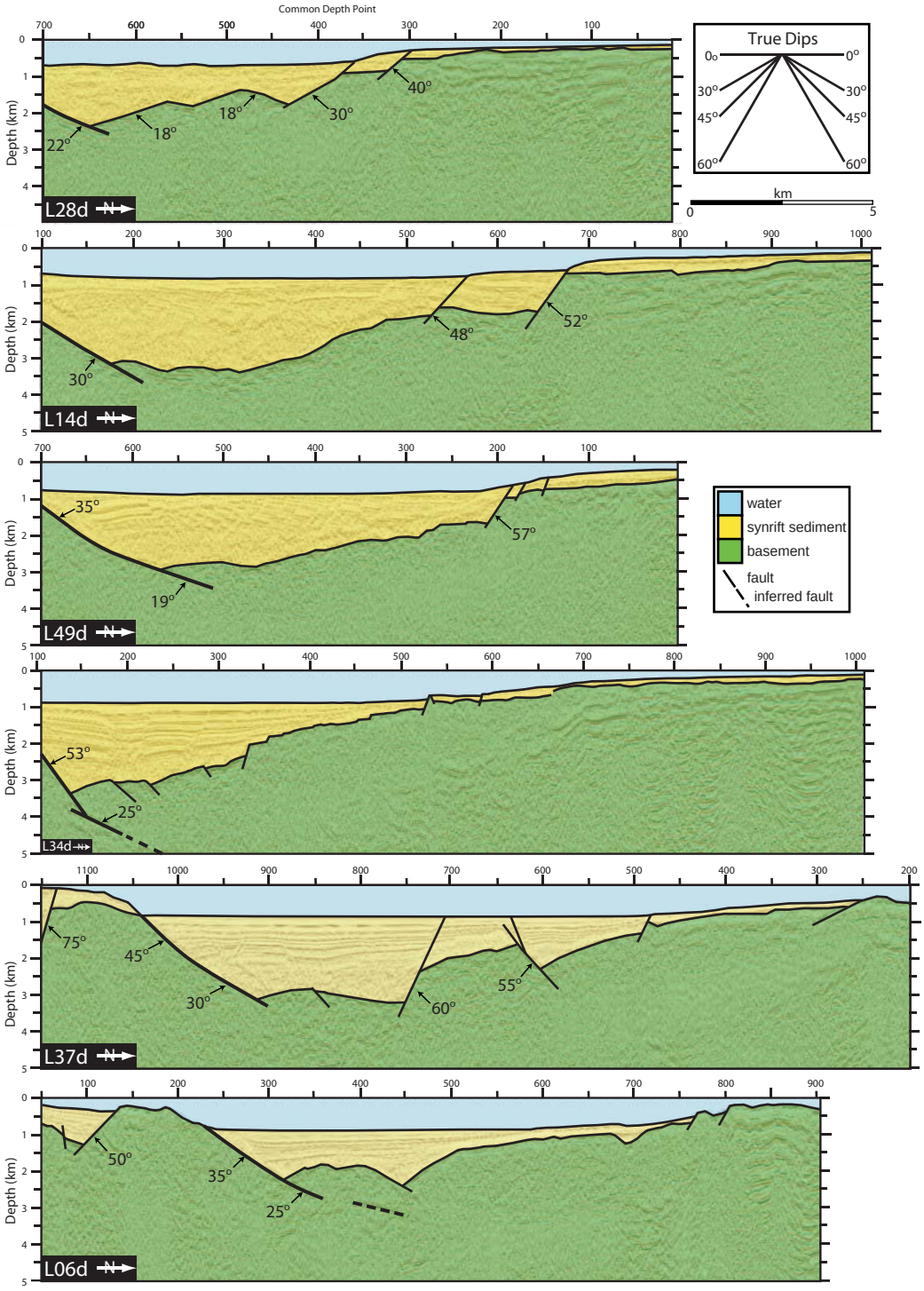
Common Depth Point
True Dips
0°
30°
45°
60°
km
0
5
Depth (km)
L28d
22°
18°
18°
30°
40°
L14d
30°
48°
52°
L49d
35°
19°
57°
water
synrift sediment
basement
fault
inferred fault
L34d
53°
25°
L37d
75°
45°
30°
60°
55°
L06d
50°
35°
25°

Figure 5.8B

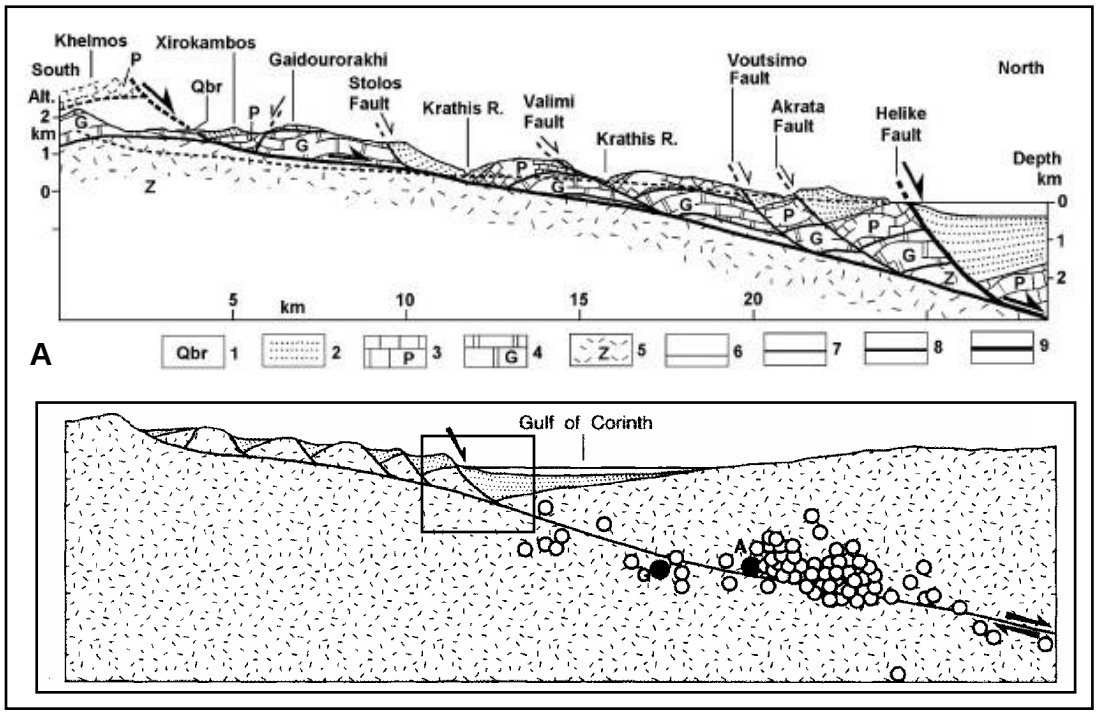
Khelmos
Xirokambos
South
P
Qbr
Gaidourorakhi
Stolos Fault
Krathis R.
Valimi Fault
Krathis R.
Voutsimo Fault
Akrata Fault
Helike Fault
North
Alt.
km
Depth km
Z
G
P
5
km
10
15
20
A
Qbr 1
2
P 3
G 4
Z 5
6
7
8
9
Gulf of Corinth

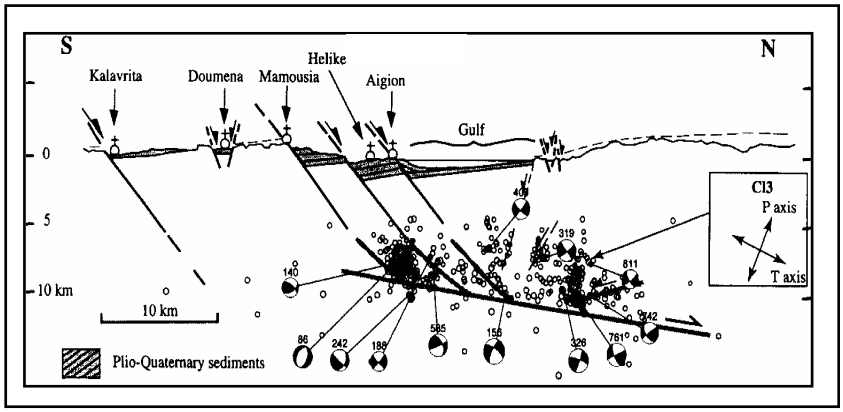
S
N
Kalavrita
Doumena
Mamousia
Helike
Aigion
Gulf
0
5
10 km
10 km
Cl3
P axis
T axis
Plio-Quaternary sediments
B

Figure 5.9

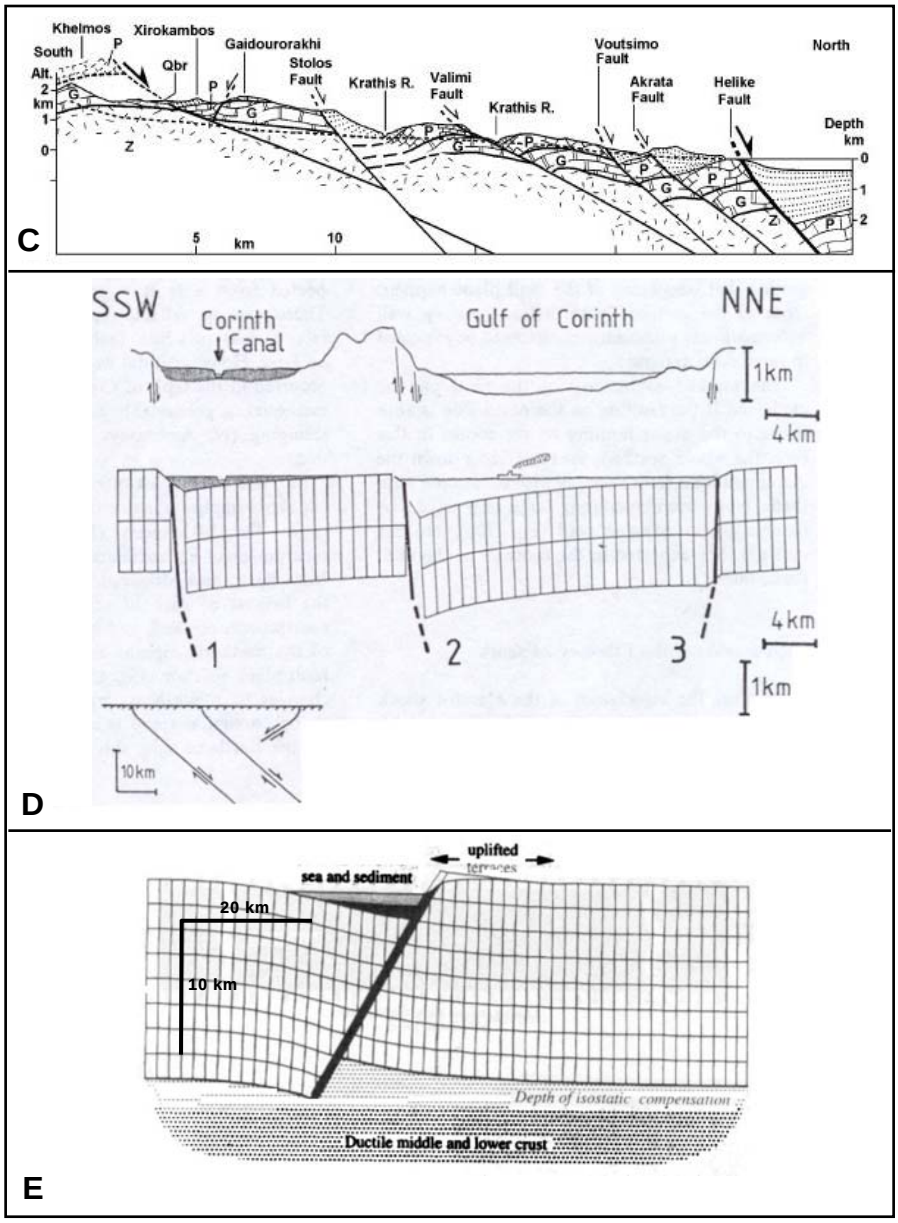

Figure 5.9 cont.

6. Sedimentation adjacent to major normal faults in the Gulf of Corinth, Greece

Introduction

The Gulf of Corinth (GOC), in central Greece, is a natural laboratory to study processes related to active continental extension. Large, seismogenic normal faults in and around the Gulf accommodate nearly one third of the ~35 mm/yr total measured displacement rate across the Aegean region [*Abers*, 2001] and many of these faults and syn-rift sediments are well-exposed and easily accessible on the Gulf margins. Work around the GOC has focused on a variety of topics, including landscape evolution related to active and inactive faults [*Doutsos and Piper*, 1990; *Jackson et al.*, 1982; *Leeder et al.*, 1991], interactions between faulting and sedimentation [*Gawthorpe et al.*, 1994; *Gawthorpe and Leeder*, 2000; *Leeder et al.*, 1991], and modeling of crustal deformation [*Armijo et al.*, 1996; *Westaway*, 2002]. Both the locations of recent earthquakes and geodetic measurements over the past 100 years suggest that deformation occurs in a narrow region beneath the Gulf where previously only a limited amount of marine geophysical data was available.

The purpose of this chapter is to shed light on interactions between faulting and sedimentation in active extensional basins using examples from the GOC based on the EW0108 grid of closely spaced multi-channel seismic (MCS) lines, a new bathymetric map, and onshore observations. I present a new fault map of the GOC followed by a brief discussion of the major faults. I then describe sedimentation at the center, ends, and between each major border fault.

The Gulf provides evidence that within a single, relatively small rift, basin filling can change dramatically over very short distances as can the geometry of major border faults that control this filling. At first glance the GOC may appear similar to other rifts but the type of along strike variability and complexity exhibited in the basin have rarely been documented and provide new insight into the complex interactions between faulting and sedimentation that can be used in the analysis of both modern and ancient extensional basins.

Surface Fault Geometry in the Gulf of Corinth

Slip along a normal fault drops the hanging wall relative to the footwall. The footwall then becomes the main sediment source for the adjacent basin although sediment can also be derived from the distal portion of the hanging wall [*Leeder and Gawthorpe*, 1987]. Along a fault, the footwall uplift and hanging wall subsidence are greatest at the center of a fault segment and decrease towards its tips [*Gawthorpe et al.*, 1994]. The simplest basin fill patterns show maximum thickness near the center of a fault and gradual thinning towards the fault tips [*Morley*, 2002]. In the GOC, a number of active faults control the current submarine basin margins and offset along each accumulates as they grow and interact at their ends. This interaction greatly affects sediment supply and dispersal.

The large border faults along the southern Gulf margin imaged in the EW0108 survey that are more than 5 km long and that dip to the north include the Heliki (HEL), Derveni (DER), Sithas (SIT), Xylocastro (XYL), and Perahora faults (PER) (Figure 6.1). These right-stepping en-echelon faults generally

overlap at their ends, although a gap is present between the ends of some (Figure 6.1). The Derveni, Sithas, and Perahora faults are submarine whereas the Xylocastro and Heliki faults have both subaerial and submarine portions. The Heliki, Derveni, and Xylocastro faults strike EW, whereas the Sithas fault strikes ESE and the Perahora fault strikes ENE.

Previous workers have mapped a single offshore Corinth fault along the southern margin between Derveni and Kiato (Figure 6.1) [*Higgs*, 1988; *Moretti et al.*, 2003; *Stefatos et al.*, 2002]. Our MCS data reveal the presence of two major south-dipping faults in addition to confirming that the Xylocastro fault extends offshore. The larger of the two, the Derveni fault, changes along its 17 km trace from a basin-bounding fault west of Derveni to a fault cutting through the entire sediment section in the hanging wall of the Sithas fault (Figure 6.1). The Sithas fault strikes N115°E and is marked by a scarp, which forms the submarine slope at the head of the large Sithas submarine fan. Onshore, south of the Sithas fault, the Xylocastro fault is subaerial and extends offshore to the east but does not merge with the Perahora fault across the entrance to the Gulf of Lechaio as has been suggested [*Armijo et al.*, 1996]. The total length of the Xylocastro fault might exceed 31 km although only ~10 km is located offshore. Elevated topography characterizes the footwall of the subaerial part of the fault (Figure 6.1). Similarly, the majority of the Heliki fault trace is subaerial except for its eastern tip. There the synrift strata in the Gulf record a history of fault growth folding associated with vertical and eastward fault propagation.

Segmented south-dipping border faults along the northern Gulf margin are numerous, vary in length, and create bathymetric scarps unless eroded by drainage features. Between 22° 10’ E and 22° 30’ E, four large faults are present in addition to many minor faults (Figure 6.1). The Eratini fault (ERA) is located south of Eratini (Figure 6.1). It originates in the west, north of the axial channel, is ~10 km long and creates a seafloor scarp at the base of the submarine shelf. The Eratini River submarine channel dissects the scarp in its center (Figure 3.3). The Itea fault (ITE) follows the 500-mbsl contour along the entrance to the Gulf of Itea (Figure 6.1). Two large, unnamed faults are located south of each of the faults just discussed. Both faults significantly offset the basement and create seafloor scarps and the one south of the Itea fault, splits into two faults at its eastern tip (Figure 6.1).

Two major faults and several smaller faults are present along the northern slope, south of Antikyra (Figure 6.1). One or possibly two segments make up the Antikyra fault that stretches across the entrance to the Gulf of Antikyra. The western portion of the fault trace is sinuous and trends ~EW whereas the eastern portion trends ~ENE and is within a similarly oriented submarine canyon (Figure 6.1). The other fault, which is unnamed, is located at the base of the submarine slope south of the eastern portion of the Antikyra fault, is 15 km long and creates a prominent bathymetric ridge accentuated to the north by small north-dipping faults. A submarine channel breaches the center of the ridge (Figure 3.3).

On the abyssal plain only a few large faults offset the seafloor (Figure 6.1) although MCS data reveal that a large number of faults, especially south of the

Gulf of Itea, terminate directly beneath the seafloor (see Chapter 5). This implies that the sediment supply is large enough and that sediment dispersal is efficient enough to “smooth out” most fault-generated topography. Only faults with relatively high slip rates are able to maintain scarps on the seafloor. The subsurface length of many faults in the Gulf is greater than their seafloor traces. This results from the offset along a fault being a maximum near the fault center, where it cuts the surface, and decreasing towards the fault tips, where it is subsurface.

Our fault map for the Gulf varies from previous efforts which have all made assumptions about fault locations and continuity based on the presence of steep slopes, steps on the seafloor, and shallow penetration seismic data. The new map (Figure 6.1) reveals the presence of five north dipping, right stepping, and echelon faults within our survey area along the southern Gulf margin. The faults vary in length and orientation. A series of smaller faults exist along the northern margin and in the central basin.

An accurate characterization of the major faults in areas where large earthquakes occur frequently is necessary for seismic hazard assessment since the size of an earthquake is related to the surface area of the fault. The Gulf of Corinth has a recorded history (since 480 B.C.E) of repeated large earthquakes that have destroyed major cities. In the last 40 years more than ten greater than Mb=5 events have occurred along faults in and around the Gulf margins (Figure 2.4). EW0108 MCS data directly image these faults and their geometries bear upon future studies of seismic hazard in the Gulf of Corinth.

Sedimentation Adjacent to Major Border Faults

Now that the fault trace geometry in the Gulf and the seismic stratigraphy (Figure 4.1) have been established, it is possible to explore sedimentation adjacent to the major border faults and then the smaller faults in the northern and central Gulf. Different sedimentation patterns exist on the hanging walls of the southern border faults. These differences relate to fault growth and provide constraints on the border fault geometry proposed above. Importantly, the differences illustrate the many responses of sediment delivery and deposition to the slip and growth of faults. Sedimentation with respect to the center and ends of each major border fault, from west to east, are the focus of the following sections.

The Heliki Fault

The Heliki fault controls 25 km of the southern margin until terminating offshore (Figure 6.1). The fault is segmented and dissected by rivers that originate many kilometers to the south, incise prominent valleys on the Peloponnesus Peninsula, and change course only slightly across the fault indicating that they formed prior to the fault. Sediment carried by these rivers constructs large fan deltas and a large submarine fan on the Heliki fault footwall. However, a prominent system of channels and canyons that flow eastward, toward the central basin, incise the submarine fan, indicating that erosion as well as deposition characterizes the basin floor adjacent to the center of the Heliki fault.

Unfortunately, none of the MCS lines approach close enough to the shoreline to directly image the fault at the seafloor but a recent high-resolution survey of the area confirms that the eastern tip of the fault ends just northeast of the Akrata Cape (AC, Figure 6.2A) [*McNeill et al.*, 2003]. Three MCS lines image the along-strike changes in stacking patterns in this location. Line 29 provides the clearest image of the Heliki fault (H, Figure 6.2B). In L29, strata in sequences 3-5 lap onto the top of a monocline (horizontal barbs, Figure 6.2B)) created by sequences 1 and 2 above the Heliki fault. Less than 2 km to the east, L24 images a geometry where the basin bounding fault (H) is still present but sequences 1-4 are folded and the upper portion of sequence 4 and all of sequence 5 lap onto the folded, underlying horizons (horizontal barbs, Figure 6.2C). In both of these lines (L29 and L24), the Heliki fault reaches the surface south of the termination of the MCS line (Figure 6.2A) but 2 km to the east, in L30, the fault does not. Instead, all 5 late-rift sequences create a gentle monocline above the fault tip and thicken to the north, away from the fold (Figure 6.2D).

Figure 6.2E shows the 3D geometry at the end of the Heliki fault to summarize the above observations. In this location, sediment delivery and stacking patterns are greatly influence by the vertical and lateral growth of the subaerial Heliki fault. The southern ends of lines 29, 24, and 30 (Figure 6.2B-D) image along-strike variations that result from this growth. The MCS data reveal that a growth fold [*Gawthorpe and Hardy*, 2002; *Gawthorpe et al.*, 1997; *Khalil and McClay*, 2002] is associated with the propagation of the eastern tip of the

Heliki fault. Slip along the fault, accompanied by footwall uplift, gradually diverted the course of the Kratis River to the east (Figure 6.2A). Currently, the River supplies sediment to the basin east of the tip of the surface trace of the Heliki fault (Figure 6.2A) resulting in the conformable but folded strata imaged in L30 (Figure 6.2D). The folding is due to growth of the fault at depth and the conformable strata are due to direct sediment supply from the Kratis Rivers to the basin floor. Therefore, the folded sequences that contain conformable strata in L29 and L24 (Figure 6.2B-C) were deposited when the Heliki fault was buried in those locations. When the fault broke the surface, the Kratis River and the growth fold migrated eastward. Sediment supply then became indirect and subsequent deposition resulted in on-lap of the folded strata. Eastward, from L29 to L30 (Figure 6.2B-D) the change from conformable to on-lap occurs in progressively younger sequences and has not yet occurred where the fault is subsurface and creates a growth fold in L30 (Figure 6.2D). Therefore, lateral and vertical propagation of the Heliki fault affect large-scale (MCS resolution) stacking patterns on the hanging wall of the fault.

The Derveni Fault

The Derveni Fault is the slope forming border fault along 13 km of the southern margin before it departs from the slope and continues for another 12 km into the central basin (Figure 6.1 and 6.3A). The MCS data image the fault along its entire length except for the western tip where the data do not approach close enough to the shoreline to image the up-dip portion of the fault. Bathymetric data from a high resolution survey of the region [*McNeill et al.*, 2003] are used to map

the fault trace there. The Derveni fault crops out at the base of the submarine slope in L49 and extends with a listric geometry beneath the sediment section into the basement (Figure 6.3B). The dip of the fault is ~40° at the surface and ~20° at the base of the synrift section. The top of the basement intersects the fault plane reflector at CDP 570. Near the center of the Derveni fault, sequences 3-5 are thick outboard of the fault but thin and exhibit normal drag against the fault (Figure 6.3B). Slightly north of the intersection of the top of the basement and the planar reflector (CDP 580) north- and south-dipping faults cut a broad rollover that create a series of nested grabens in the late-rift section. The faults terminate up-dip at or slightly beneath the seafloor. Erosion features within the grabens and seismic sequences that thicken on the down dropped sides of the faults and are thickest within the central graben indicate the grabens act as pathways for axial sediment transport and as a depocenter.

Sediment supply to the Gulf occurs across the Derveni fault via the Dervenios and Skoupeikos Rivers that incise canyons on the submarine slope (Figure 6.3A). The canyons are not well-imaged in the bathymetric maps here but they have been identified by previous workers [*Ferentinos et al.*, 1988]. Both rivers originate in the mountains ~10 km south of the shoreline and incise valleys that cross the Xylocastro fault, ~5 km south of the coastline, without significant changes in course (Figures 3.3 and 6.3A). The wide submarine rise and thickened sequences against the southern margin imply that these rivers are able to deliver sediment to the basin floor, creating a submarine fan at the base of the slope.

In L49, seismic sequences 1-5 exhibit normal drag against the Derveni fault. A mechanical analysis of folding associated with faults suggests that both normal and reverse drag are due to the heterogeneous displacement field that develops around an active fault [*Graseman et al.*, in preparation]. Furthermore, the analysis suggests that normal drag will occur if the angle between a marker and the fault is <30-40°. However, this model deals with deformation of pre-existing markers around a fault far from the surface whereas, in the Gulf of Corinth, the markers form after fault initiation in a depositional basin on the hanging wall of a fault at the surface. The broad roll-over anticline and crestal collapse graben imaged in L49 is typically associated with normal faults that are listric or curved at depth [*Shelton*, 1984]. Similar geometries have been produced in model experiments of initial slip on a listric fault that results in the formation of a broad roll-over in the sediment section that subsequently collapses along smaller faults as slip continues on the main fault [*McClay and Ellis*, 1987]. An MCS lines collected as part of the French-Greek SEIS-GREECE 1997 survey across the hanging wall of the Derveni fault imaged the same listric border fault and sedimentary fill geometries [*Sachpazi et al.*, 2003]. A reconstruction of this line suggests that the roll-over formed when the hanging wall was extending along the slightly curved, shallow portion of the Derveni fault whereas the crestal graben formed after the hanging wall broke away from the steep portion of the fault and dragged its keel away over low-angle portion of the fault [*Sachpazi et al.*, 2003]. Since the upper late-rift sequences thicken into the central graben, its development results in the creation of a new depocenter and sediment delivery

pathway. Both are important in the structural and stratigraphic evolution of the basin.

Where the Derveni Fault departs from the slope and approaches the western tip of the Sithas fault (SF in Figure 6.3A) the relationship between faulting and sedimentation changes dramatically. Line 33 images a portion of the Gulf where the Derveni fault cuts through the synrift section 1.5 km north of the southern margin. The Sithas fault is the southern border fault in L33. However, because the orientation of L33 changes approaching the southern margin it is hard to interpret the MCS data. Seismic sequences thin to the south, towards the overlap zone between these two faults (CDP's 650-750, Figure 6.3C), where a few small, high-angle normal faults cut the late-rift section. Seismic sequences thicken away from the overlap zone towards south-dipping faults that cut through the entire synrift section in the central basin. The thickest sediment is located on the hanging walls to these antithetic faults although locally the upper two seismic sequences thicken adjacent to both the Sithas and Derveni faults.

The submarine slope in the overlap zone is incised by channels clearly imaged at depths >300mbsl (Figure 6.3A). Despite the lack of any major rivers entering the Gulf here, the channels and hummocky submarine slope and rise imply that drainage development exploits the overlap zone between these two faults. Unlike the larger rivers, the drainage pathways are short and originate very close to the shoreline on the hanging wall of the Xylocastro fault and/or the submarine slope (Figure 6.3A).

Near the western tip of the Sithas fault, the Fonissa River incises a prominent canyon imaged in cross-section as a series of v-shaped seafloor features in L33 south of CDP 740 (Figure 6.3). The Fonissa River is similar to those that cross the Derveni fault to the west because it originates in the mountains ~10 km south of the coastline and crosses the Xylocastro fault before reaching the submarine basin.

Figure 6.3D is a simplified block model, which summarizes observations from the MCS data on the hanging wall of the Derveni fault. The front panel of the block model is a composite section, which combines characteristics of L49 (Figures 5.3 and 6.3B) in addition to other MCS lines (not shown) and the seafloor bathymetry. The shading of the seafloor correlates with the thickness of sediment in that location. Adjacent to the Derveni fault and within the series of nested grabens, the synrift section is thick. However, erosion features suggest the presence of sediment delivery channels, which transport sediment down-slope, parallel to the border fault. Canyons that incise the hanging wall of the Derveni fault deposit large submarine fans at the base of the submarine slope. Very few faults reach the seafloor south of the crestal grabens except for those along the northern margin that create seafloor scarps. A few canyons are able to breach the faults but most become redirected by the faults or exploit gaps or overlap zones between the ends of the faults.

The Sithas Fault

The Sithas fault is the basin-bounding structure south of the large Sithas submarine fan, which occupies the submarine rise along almost the entire length

of the fault. The toe of the fan is arcuate and defined by the 850-mbsl contour (Figure 6.4A). Strata exhibit normal drag against the Sithas fault, identified by the termination of strata rather than as a fault plane reflector. Only below 2 seconds two-way travel time (TWTT) is the fault directly imaged in L35 (Figure 6.4C). Less pronounced deformation characterizes the sedimentary fill on the hanging wall of the Sithas fault when compared to the Derveni fault. This results from the differences in border fault geometries between the two locations. The top of the basement approaching the southern margin in L21 and L35 (Figure 6.4B-C) intersects the high-angle portion of the border fault rather than the low-angle portion. Therefore, fault slip results in vertical motion of the hanging wall. In addition, the zone of diffuse faulting at the eastern tip of the Derveni fault creates the central graben rather than collapse of a rollover anticline. This zone widens and faults becomes more numerous between L21 and L35 (Figures 6.4B-C). Despite these differences, sequences clearly thicken towards the southern margin and only slightly within the central graben.

The Sithas submarine fan, fed by both the Sithas and Agiortikos Rivers and their submarine canyons, is widest adjacent to the center of the Sithas fault. The Sithas River originates ~20 km south of the Gulf whereas the Agiortikos River originates less than 10 km south of the Gulf and crosses the eastern tip of the Sithas fault. Similarly, the Fonissa River originates less than 10 km south of the Gulf and crosses the western tip of the Gulf. The submarine canyon associated with Agiortikos River (AR, Figure 6.4C) is one of the most prominent canyons along the southern Gulf margin and is imaged in L35 as an ~200 m

deep feature cut through well-stratified sediments on the hanging wall of the Sithas fault.

The Xylocastro fault is present south of the Sithas fault (Figure 6.4). Stacking velocities support the interpretation that a thick sediment section sits on top of the elevated basement block between the Xylocastro and Sithas faults. Refer to Chapter 5 for a more detailed discussion of these relationships.

Figure 6.4D is a simplified block model, which summarizes characteristics from the hanging wall of the Sithas fault. The faults along the southern margin are the subaerial Xylocastro fault, which approaches the shoreline to the east, and the submarine Sithas fault. The shelf is broad on the footwall of the Sithas fault and sediment delivery pathways incise both the Xylocastro and Sithas faults before delivering sediment to the large Sithas fan at the base of the submarine slope. The most pronounced synrift thickening occurs on the immediate hanging wall of the Sithas fault and the small nested grabens created by the tip of the Derveni fault have a small influence on sediment thickness in the central basin. Although some faults create scarps along the northern margin, many canyons and channels incise the submarine slope and deliver sediment to the basin floor.

The Xylocastro and Perahora Faults

Both the Xylocastro and Perahora faults have been the focus of studies relating to footwall uplift [*Armijo et al.*, 1996; *Flotte et al.*, 2001; *Leeder et al.*, 2003]. Of note is the study by Armijo et al. [1996], which mechanically modeled uplift and calculated deformation rates along the Xylocastro fault by incorrectly proposing that the fault extends across the mouth of the Gulf of Lechaio and

connects with the Perahora fault. With very little constraint on the submarine fault structure, the model predicted a synrift sediment thickness of ~5 km, almost twice the actual thickness.

Line 37 (Figures 6.5A,B) provides the clearest image of the Xylocastro fault where it extends offshore from near the mouth of the Agiortikos River to the east for 9 km near the base of the E-W trending submarine slope. Stratigraphic relationships on the hanging wall of the Xylocastro fault in this location (L37) are unique. Rather than exhibiting the thinning and/or normal drag in other parts of the basin, sequences maintain a constant thickness across the entire hanging wall and drag only slightly against the Xylocastro fault (Figure 6.5B).

Line 42 images the eastern tip of the Xylocastro Fault where sequences thin and create a small monocline towards the fault (Figure 6.5C). The monocline is most clearly developed in the reflective bases of sequences 4 and 5, which form on lap surfaces for strata in the semi-transparent portion of the sequences (horizontal barbs, Figure 6.5C). The geometry is similar, although on a smaller scale, to the on lap near the eastern tip of the Heliki fault (Figure 6.2) and may indicate folding associated with growth of the Xylocastro fault. Past the eastern tip of the fault, in L38, a broad submarine slope, distributed synrift faulting, and a shallow-dipping top of the basement beneath the sedimentary fill characterize the southern Gulf margin (Figures 6.5A and 6.5D). The basement probably acts as a slip surface in this location.

Small, north-dipping faults near the seafloor occupy a 2 km wide zone past the tip of the Xylocastro fault (CDP 130-200, Figure 6.5D). North of this

zone, south-dipping faults do not clearly intersect the basement or reach the seafloor. These faults extend from the tip of the Xylocastro fault, across the basin to the east, to the tip of the Perahora fault. Line 05 (Figure 6.5E) images these faults far from the ends of the Xylocastro and Perahora faults. Line 05 also suggests that, in this location, the early-rift sequence extends south, onto the submarine shelf and may be related to the sediment in the Gulf of Lechaio (see Figure 6.5B, F-G). Younger sequences terminate against the top of the early-rift sequence rather than against a border fault like in other parts of the Gulf. Shallow strata lap onto the reflective base of sequence 1 in two locations, above the south dipping faults and further south, near the base of the slope (horizontal barbs, Figure 6.5E). Thickening of sequences 3-5 near the base of the slope is further evidence that the basement may act as a slip surface north of the Gulf of Lechaio.

The western tip of the Perahora fault is a zone of diffuse normal faulting and sequences thicken to the north, away from this zone (L45, Figure 6.5F). Strata are less back-tilted against the south-dipping faults than in L38 and L05 probably due to the presence of the Perahora fault tip in L45 (Figure 6.5F). The Perahora fault is best imaged along strike to the east (L06, Figure 6.5G). Diffuse faulting is not associated with the center of the fault and instead sequences 1-4 thicken towards and exhibit normal drag against the Perahora fault. Horizons within sequence 1 lap onto the limb of the drag-induced fold (horizontal barb, Figure 6.5G).

In addition to the Xylocastro and Perahora faults, large, south-dipping normal faults are present across the mouth of the Gulf of Lechaio (Figures 6.5A-B, F-G). They include the Loutraki and Kiato faults and another fault ~1.5 km south of the eastern Kiato fault (Figure 6.5E). Each fault offsets the basement by >1 km and borders a thick synrift section comparable in thickness to the sediment in the main basin. The faults are active but only the Loutraki fault creates a prominent seafloor scarp along the southern Perahora Peninsula (Figure 6.5F).

Three submarine canyons enter the main basin between the Xylocastro and Perahora faults (Figure 6.5A). The westernmost two of these canyons originate as the onshore Asopos (AR) and Elisson Rivers, whereas the easternmost canyon may originate as the Raizanis, Zapantis, or Solomos Rivers, all of which enter the southern Gulf of Lechaio (Figures 3.3 and 6.5A). As opposed to the canyons that enter the Gulf between the major border faults, the Seliandros River incises a canyon on the slope as it crosses the submarine Xylocastro fault (Figure 6.5A). In contrast, only small pathways incise the slope controlled by the Perahora fault. This is probably because there is not much space for the development of large drainage systems on the relatively narrow footwall of the Perahora fault (Figures 3.3 and 6.5A).

Figure 6.5 summarizes observations from the hanging wall of the Xylocastro fault, which dies out where the orientation of the shelf edge swings to the south and a large canyon incises the shelf and forms a submarine canyon near the fault tip. Sediment is equally thick across the intra-rift graben nearest to

the southern margin, which subsides uniformly with respect to the bounding faults. Sediment also thickens within the northern intra-rift graben and is thicker than atop the central horst block. Many canyons and channels along the northern margin create a heavily incised submarine slope and supply sediment to the main basin. Canyons that drain the southern margin cross south dipping faults such as the Kiato fault in the mouth of the Gulf of Lechaio. The size of these faults and the thick sediment section on their hanging walls implies this region, south of the main basin, may act as a sediment trap.

Sediment-Filled Sags

East west oriented MCS lines outboard of the major border faults image thickening of the synrift section across broad sags (Figures 6.6 and 6.7). The thickening occurs in the central basin north of the ends of the Heliki and Derveni faults, outboard of the eastern portion of the Derveni fault where it overlaps the Sithas fault, in the intra-rift graben outboard of the Xylocastro fault (Figures 6.1 and 6.6), and on the hanging walls of two faults south of the Gulf of Itea. The synrift sediment thickness in these sags is >2 km and the sags are some of the thickest sediment accumulations in the entire Gulf. A similar feature was imaged in the Consag Basin in the northern Gulf of California and suggested to be a pull-apart basin (accommodation zone) between left-stepping transform faults [*Persaud et al.*, 2003].

Footwall uplift and hanging wall subsidence are greatest at the center of a fault segment and decrease towards its tips [*Gawthorpe et al.*, 1994]. If variations in sediment thickness reflect this aspect of fault growth, the synrift section should

reach a maximum thickness adjacent to the centers of major border faults. Therefore, sag might mark the hanging wall of the center of a large fault. Two clear examples of this exist in the Gulf, both along the northern margin, south of the Gulf of Itea.

Figure 6.7A is a portion of L02; an east west oriented MCS line that images a large portion of the hanging wall block of the Itea fault before crossing the tip of the fault near CDP 900 (Figure 6.1). Figure 6.7B is a portion of L14, which crosses the center of the Itea fault (Figures 6.1). Locally, the synrift section reaches a maximum thickness of ~1.3 km at CDP 660 in L02, on the immediate hanging wall of the Itea fault (Figure 6.7). Early-rift strata exhibit the most pronounced sagging across the basement deep in L02 and strata within this sequence lap onto and successively climb the basement reflector (horizontal barbs, Figure 6.7A). Less pronounced thickening characterizes the late-rift sequence.

The second clear example of sag located on the center of the hanging wall of a fault occurs adjacent to the large, unnamed fault immediately south of the Itea fault (Figure 6.1). Line 07 (Figure 6.6) crosses the center of the sag, which is much larger than the sag imaged in Figure 6.7. Synrift sediment thickness is ~2.3 km where L50 (Figure 5.3) intersects the sag (CDP 1590) and the early-rift sequence comprises approximately ¾ of this thickness.

Interpretation of the other two sags (Figure 6.6B-C) is not as straightforward. The sag centered at CDP 500 in L18 (Figure 6.6B) occurs outboard of the Derveni fault, where the fault cuts through the center of the basin

(Figure 6.1). In both L07 and L18 (Figure 6.6A-B), the synrift section in the center of the sags reaches comparable thicknesses of ~2.3 km. However, in L18, the late-rift section comprises most of the sag, opposite the case in L07. Cleary, the sag imaged in L18 is a late-rift feature associated with growth of the Derveni fault. The proximity of the Sithas fault tip, ~3 km south and slightly east of the sag, could also influence sediment thicknesses in the sag if the fault slip profiles overlap. In contrast, the sag in L07 (Figure 6.6A), is an early-rift feature associated with the large, south dipping fault along the northern margin (see L50, Figure 5.2), which has remained active during deposition of the late-rift section. However, relative thicknesses of the early- and late-rift sections on the hanging wall of the fault suggest the fault slip rate has decreased. Chapter 5 discusses the prominence of northern margin faults during deposition of the early-rift section in further detail.

The sag in L19 (Figure 6.6C) centered at CDP 1520 occurs outboard of the Xylocastro fault, in the intra-rift graben imaged in L37 (Figure 5.5). No clear intra-basement reflectors mark the location of the Xylocastro fault in L37, L42 (Figure 5.5), or in L19 (Figure 6.6C). The maximum sediment thickness across the sag is ~2.3 km, divided almost equally between the early- and late-rift sections. Most of the sagging occurs within the early-rift sequence and sequences 1 and 2 in the late-rift section whereas the shallower late-rift sequences do not thicken across the sag (see Figure 5.6 for an interpreted version of L19). The thickening at the base of the late-rift section may be associated with the synrift fault at CDP 850 in L37 (Figure 5.5) and the sag in

general appears associated with subsidence of the intra-rift graben on the hanging wall of the submarine portion of the Xylocastro fault.

In summary, the four sediment-filled sags imaged in the Gulf of Corinth all appear to be associated with the hanging walls of normal faults and the size of the sags is directly proportional to the size of the faults. For example, small sag characterizes the hanging wall of the relatively small Itea fault, whereas broad and deep sags characterize the hanging walls of the large border faults along the southern margin and the large, unnamed fault, south of the Itea fault, along the northern margin. Curiously, the maximum sediment thickness (~2.3 km) in the center of the sags is similar although they occur with respect to different faults. In addition, the difference in relative thicknesses of the early-and late-rift sections reveal temporal variations in fault growth. For instance, the sags on the hanging wall of the Itea fault (Figure 5.7), the unnamed fault to the south (Figure 5.6A), and the Xylocastro fault (Figure 5.6C) exhibit the majority of thickening and sagging in the early-rift and base of the late-rift sections. These observations imply the majority of fault growth took place during those periods of deposition. In contrast, thickening within the sag on the hanging wall of the eastern portion of the Derveni fault (Figure 6.6B) indicates late-rift fault growth. The sag is not present across the entire hanging wall of the Derveni fault and isopach maps (not shown) suggest recent linkage of the basin-bounding portion of the Derveni fault with the eastern portion of the fault. Therefore, although the sag is associated with the western portion of the fault, it still may mark the center of the fault prior to fault linkage.

The presence of sediment-filled sags imaged in the Gulf of Corinth indicates fault growth in accordance with the typical slip distribution along a fault that reaches a maximum in the center of the fault and decreases towards the fault tips. Identification of sediment-filled sags in other basins can contribute to locating faults and the relative thicknesses of seismic sequences within the sags can aid in constructing fault growth histories.

Summary and Conclusions

The relationship between faulting and sedimentation varies across the Gulf of Corinth adjacent to the five large, north-dipping border faults along the southern Gulf margin, which are right-stepping and en-echelon. This arrangement may reflect N-S directed extension that is oblique to the NW-SE trending basement fabric. The faults are, from west to east, the Heliki, Derveni, Sithas, Xylocastro, and Perahora faults. They interact and/or overlap at their ends. The Xylocastro fault extends offshore near the Agiortikos River but does not link with the Perahora fault across the entrance to the Gulf of Lechaio. Between the two faults, the basement is shallow and small normal faults cut the synrift section. Three large, south-dipping faults create >1 km of basement offset at the entrance to the Gulf of Lechaio. The Derveni and Sithas faults are separate basin-bounding structures and the Derveni fault departs from the coastline and cuts through the central basin where it overlaps the Sithas fault. Other faults are present along the northern margin and within the central basin, many of which create bathymetric scarps and/or ridges on the basin floor. The

faults interact with sediment delivery pathways and affect sediment supply to the flat central basin where sedimentation outpaces local vertical fault growth.

Variations in fault length, shape, age, and position all affect sediment deposition and stratigraphic patterns on the hanging walls to these faults. Major border faults in the Gulf exhibit unique characteristics. For example, stratigraphic patterns on the hanging wall of the Heliki fault indicate the presence of a growth fold associated with lateral and vertical propagation of the fault tip (Figure 6.2). Major border faults in the Gulf also exhibit similar characteristics. For example, on the hanging walls of the Derveni and Sithas faults, strata exhibit normal drag before terminating against the fault. In addition, on-lap of folded or dragged strata in a few locations indicates that filling of space adjacent to fault-generated folds is important and that the resulting stacking patterns are recognizable at the scale of the MCS data and infers fault growth. In general, sediment thickness increases towards and is greatest on the hanging walls in the centers of the major faults whereas the synrift section thickens away from the ends of the faults towards antithetic faults in the central basin. Variations on this general theme, such as on the hanging wall of the eastern portion of the Derveni fault, may be due to fault linkage or significant early growth of faults that are no longer the major faults (i.e. large sag along the northern margin, Figure 6.6A).

Geometrical constraints that arise from the listric geometry of the Derveni fault (Figure 6.3B) result in a rollover anticline in the synrift section, which is faulted into a series of nested grabens due to the complex strain that results from the rollover. Consequently, maximum sediment thickness occurs in two locations,

1) above the limb of the fold nearest to the fault, and 2) within the series of nested grabens formed on top of the fold axis. This holds true along the entire length of the Derveni fault where it is a border fault (Figure 6.1).

The synrift section adjacent to the Sithas, Xylocastro, and Perahora faults shows remarkable similarities. Sediment thickness increases towards the faults and is thickest adjacent to the faults. In addition, the locations of sediment-filled sags help identify major faults and understand the growth history of the faults.

The fault geometry established in a rift basin undoubtedly controls hanging wall stacking patterns but sediment must be able to reach the basin floor. In the Gulf of Corinth, competition exists between rivers draining the Gulf margins and footwall topography created by the growth of faults. Rivers that originate >10 km south of the shoreline were established early, and now cross inactive faults on the Peloponnesus Peninsula before incising the footwalls of the major faults and supplying sediment to the basin floor. Short rivers and canyons exploit gaps and/or overlap zones between the major faults. One example exists of a river that changed its course due to vertical and lateral fault propagation. The same variations hold true for the northern Gulf margin, where canyons and channels occasionally incise fault scarps and typically exploit gaps between faults or become redirected by the growth of fault tips. Interactions between large border faults, faults on the basin floor, faults along the northern margin and sediment delivery pathways directly affect stratigraphic patterns, sediment thicknesses, and depocenter development.

In submarine rift basins, such as the Gulf of Corinth, basin filling patterns reflect the interaction between fault growth and the development of sediment delivery pathways, which provide information about the evolution of the basin. Examples from the Gulf of Corinth emphasize that in locations where multiple border faults, which vary in size and geometry, are present, sedimentation will differ adjacent to the faults. Variable development of hanging wall faults also affects sediment supply and stratigraphic patterns opposite the major border faults and in the central basin. Most of the literature on sedimentation in rift basins tends to concentrate on single or few fault systems, ignoring the complexity that may evolve in rift systems, such as the Gulf of Corinth, which typically contain a large number of faults. In these systems, large faults overlap, interact, and result in recognizable filling patters, which in cases where the major faults are unknown, can aid in constructing their geometries and growth histories.

FIGURE CAPTIONS

Figure 6.1 Shaded relief and structure map of the Gulf of Corinth. Black boxes show the locations of figures used to illustrate the relationships between faulting and sedimentation adjacent to major border faults along the southern margin. The EW0108 grid of multi-channel seismic (MCS) lines is in light gray and MCS lines discussed in the text are in blue. Black numbers denote selected common depth points (CDP's), small blue dots denote every 50th CDP, and large dots denote every 1000th CDP. CDP interval=25m. Towns referred to in the text are labeled. AIG=Aigion fault; ANT=Antikyra fault; DER=Derveni fault; DOM=Domvous fault; EAL=eastern Alkyonides fault; ERA=Eratini fault; HEL=Heliki fault; ITE=Itea fault; KAP=Kaparelli fault; KIA=Kiato fault; LOU=Loutraki fault; PER=Perahora fault; PSA=Psatha fault; PSP=Psathopyrgos fault; SIT=Sithas fault; WAL=western Alkyonides fault; XYL=Xylocastro fault.

Figure 6.2 A) Map of a portion of the central-western Gulf showing faults and MCS line locations with annotated CDP numbers. The EW0108 survey grid is in light gray. A change in course of the Kratis River is due to the lateral growth of the major, north-dipping Heliki fault. **B-D)** Multi-channel seismic (MCS) lines across this portion of the Gulf illustrate the structural and stratigraphic evolution discussed in the text. **E)** Schematic block diagram of the eastern tip of the Heliki fault. Upper inset shows a perspective view of the Heliki fault which drops the Gulf down from mountains to the south. I focus on its eastern end. Lower inset is a simplified block diagram illustrating a growth fold. Both block diagrams are modified from *Gawthorpe et al.* [1997].

Figure 6.3 A) Map of a portion of the southern Gulf showing faults and MCS line locations. Both the Dervenios and Skoupeikos Rivers cross the subaerial Xylcoastro and submarine Derveni faults before dumping sediment on the basin floor. In addition, many gullies and small canyons incise the slope at the western

end of the Derveni fault, especially where it departs from the submarine slope (22°30' N) in the east (Figure 7B). **B-C)** MCS lines located near the center of the Derveni fault (L49) and near the eastern portion of the fault (L33), in the overlap zone between the Derveni and Sithas faults. Small channels incise the seafloor in the overlap zone south of the turn (CDP 750). M=seafloor multiple. **D)** Simplified block model of sedimentation on the hanging wall of the Derveni fault. See text for discussion.

Figure 6.4 A) Map of a portion of the southern Gulf showing faults and MCS line locations. The EW0108 survey grid is in light gray. The Sithas fault controls the southern margin and the Xylocastro fault is located onshore to the south. The Sithas and Agiortikos Rivers cross both of these faults and the former feeds a large submarine fan at the base of the slope (arcuate mound defined by the 850 mbsl contour) whereas the Agiortikos river carves a deep canyon. **B-C)** The MCS data L21 and L25) image these features in addition to a basement block between the Xylocastro and Sithas faults. The package of sediment atop this block is incised by the prominent Agiortikos canyon (AR, Figure 18C). The nested series of faults in the central basin (CDP 270 in L21 and CDP 950 in L35) lie along strike from the eastern termination of the Derveni fault and are a zone of faulting that widens away from the fault tip. **D)** Simplified block model of sedimentation on the hanging wall of the Sithas fault. See text for discussion.

Figure 6.5 A) Map of the southern Gulf margin near the mouth of the Gulf of Lechaio. Major border faults in this area are the offshore extension of the Xylocastro fault and the Perahora fault. Faults to the south are large and offset the seafloor. A number of canyons exploit the zone between the Xylocastro and Perahora faults. AS=Asopos River. **B-D)** MCS lines image the Xylocastro fault as it changes along-strike from a prominent border fault **(B)** to a zone of faulting **(D)** above a shallow-dipping basement. Between these two locations, near the end of the Xylocastro fault **(C)**, the uppermost reflective units are slightly folded and semi-transparent horizons lap onto the limbs of these folds. **E-G)** MCS lines

image the basin between the ends of the Xylocastro and Perahora faults **(E)**, the western tip of the Perahora fault **(F)** and the Perahora fault and horst block between the Perahora and Loutraki faults **(G). H)** Simplified block model of sedimentation on the hanging wall of the submarine Xylocastro fault. See text for discussion.

Figure 6.6A-C) Examples of sediment-filled sags from various parts of the Gulf. Figure 6.1 shows the locations of the MCS lines. See text for discussion.

Figure 6.7 A) East-west oriented MCS Line 02 images a sag basin on the hanging wall near the center of the Itea fault. The basal sequence is substantially thicker in the center of the sag than near its margins. Drainage exploits the regions near the end of the fault. **B)** Line 14 crosses L02 through the center of the sag. Figure 6.1 shows the locations of the MCS lines.

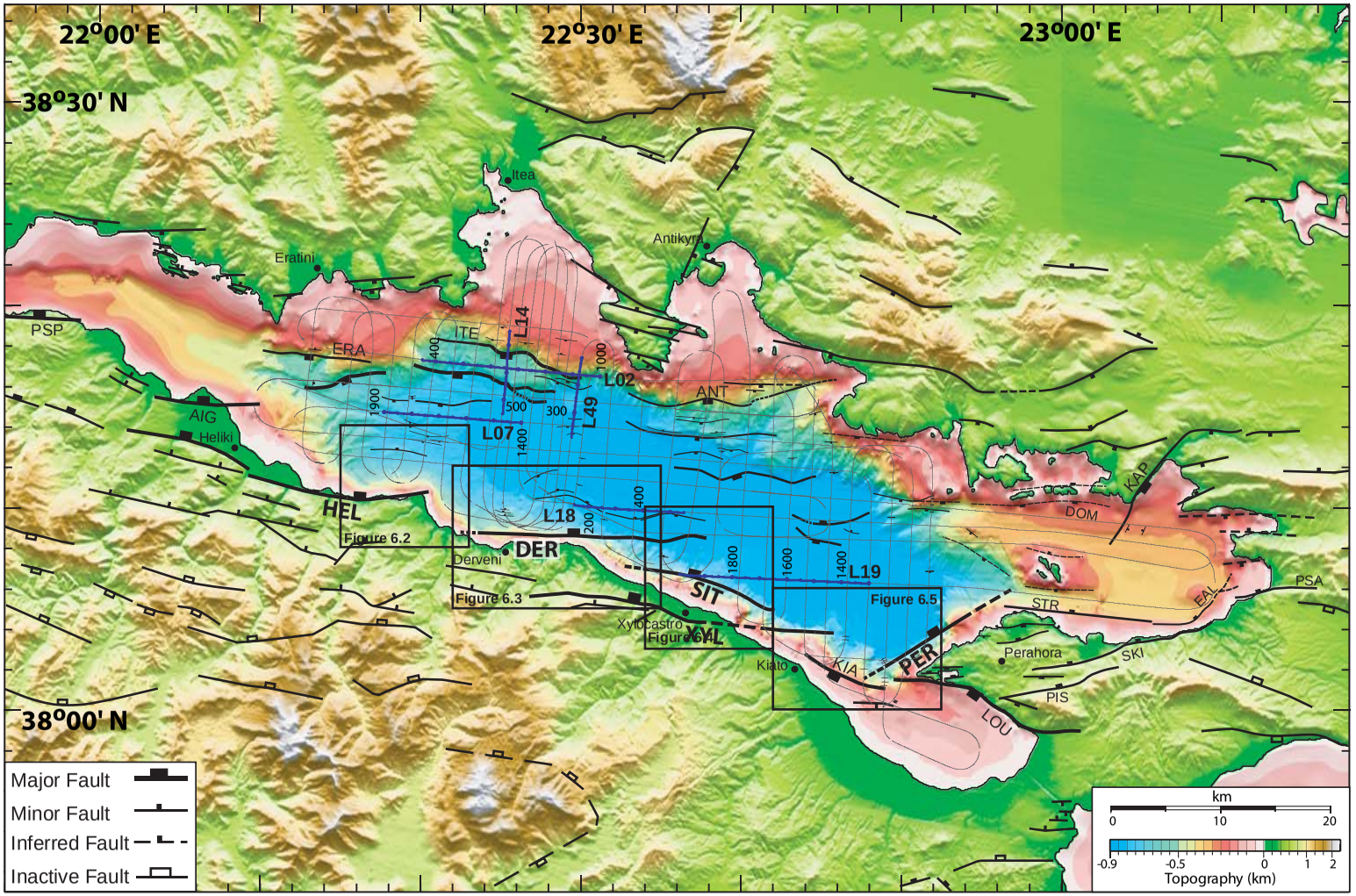
22°00' E
22°30' E
23°00' E
38°30' N
38°00' N
Itea
Antikyra
Eratini
PSP
ERA
ITE
L14
L02
L49
ANT
AIG
Heliki
L07
HEL
Figure 6.2
L18
DER
Dervéni
Figure 6.3
SIT
Xylocastro
Figure 6.4
YAL
L19
Figure 6.5
KAP
DOM
PSA
STR
EAL
Perahora
SKI
Kiato
KIA
PER
PIS
LOU
Major Fault
Minor Fault
Inferred Fault
Inactive Fault
km
0
10
20
-0.9
-0.5
0
1
2
Topography (km)

Figure 6.1

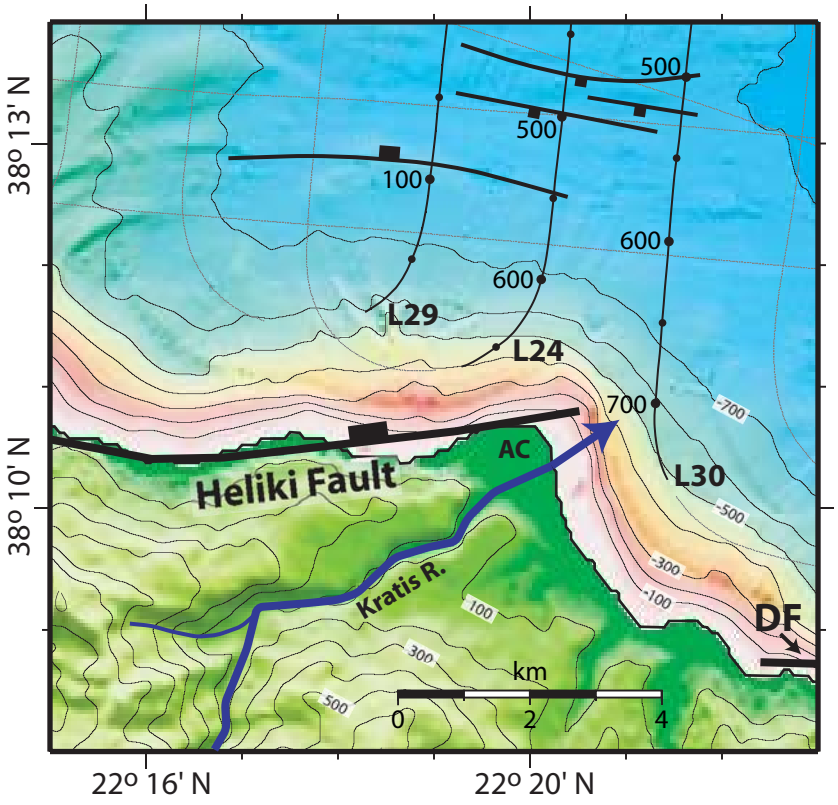
38º 13' N
38º 10' N
22º 16' N
22º 20' N
500
500
100
600
600
L29
L24
700
AC
Heliki Fault
L30
Kratis R.
DF
km
0
2
4

Figure 6.2A

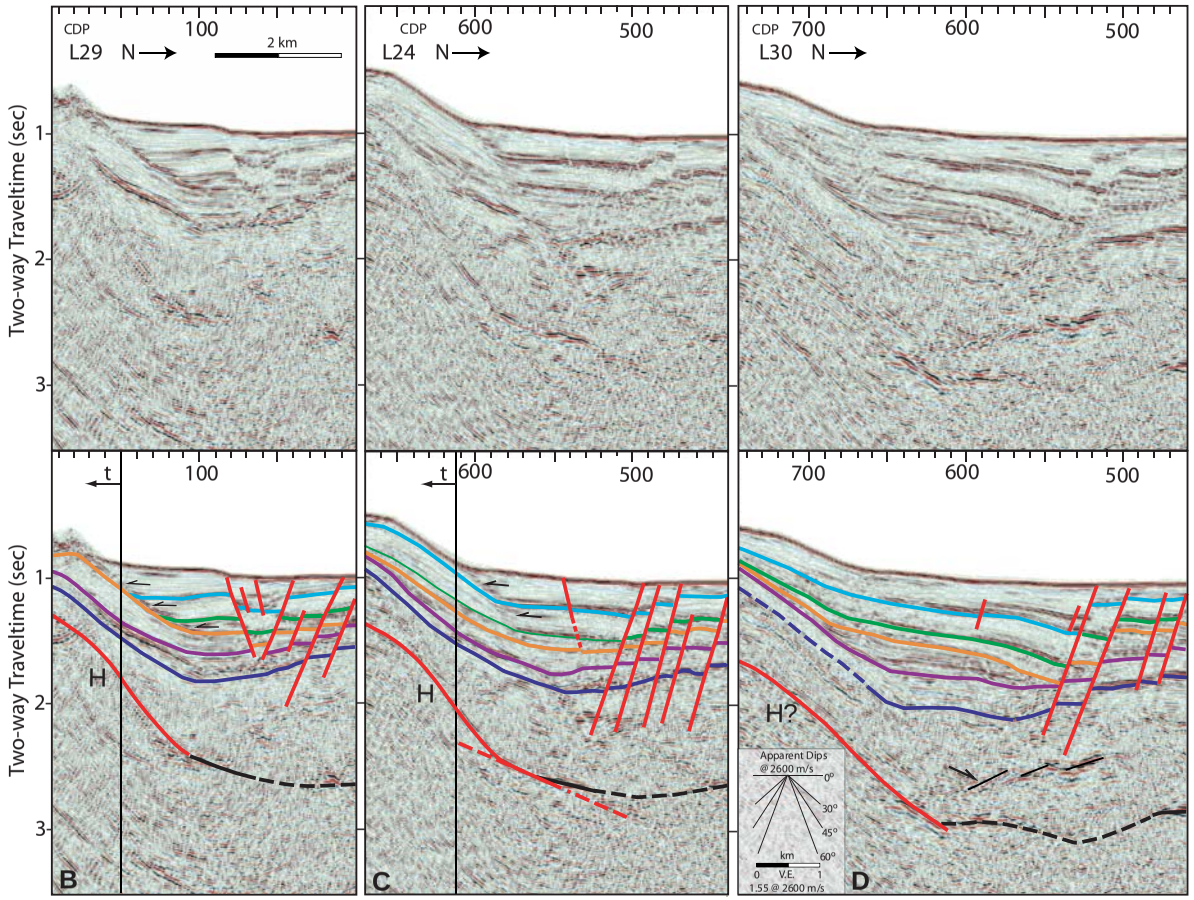

Figure 6.2BCD

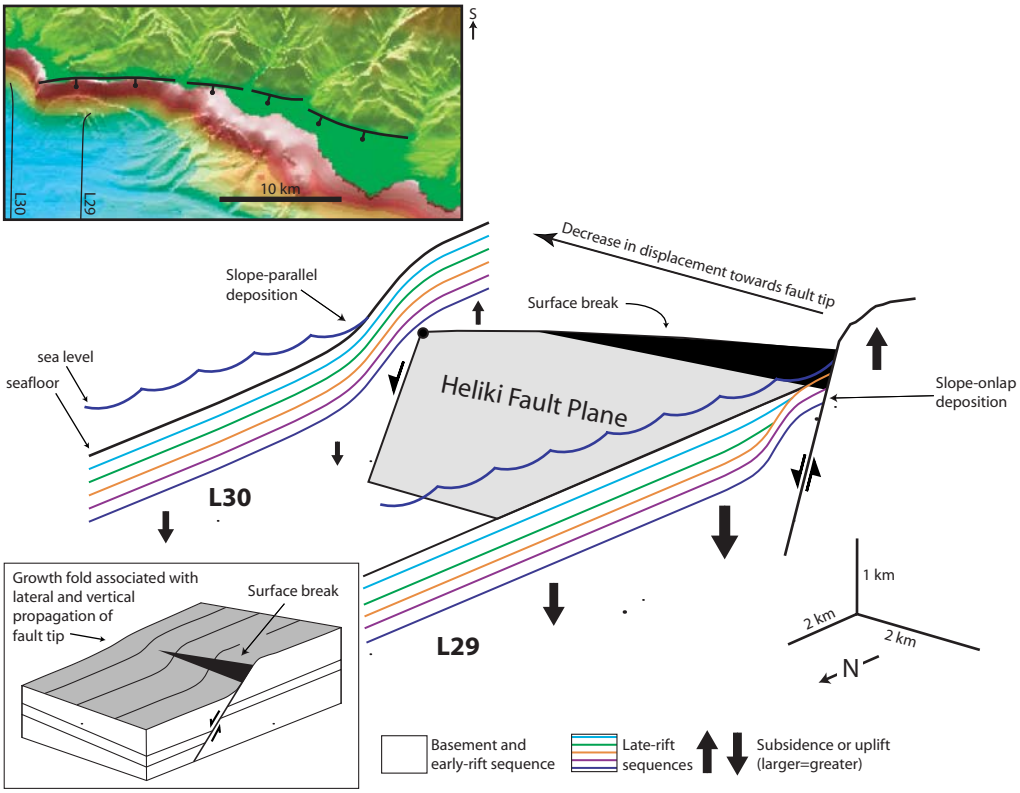
S
10 km
L30
L29
Decrease in displacement towards fault tip
Slope-parallel deposition
Surface break
sea level
seafloor
Heliki Fault Plane
Slope-onlap deposition
L30
L29
Growth fold associated with lateral and vertical propagation of fault tip
Surface break
1 km
2 km
2 km
N
Basement and early-rift sequence
Late-rift sequences
Subsidence or uplift (larger=greater)

Figure 6.2E

38o 10' N
38o 06' N
22o 25' E
22o 30' E
Derveni Fault
Xylocastro F.
L49
L33
SF
Derveniios R.
Skoupeliios R.
Fonissa R.
km
0
2
4
500
600
700
800
-850
-700
-500
-300
-100
100
300
500
1000

Figure 6.3A

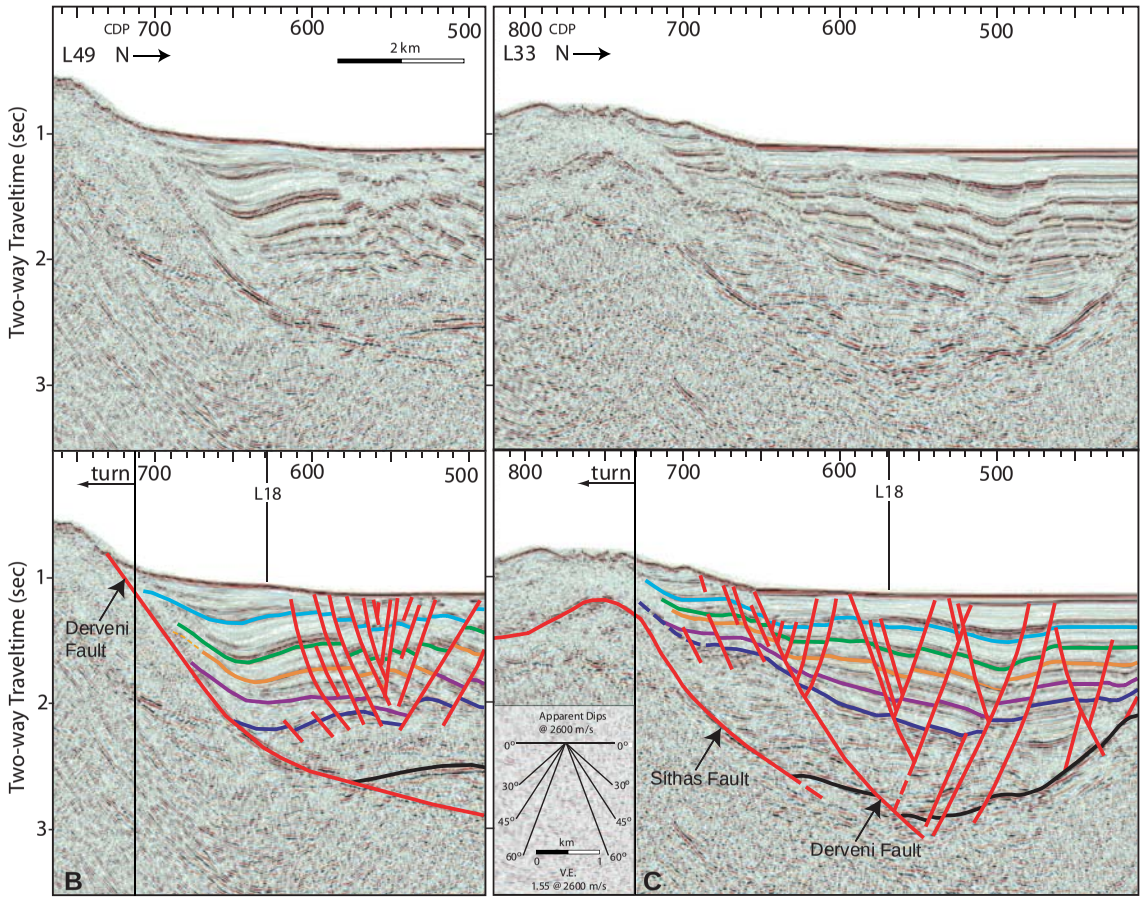
CDP 700
600
500
L49 N
2 km
800 CDP
700
600
500
L33 N
Two-way Traveltime (sec)
1
2
3
turn 700
600
500
L18
800
turn
700
600
500
L18
Derveni Fault
Apparent Dips @ 2600 m/s
0°
30°
45°
60°
km
V.E. 1.55 @ 2600 m/s
Sithas Fault
Derveni Fault
B
C

Figure 6.3BC

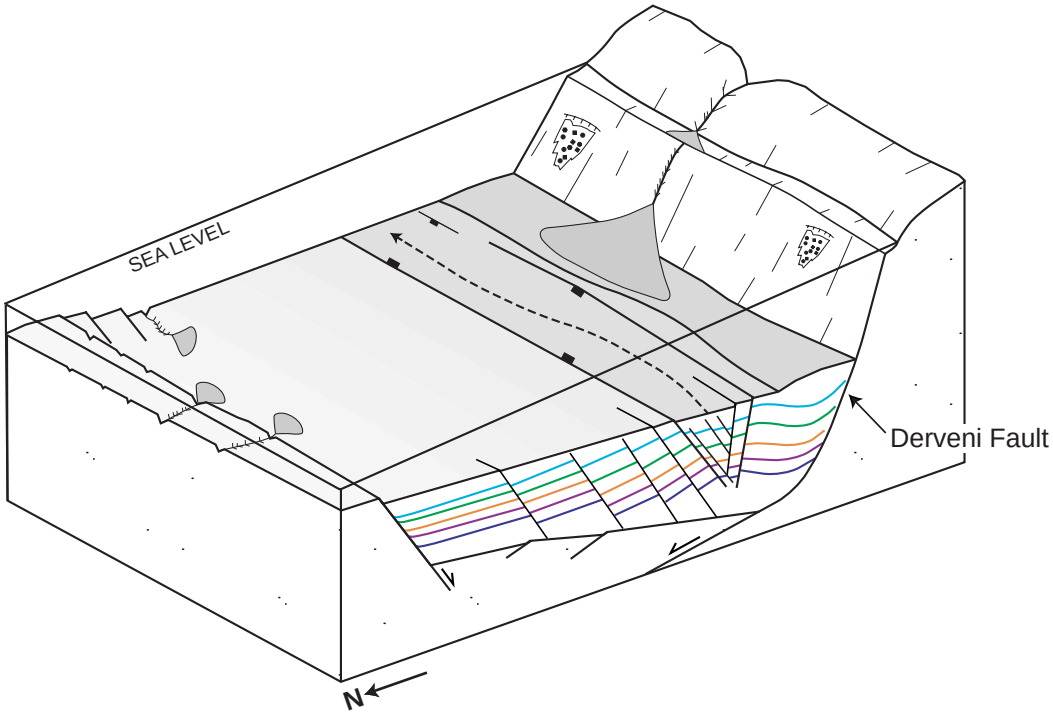

Figure 6.3D

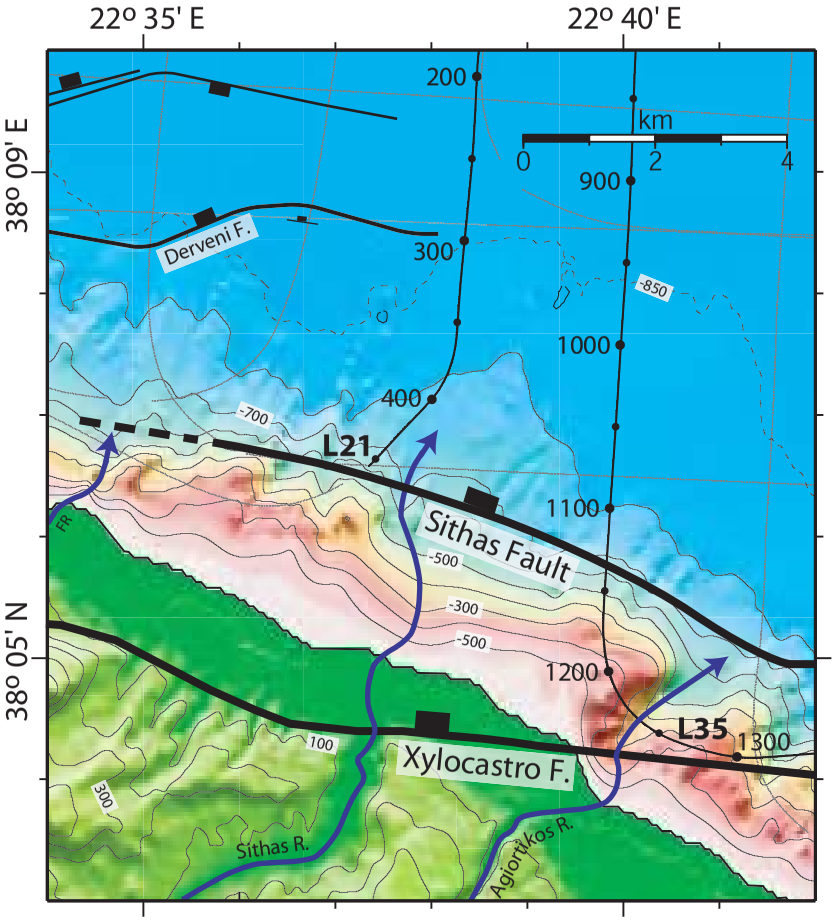
22º 35' E
22º 40' E
38º 09' E
38º 05' N
200
km
0
2
4
900
Derveni F.
300
-850
1000
400
-700
L21
1100
Sithas Fault
FR
-500
-300
-500
1200
L35
1300
100
Xylocastro F.
300
Sithas R.
Agiortikos R.

Figure 6.4A

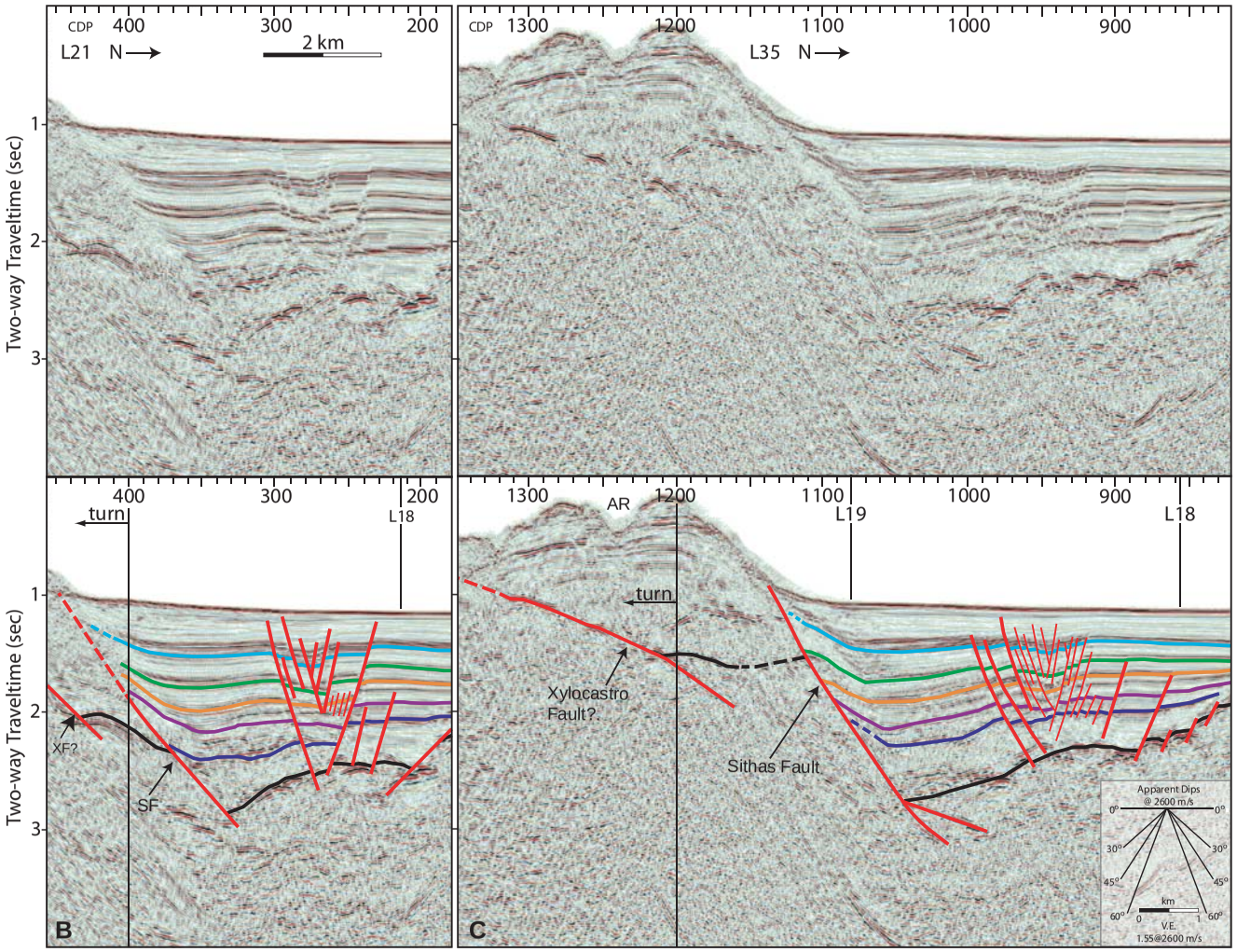
CDP 400 300 200
L21 N
2 km
CDP 1300 1200 1100 1000 900
L35 N
Two-way Traveltime (sec)
1
2
3
400 300 200
turn
L18
XF?
SF
B
1300 AR 1200 1100 1000 900
L19
L18
turn
Xylocastro Fault?
Sithas Fault
C
Apparent Dips @ 2600 m/s
0°
30°
45°
60°
km
0 1
V.E. 1.55@2600 m/s

Figure 6.4BC

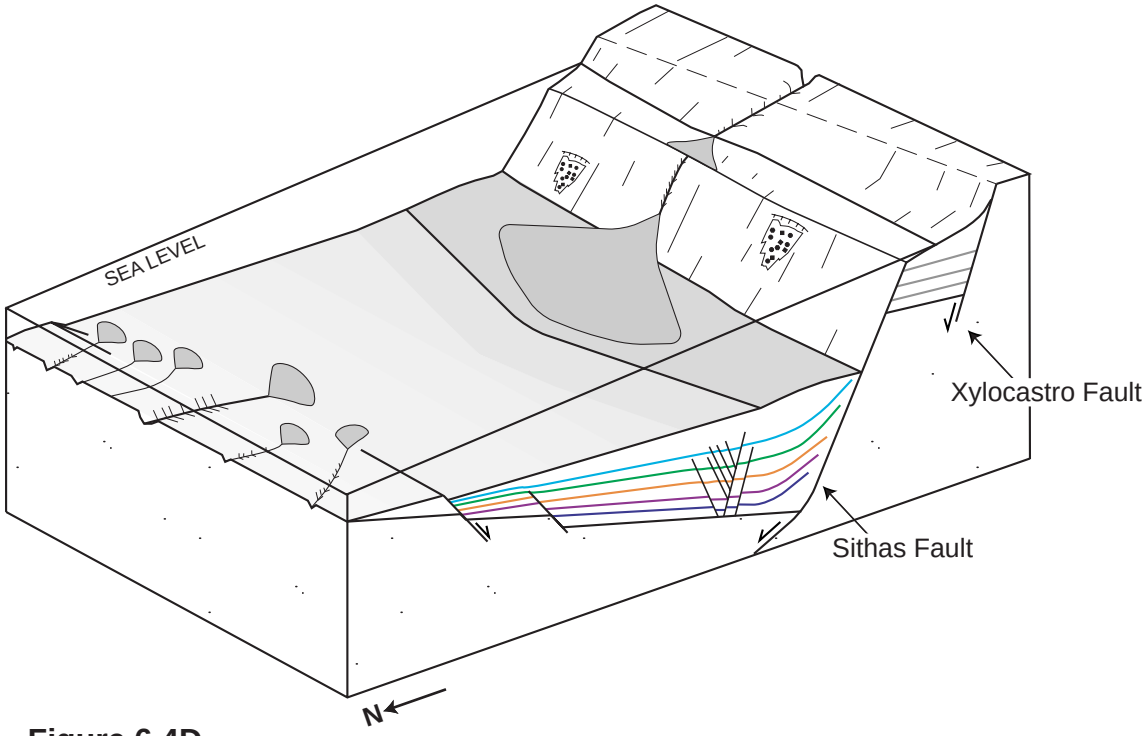

Figure 6.4D

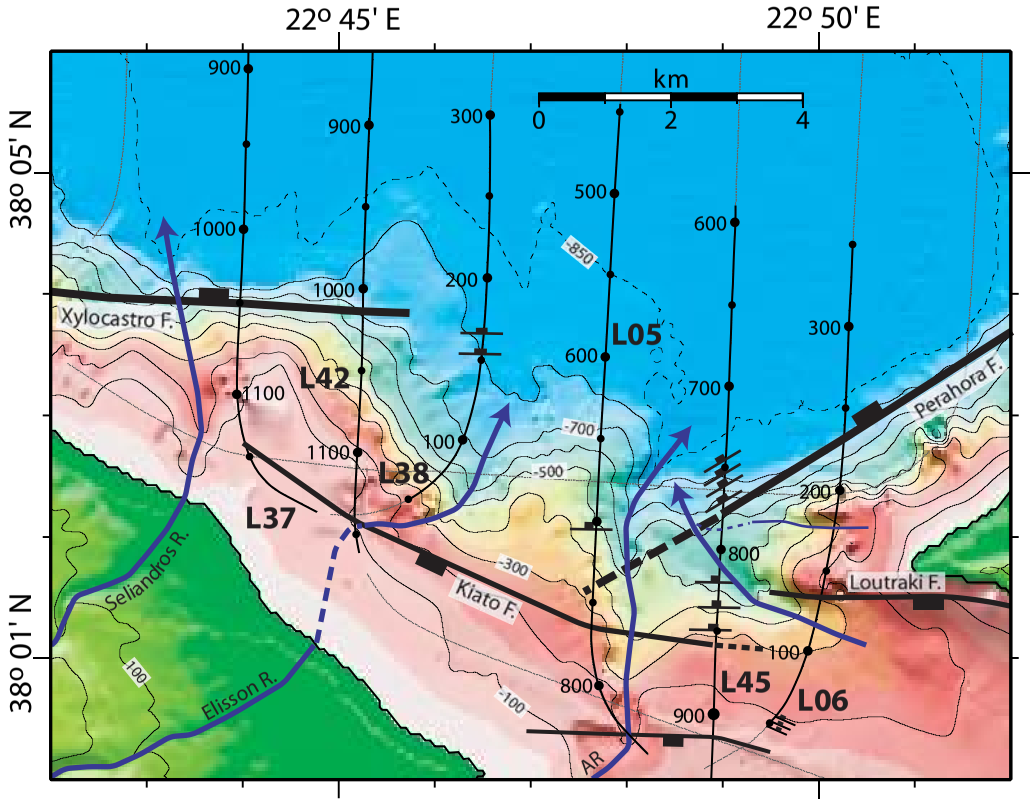
22º 45' E
22º 50' E
38º 05' N
38º 01' N
km
0
2
4
900
900
300
1000
500
600
-850
1000
200
Xylocastro F.
L05
600
300
L42
1100
700
Perahora F.
-700
1100
100
L38
-500
200
L37
800
-300
Kiato F.
Loutraki F.
Seliandros R.
100
100
Elisson R.
800
L45
L06
-100
900
AR

Figure 6.5A

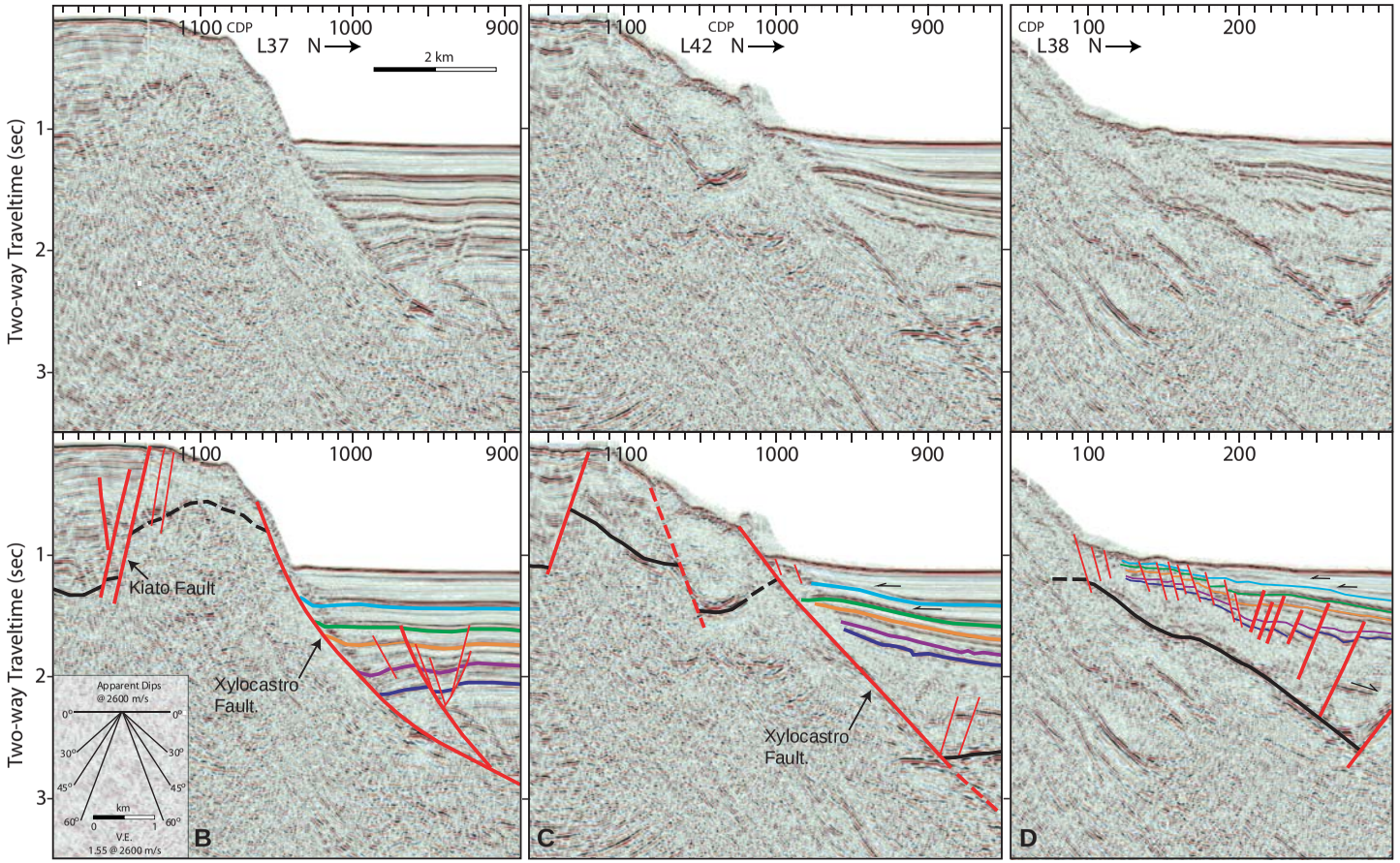
1100 CDP 1000 900
L37 N
2 km
CDP 1000 900
L42 N
CDP 100 200
L38 N
Two-way Traveltime (sec)
1
2
3
Kiato Fault
Xylocastro Fault
Apparent Dips @ 2600 m/s
0°
30°
45°
60°
km
V.E. 1.55 @ 2600 m/s
B
C
D

Figure 6.5B-D

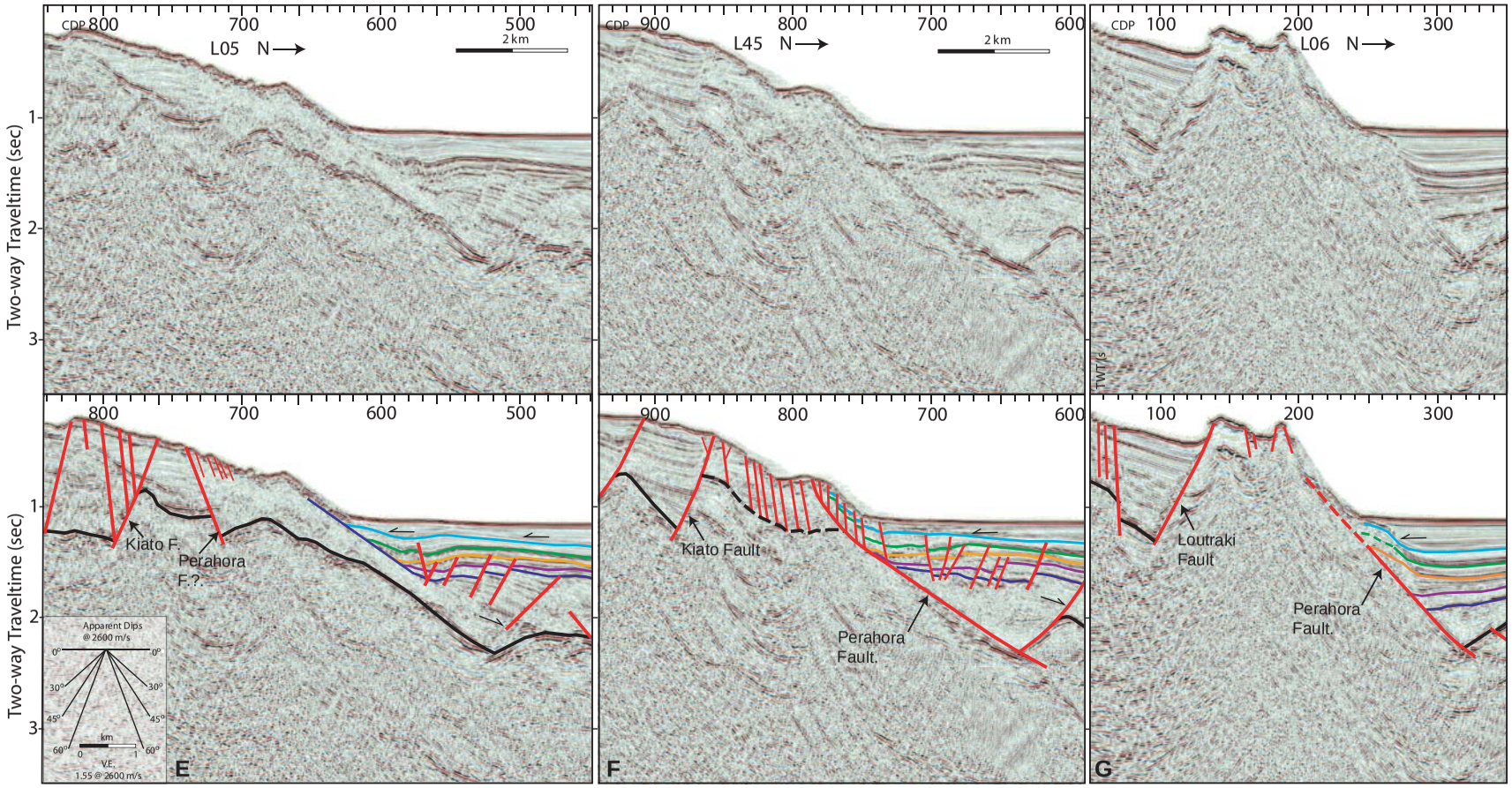

Figure 6.5EFG

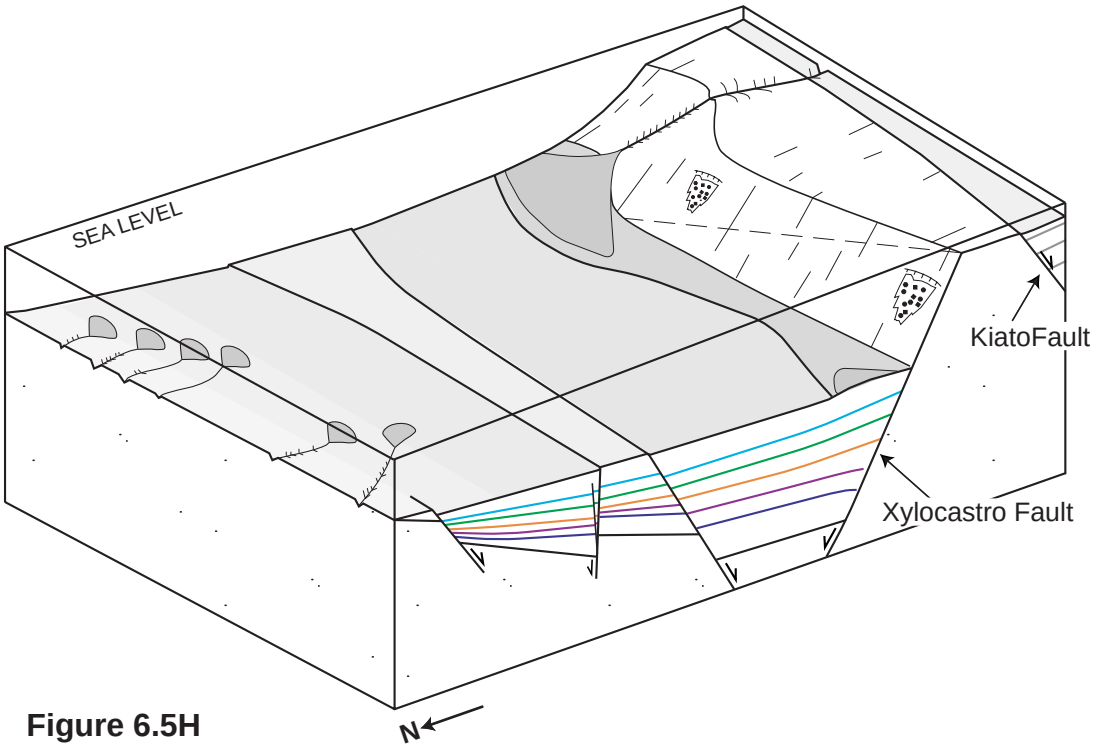

Figure 6.5H

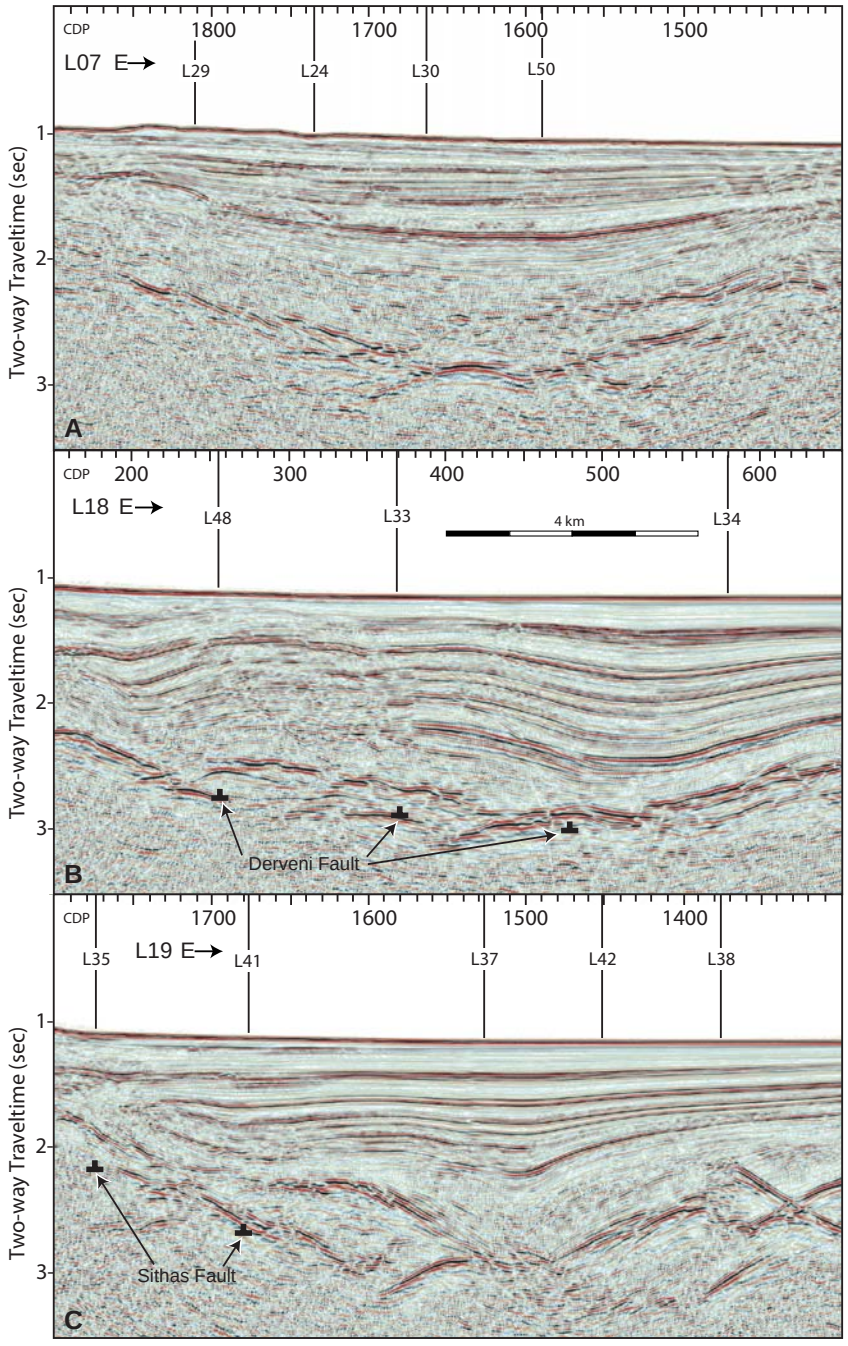
CDP
1800
1700
1600
1500
L07 E
L29
L24
L30
L50
Two-way Traveltime (sec)
1
2
3
A
CDP
200
300
400
500
600
L18 E
L48
L33
4 km
L34
Two-way Traveltime (sec)
Derveni Fault
B
CDP
1700
1600
1500
1400
L35
L19 E
L41
L37
L42
L38
Two-way Traveltime (sec)
Sithas Fault
C

Figure 6.6

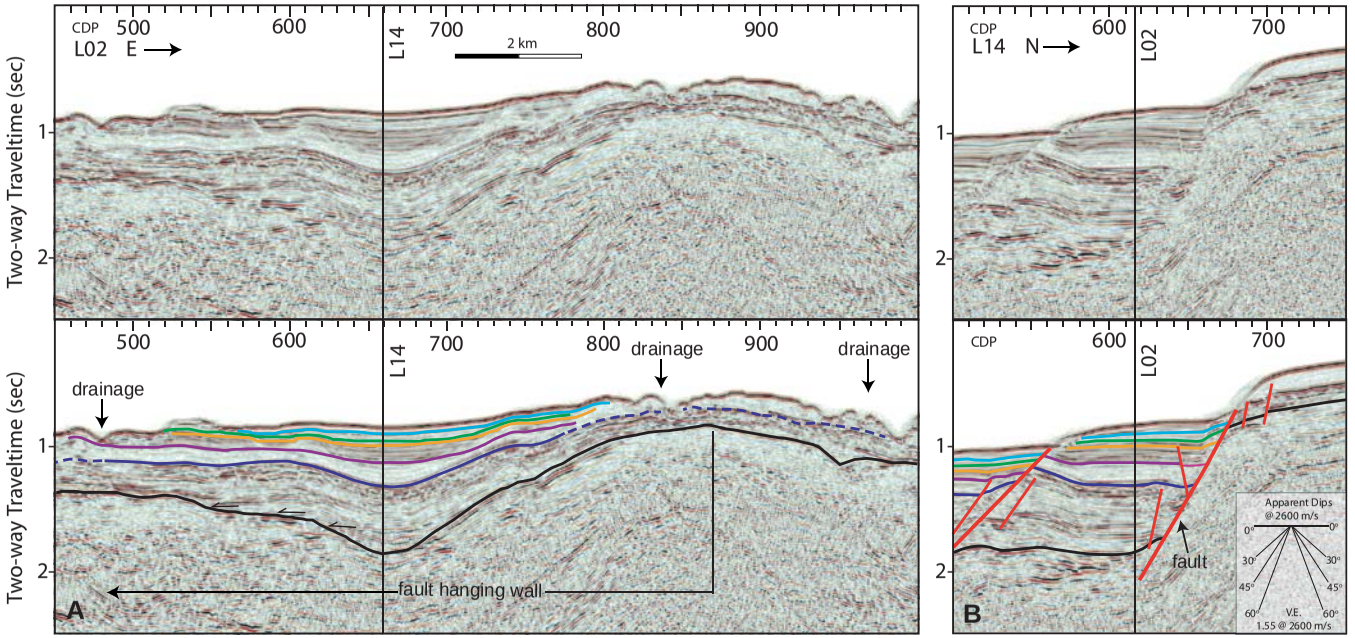
CDP
L02 E
500
600
L14
700
800
900
2 km
Two-way Traveltime (sec)
1
2
drainage
drainage
drainage
fault hanging wall
A
CDP
L14 N
600
700
L02
B
fault
Apparent Dips
@ 2600 m/s
0°
30°
45°
60°
V.E.
1.55 @ 2600 m/s

Figure 6.7

A1. Data Acquisition and Processing

The data presented in this study were collected during a geophysical survey aboard the R/V *Maurice Ewing* between the 23rd of July and the 1st of August, 2001(EW0108). Marine multi-channel seismic (MCS) reflection data, Hydro-Sweep DS-2 bathymetric data, and gravity data were acquired. The first two sets of data are the main focus of this study. The geophysical cruise, beginning at the Port of Patras on the western coast of Greece and ending at the Port of Piraeus near Athens, was the comprehensive MCS investigation of the Gulf of Corinth submarine basin (Figure A1.1).

Multi-Channel Seismic (MCS) Data

Prior offshore work in the area comprised soundings [*Heezen et al.*, 1966], high resolution (shallow) seismic reflection (air-gun) surveys [*Lykousis*, 1998; *Sakellariou et al.*, 1998], and MCS profiles that penetrate slightly >1 sec TWT beneath the seafloor and did not image basement [*Brooks and Ferentinos*, 1984; *Clement*, 2000; *Higgs*, 1988]. Clement [2000] pre-stack depth migrated two NS oriented MCS profiles shot for DEP-Hellenic Petroleum providing the first images into the basement. One EW profile [*Sachpazi et al.*, 2003] also imaged into the basement. Our grid of MCS data (Figure A1.1) consists of 33 NS trending strike lines and 10 EW trending dip lines, each of which images the entire sedimentary package and into the basement.

For the survey, a 20 air gun, 8445 cu. in. array was used as a seismic source with a shot interval of 50 m. For each shot, 16384 ms of data was recorded at a 4 ms sample rate for each channel on the streamer. During the first

half of the survey (lines 1-23) we shot to a 240 channel, 6-km-long streamer with a group interval of 25 m. The second half of the survey (lines 24-53) was shot using a 240 channel, 3-km-long streamer, with a group interval of 12.5 m. The change in streamer length midway through the survey was a precautionary response to traffic in the Gulf and occurred after the shooting of the longer E-W oriented lines. The streamer was instrumented with depth control birds (set to 10 m for this survey) with compasses that provided streamer depth and bearing. Navigation was recorded by GPS receivers on the tail-buoy and on the *Ewing.* The seismic data were written to tape and the EW0108 science party processed a limited number of lines through post-stack migration onboard using the seismic data processing software ProMAX.

All of the data were re-processed through post-stack migration and interpreted at the University of Hawaii using ProMAX and SeisWorks, both Landmark Graphics Corporation products. Following is a description of the steps used to create the MCS images presented in this paper. The steps had to be performed individually for each of the 53 seismic lines. Geographic coordinates were assigned to each shot using a crooked-line binning method similar to that used in on-land surveys where the streamer isn't directly behind the shot source. This was done to preserve as much data as possible around the many turns of the survey as important geologic information is contained in the basin edges offshore. After coordinates were assigned, shots were viewed and edited for bad shots and excessively noisy channels. The source of noise in our case was usually commercial traffic near the streamer or noise generated by the streamer

creating drag through the water column. In one instance, a group of noisy traces was produced by a strike-slip earthquake that occurred in the Aegean Sea, nearly 200 km to the northeast. The calculation of trace statistics such as spikiness facilitated the process of noise-editing the data. Refraction first arrivals were muted (but used by B. Zelt to perform first-arrival seismic tomography) because they travel through the water column and contain no reflection information. Predictive deconvolution was performed to compress the source wavelet [*Yilmaz*, 2001] by picking an operator and applying it to all the traces on a shot record. Parameters for the operator were chosen to best reduce the bubble pulse and other ringing in the data. A 4-10-70-80 Hz band pass filter was then applied to reduce the low- and high-frequency noise signals which are boosted after deconvolution [*Yilmaz*, 2001]. The data were then sorted into the common mid-point domain (CMP) using the crooked-line geometry of the streamer and a spacing of 25 meters between CMP's. Velocity analysis was performed on selected groups of CMP gathers grouped every 25 CMP's. The velocities were then spatially interpolated to create a velocity field used to apply normal-moveout (NMO) correction which attempts to flatten, by stretching, data with increased travel times at far offsets. Top mutes were applied to remove the excessively stretched data and inside mutes were applied to suppress the strong seafloor multiples. In the center of the basin the mutes were picked every 25 CDP's but more frequently in regions of topography to avoid cutting out portions of the seafloor. Each line was stacked and treated with a time-varying band pass filter to further suppress the seafloor multiple which persisted and obscured the

deep sediments in the form of high-frequency “fuzz”. The first filter gate was picked from the seafloor to ~50 ms above the multiple and had a value of 0-4-70-80 Hz and the second filter gate was picked from the multiple to 16000 ms and had a value of 4-10-30-40 Hz. Once satisfied with the stack, an interval velocity field was created for each seismic section and converted to root mean square (RMS) velocities for migration. Memory Stolt F-K migration was performed using the RMS velocities to move dipping events to their “true” subsurface positions and to collapse diffractions [*Yilmaz*, 2001]. Numerous iterations were performed in an attempt to reach the most satisfactory velocity model. The migrated sections were then loaded into SeisWorks for interpretation.

Hydrosweep-DS2 Bathymetry and Digital Topography

Multibeam bathymetric data were collected using Hydrosweep DS-2 multibeam sonar during the entire cruise, including after cessation of MCS shooting. The multibeam system calculates as many as 140 “soft” beams from the 59 “hard” beams generated by the ATLAS GE-6012 hardware signal processor and results in a swath width as great as 120 degrees in deep water. Depths in the Gulf ranging from 13 mbsl to nearly 887 mbsl resulted in narrow swaths in the shallow areas and wide swaths in the deep areas. Processing of the bathymetric data was performed using MB System software [*Caress and Chayes*, 1996]. Four XBT’s (salinity, depth, and temperature measurement devices) launched during the survey provided sound-velocity information in various parts of the Gulf (Figure A1.2) which was applied to the data to best reduce residuals stemming from inaccurate profiles acquired from a global

database of sound-velocity profiles. Manual editing of each ping was carried out to eliminate obvious artifacts and the data was gridded with a cell size of 0.0005 degrees (~55 meters) resulting in the map shown in Figure A1.3. To fill gaps in shallow portions of the Gulf, points were digitized from offshore maps that combined data collected by British and Greek surveys between 1840 and 1935. The resulting bathymetry was then combined with a digital elevation model (DEM) of Greece to create a final map using the Generic Mapping Tools (GMT) [*Wessel and Smith*, 1998]. The combined bathymetric and topographic data were then used to make all of the maps for the rest of this thesis.

Depth-Converted (MCS) Data

Select MCS lines from the EW0108 dataset underwent post-migration depth conversion in ProMAX to better constrain fault dip and sediment thickness information. Figure A1.4 shows the velocity model used to convert the MCS data superposed atop one of the MCS profiles and a comparison of velocity gradients from the seafloor to 2 km depth calculated using a variety of methods.

I specify linear velocity gradients for the water column, sediment section, and basement and use the seafloor and top of basement horizons from my SeisWorks interpretations to create a velocity space for each depth-converted MCS profile (Figure A1.4B). The water column velocity is 1.5 km/sec and I increased the velocity in the sediment section linearly by 1.5 km/sec/sec from 1.5 km/sec at the water-sediment interface to the top of the basement. The sediment thickness in the Gulf, and hence the maximum sediment velocity, is highly

variable. In the basement, the velocity increases linearly from 5 km/sec at the top of the basement by 0.25 km/sec/sec.

Although simple, the linear velocity gradient I use to convert the MCS data to depth compare well with velocity models obtained by other methods. Figure A1.4B includes various velocity models from the seafloor to 2 km in the Gulf. The models include results from a streamer tomography study [*Zelt et al.*, 2004], a profile obtained by pre-stack depth conversion methods [*Clement*, 2000; *Sachpazi et al.*, 2003], the linear velocity profile, and an exponentially increasing velocity profile. The linear profile approximates the velocity models obtained via other methods fairly well.

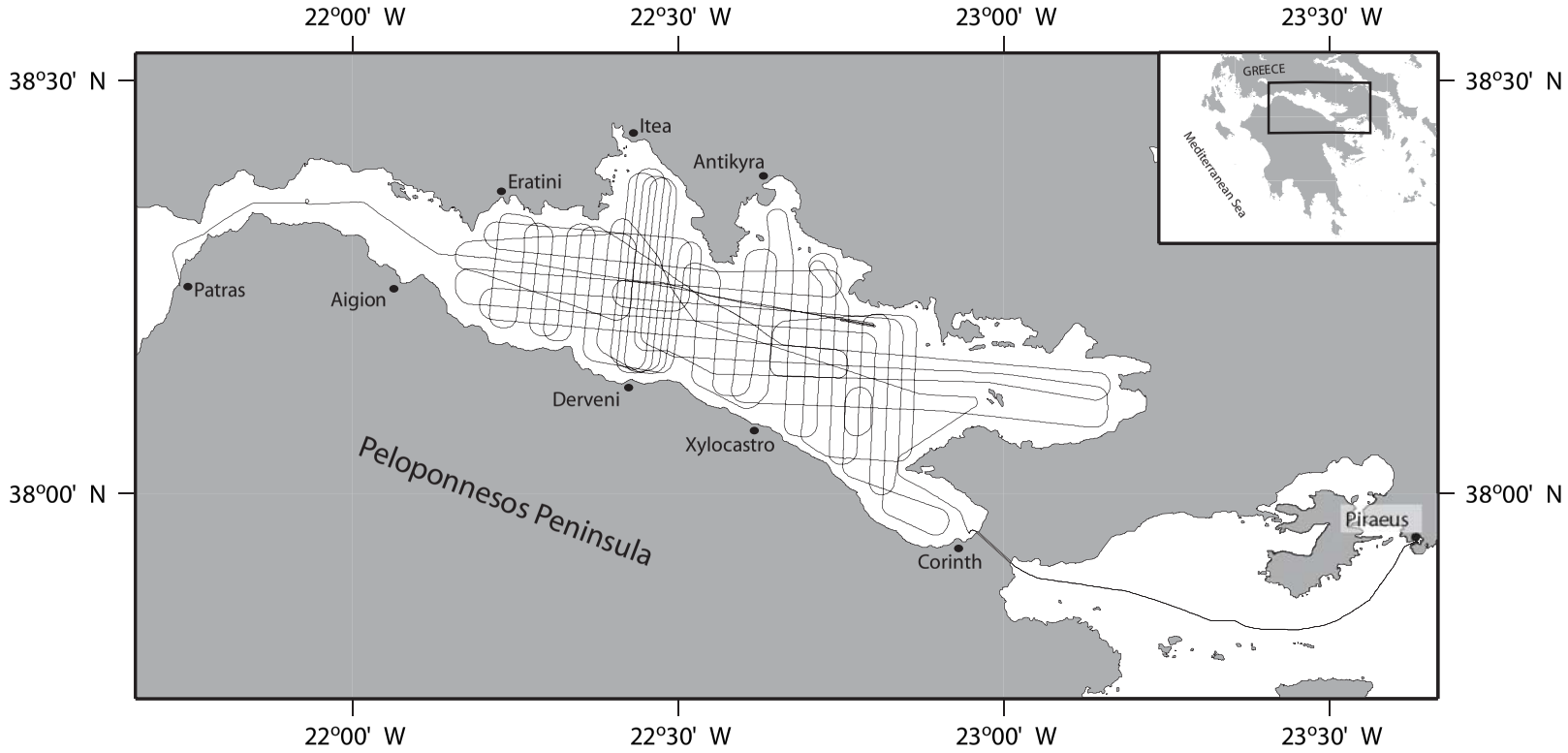
22°00' W
22°30' W
23°00' W
23°30' W
38°30' N
38°00' N
Itea
Antikyra
Eratini
Patras
Aigion
Derveni
Xylocastro
Peloponnesos Peninsula
Corinth
Piraeus
GREECE
Mediterranean Sea

Figure A1.1

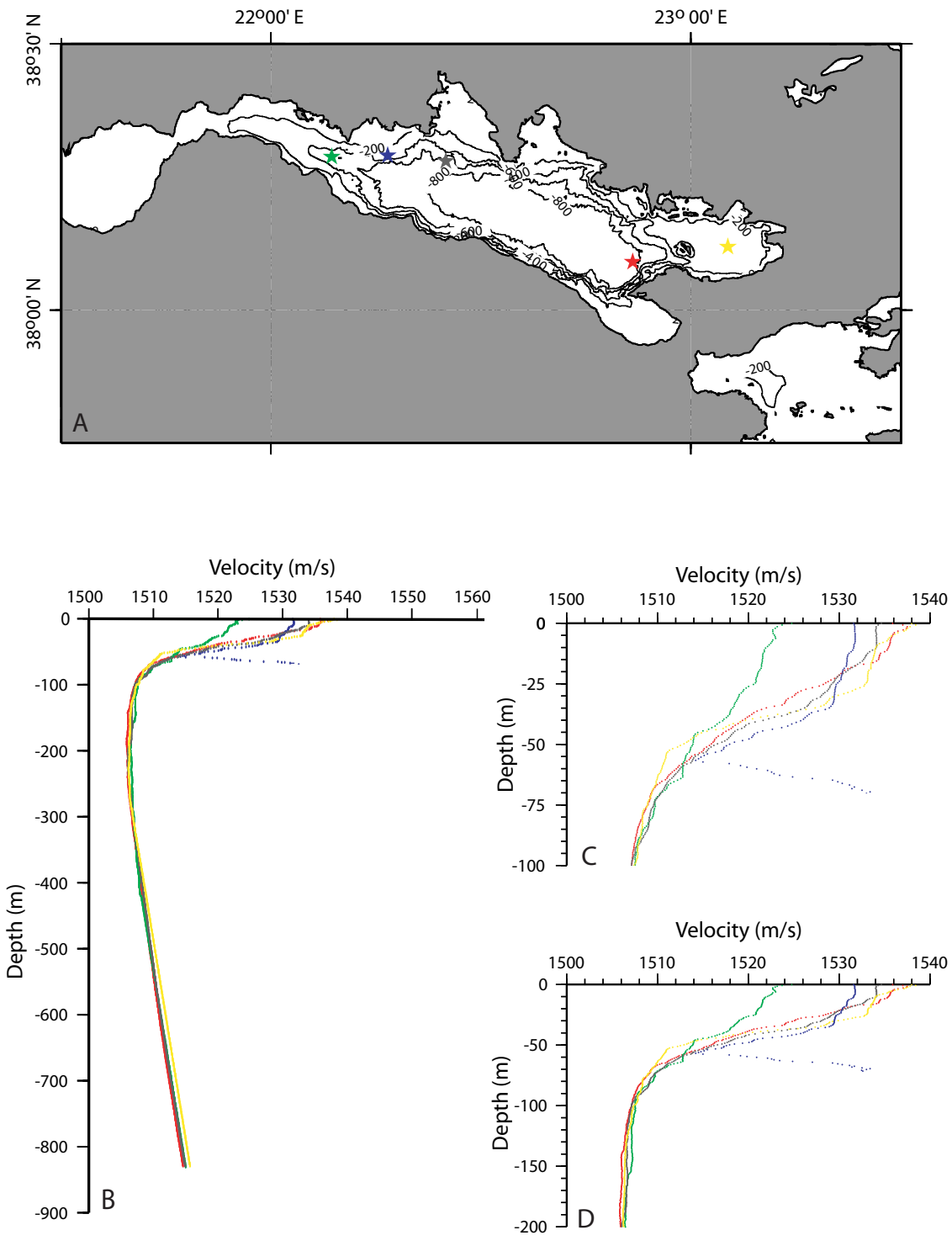
22°00' E
23° 00' E
38°30' N
38°00' N
-200
-400
-600
-800
A
Velocity (m/s)
1500 1510 1520 1530 1540 1550 1560
Depth (m)
0 -100 -200 -300 -400 -500 -600 -700 -800 -900
B
Velocity (m/s)
1500 1510 1520 1530 1540
Depth (m)
0 -25 -50 -75 -100
C
Velocity (m/s)
1500 1510 1520 1530 1540
Depth (m)
0 -50 -100 -150 -200
D

Figure A1.2

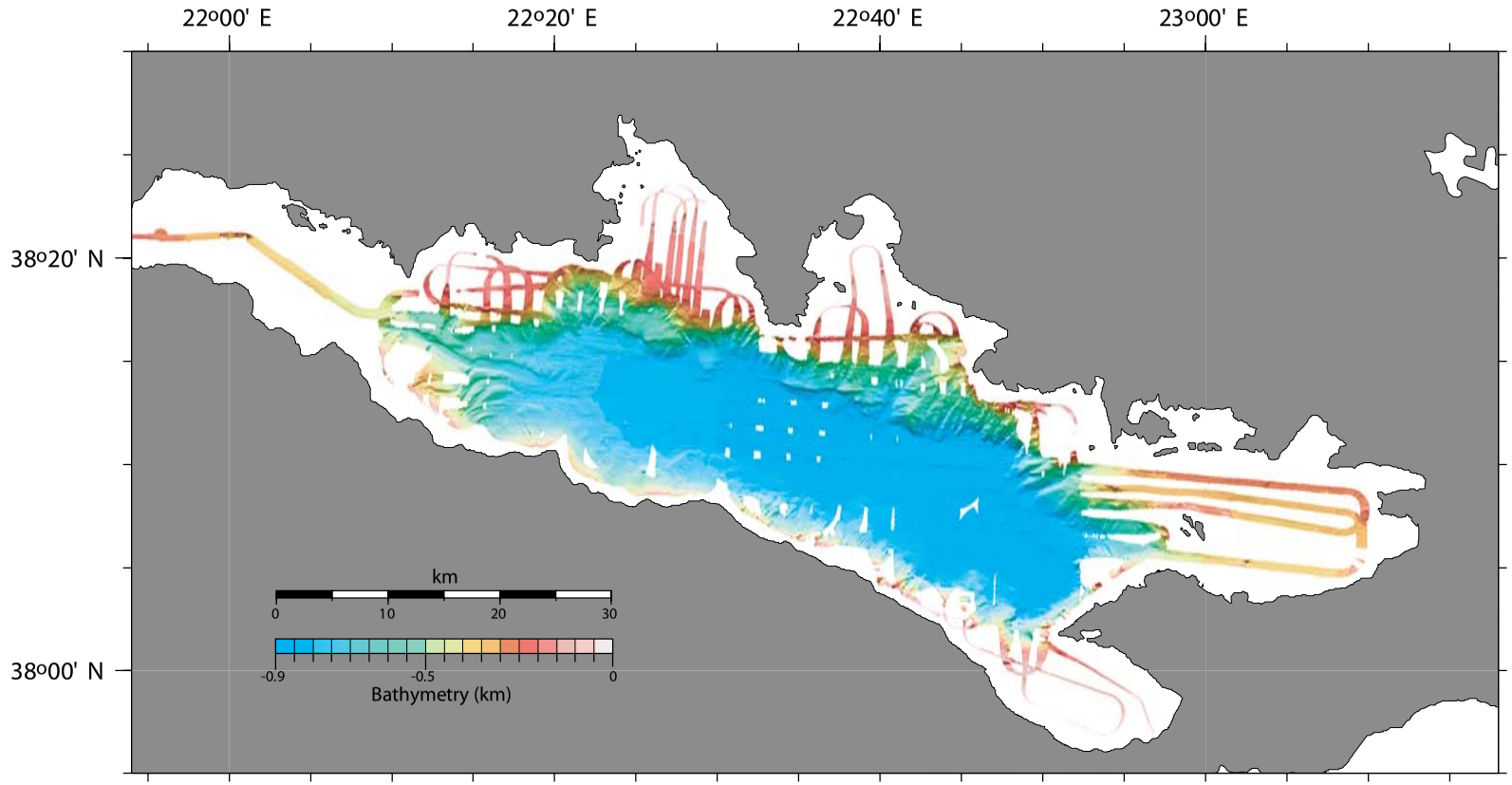
22°00' E
22°20' E
22°40' E
23°00' E
38°20' N
38°00' N
km
0
10
20
30
-0.9
-0.5
0
Bathymetry (km)

Figure A1.3

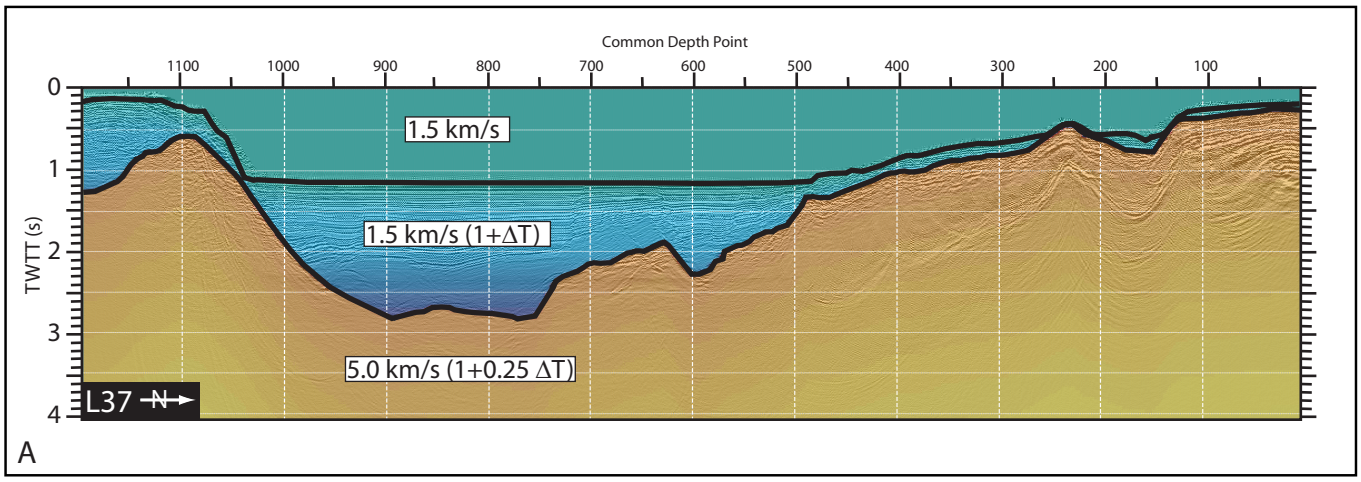
Common Depth Point
1100
1000
900
800
700
600
500
400
300
200
100
0
1
2
3
4
TWTT (s)
1.5 km/s
1.5 km/s (1+ΔT)
5.0 km/s (1+0.25 ΔT)
L37
N
A

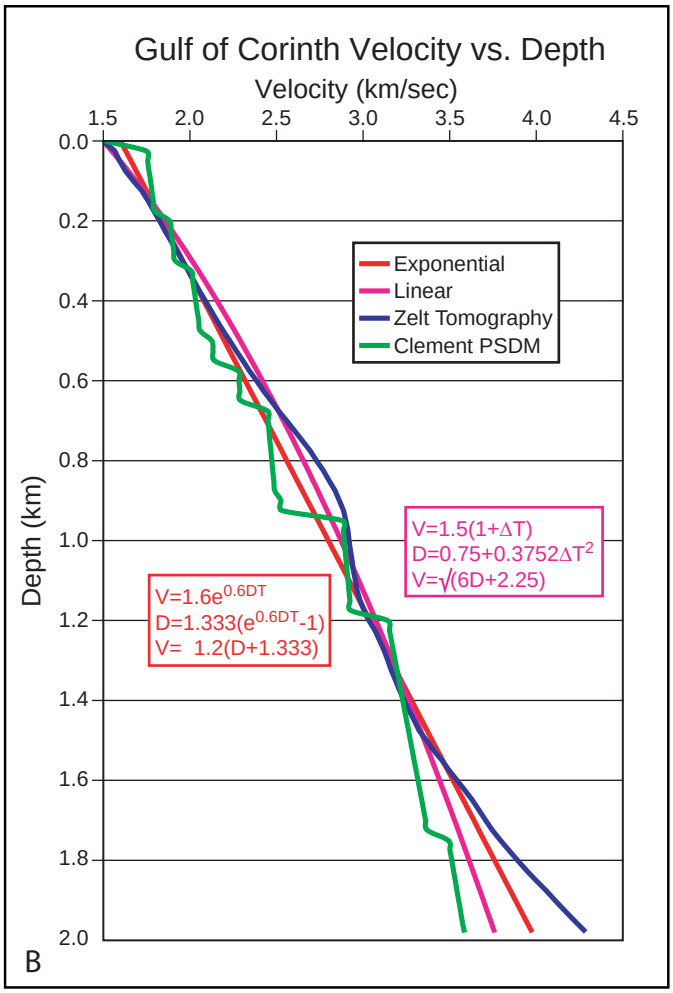
Gulf of Corinth Velocity vs. Depth
Velocity (km/sec)
1.5
2.0
2.5
3.0
3.5
4.0
4.5
0.0
0.2
0.4
0.6
0.8
1.0
1.2
1.4
1.6
1.8
2.0
Depth (km)
Exponential
Linear
Zelt Tomography
Clement PSDM
V=1.5(1+ΔT)
D=0.75+0.3752ΔT2
V=√(6D+2.25)
V=1.6e0.6DT
D=1.333(e0.6DT-1)
V= 1.2(D+1.333)
B

Figure A1.4

FIGURE CAPTIONS

Figure A1.1 Location map showing the R/V Maurice Ewing survey track in the Gulf of Corinth between July 21st and August 1st, 2001. Major cities are shown and include the port of Patras, where the cruise began, and the port of Piraeus, where the cruise finished. Inset map of Greece shows the location of the Gulf of Corinth.

Figure A1.2 A) XBT positions (starred) and (B-D) water velocity profiles used to edit the Hydrosweep bathymetric data. Increase in velocity at ~50 mbsl on the blue profile may be due to groundwater recharge along a fault plane.

Figure A1.3 Manually edited, processed, and illuminated (from the north) Hydrosweep-DS2 bathymetry collected aboard the R/V Maurice Ewing in the Gulf of Corinth. Swath width varies as a function of depth and is narrowest in the shallow subsidiary gulfs and near the steep southern margin. A few track-parallel artifacts still persist and can be seen in the central-eastern portion of the basin. Note the sparse data coverage close to the shorelines, in the subsidiary gulfs, and in the narrow, western arm of the Gulf.

Figure A1.4 A) Velocity-TWT model used to depth convert MCS profiles. B) Comparison of velocity models for the Gulf obtained by various methods.

REFERENCES

Abers, G.A., Evidence for seismogenic normal faults at shallow dips in continental rifts, in *Non-volcanic rifting of continental margins: a comparison of evidence from land and sea*, edited by R.C.L. Wilson, R.B. Whitmarsh, B. Taylor, and N. Froitzheim, Geol. Soc. London. Spec. Publ., 2001.

Armijo, R., B. Meyer, G.C.P. King, A. Rigo, and D. Papanastassiou, Quaternary evolution of the Corinth Rift and its implications for the Late Cenozoic evolution of the Aegean, *Geophysical Journal International*, *126*, 11-53, 1996.

Avallone, A., P. Briole, A.M. Agatza-Balodimou, H. Billiris, O. Charade, C. Mitsakaki, A. Nercessian, K. Papazissi, D. Paradissis, and G. Veis, Analysis of eleven years of deformation measured by GPS in the Corinth Rift Laboratory area, *Comptes Rendus Geosciences*, *336*, 301-311, 2004.

Baker, C.D., D. Hatzfeld, H. Lyon-Caen, E. Papadimitriou, and A. Rigo, Earthquake mechanisms of the Adriatic sea and western Greece, *Geophy. Jour. Int.*, *131*, 559-594, 1997.

Bernard, P., P. Briole, B. Meyer, H. Lyon-Caen, J.M. Gomez, C. Tiberi, C. Berge, R. Cattin, D. Hatzfeld, C. Lachet, B. Lebrun, A. Deschamps, F. Courboulex, C. Larroque, A. Rigo, D. Massonnet, P. Papadimitriou, J. Kassaras, D. Diagoutas, K. Makropoulos, G. Veis, E. Papazizi, C. Mitsakaki, V. Karakostas, E. Papadimitriou, D. Papanastassiou, G. Chouliaras, and G. Stavrakakis, The Ms=6.2, June 15, 1995 Aigion earthquake (Greece): evidence for low angle normal faulting in the Corinth rift, *Journal of Seismology*, *1*, 131-150, 1997.

Billiris, H., D. Paradissis, G. Veis, P. England, W. Featherstone, B. Parsons, P. Cross, P. Rands, M. Rayson, P. Sellers, V. Ashkenazi, M. Davison, J. Jackson, and N. Ambraseys, Geodetic determination of tectonic deformation in central Greece from 1900 to 1988, *Nature*, *350*, 124-129, 1991.

Brace, K.L., Preliminary ocean-area geoid from GEOS-III radar altimetry, Defense Mapping Agency, St. Louis, Mo, 1977.

Briole, P., A. Rigo, H. Lyon-Caen, J.C. Ruegg, K. Papazissi, C. Mitsakaki, A. Balodimou, G. Veis, D. Hatzfeld, and A. Deschamps, Actice deformation of the Corinth rift, Grece: Results from repeated Global Positioning System surveys between 1990 and 1995, *Journal of Geophysical Research*, *105* (B11), 25,605-25,625, 2000.

Brooks, M., and G. Ferentinos, Tectonics and sedimentation in the Gulf of Corinth and the Zakynthos and Kefallinia channels, western Greece, *Tectonophyiscs*, *101*, 25-54, 1984.

Caress, D.W., and D.N. Chayes, Improved processing of Hydrosweep DS multibeam data on the R/V Maurice Ewing, *Marine Geophysical Researches*, *18*, 631-650, 1996.

Clarke, P.J., R.R. Davies, P.C. England, B.E. Parsons, H. Billiris, D. Paradissis, G. Veis, P.H. Denys, P.A. Cross, V. Ashkenazi, and R. Bingley, Geodetic estimate of seismic hazard in the Gulf of Korinthos, *Geophysical Research Letters*, *24* (11), 1303-1306, 1997.

Clement, C., Imagerie sismique crustale de la subduction Hellenique et du Golfe de Corinth, PhD thesis, University Paris VI, Paris, 2000.

Collier, R.E.L., Eustatic and tectonic controls upon Quaternary coastal sedimentation in the Corinth Basin, Greece, *Jour. Geol. Soc. Lond.*, *147*, 301-314, 1990.

Collier, R.E.L., M.R. Leeder, P.J. Rowe, and T.C. Atkinson, Rates of tectonic uplift in the Corinth and Megara Basins, central Greece, *Tectonics*, *11*, 1159-1167, 1992.

Doutsos, T., and D.J.W. Piper, Listric faulting, sedimentation, and morphological evolution of the Quaternary eastern Corinth rift, Greece: First stages of continental rifting, *Geological Society of America Bulletin*, *102*, 812-829, 1990.

Doutsos, T., and G. Poulimenos, Geometry and kinematics of active faults and their seismotectonic significance in the western Corinth-Patras rift (Greece), *Journal of Structural Geology*, *14* (6), 689-699, 1992.

Ferentinos, G., G. Papatheodorou, and M.B. Collins, Sediment transport processes on an active submarine fault escarpment: Gulf of Corinth, Greece, *Marine Geology*, *83*, 43-61, 1988.

Flotte, N., V. Plangnes, D. Sorel, and A. Benedicto, Attempt to date Pleistocene normal faults of the Corinth-Patras Rift (Greece) by U/Th method, and tectonic implications, *Geophysical Research Letters*, *28* (19), 3769-3772, 2001.

Forsyth, D.W., Finite extension and low angle normal faulting, *Geology*, *20*, 27-30, 1992.

Gawthorpe, R.L., A.J. Fraser, and R.E.L. Collier, Sequence stratigraphy in active extensional basins: implications for the interpretation of ancient basin-fills, *Marine and Petroleum Geolgy*, *11* (6), 642-658, 1994.

Gawthorpe, R.L., and S. Hardy, Extensional fault-propogation folding and base-level change as controls on growth-strata geometries, *Sedimentary Geology*, *146*, 47-56, 2002.

Gawthorpe, R.L., and M.R. Leeder, Tectono-sedimentary evolution of active extensional basins, *Basin Research*, *12*, 195-218, 2000.

Gawthorpe, R.L., I. Sharp, J.R. Underhill, and S.C. Gupta, Linked sequence stratigraphic and structural evolution of propagating normal faults, *Geology*, *25* (9), 795-798, 1997.

Ghisetti, F., and L. Vezzani, Fault segmentation in the Gulf of Corinth (Greece) constrained by patterns of Pleistocene sedimentation, *Comptes Rendus Geosciences*, *336*, 243-249, 2004.

Gibbs, A.D., Structural evolution of extensional basin margins, *Jour. Geol. Soc. Lond.*, *141*, 609-620, 1984.

Graseman, B., S. Martel, and C.W. Passcheir, Reverse and normal drag along a single dip-slip fault, in preparation.

Hatzfeld, D., et al., The Galaxidi Earthquake of 18 November 1992: A Possible Asperity within the Normal Fault System of the Gulf of Corinth (Greece), *Bulletin of the Seismological Society of America*, *86* (6), 1987-1991, 1996.

Hatzfeld, D., V. Karakostas, M. Ziazia, I. Kassaras, E. Papadimitriou, K. Makropoulos, N. Voulgaris, and C. Papaioannou, Microseismicity and faulting geometry in the Gulf of Corinth (Greece), *Geophysical Journal International*, *141*, 438-456, 2000.

Heezen, B.C., M. Ewing, and G.L. Johnson, The Gulf of Corinth floor, *Deep-Sea Research*, *13*, 381-411, 1966.

Higgs, B., Syn-sedimentary structural controls on basin deformation in the Gulf of Corinth, Greece, *Basin Research*, *1*, 155-165, 1988.

Hubert, A., G. King, R. Armijo, B. Meyer, and D. Papanastasiou, Fault re-activation, stress interaction and rupture propogation of the 1981 Corinth earthquake sequence, *Earth and Planetary Science Letters*, *142*, 573-585, 1996.

Jackson, J.A., J. Gagnepain, G. Houseman, G.C.P. King, P. Papadimitriou, C. Soufleris, and J. Virieux, Seismicity, normal faulting, and the geomorphological development of the Gulf of Corinth (Greece): the

Corinth earthquakes of February and March 1981, *Earth and Planetary Science Letters*, *57*, 377-397, 1982.

Jolivet, L., A comparison of geodetic and finite strain pattern in the Aegean, geodynamic implications, *Earth and Planetary Science Letters*, *187*, 95-104, 2001.

Jolivet, L., and C. Faccenna, Mediterranean extension and the Africa-Eurasia collision, *Tectonics*, *19* (6), 1095-1106, 2000.

Keraudren, B., and B. Sorel, The terraces of Corinth (Greece)-A detailed record of eustatic sea level variations during the last 500,000 years, *Marine Geology*, *77*, 99-107, 1987.

Khalil, S.M., and K.R. McClay, Extensional fault-related folding, northwestern Red Sea, Egypt, *Journal of Structural Geology*, *24* (4), 743-762, 2002.

King, G.C.P., Z.X. Ouyang, P. Papadimitriou, A. Deschamps, J. Gagnepain, G. Houseman, J.A. Jackson, C. Soufleris, and J. Virieux, The evolution of the Gulf of Corinth (Greece) an aftershock study of the 1981 earthquakes, *Geophysical Journal of the Royal Astronomical Society*, *80*, 677-693, 1985.

Le Pichon, X., N. Chamot-Rooke, S. Lalleman, R. Noomen, and G. Veis, Geodetic determination of the kinematics of central Greece with respect to Europe: Implications for eastern Mediterranean tectonics, *Journal of Geophysical Research*, *100* (B7), 12,675-12,690, 1995.

Leeder, M.R., and R.L. Gawthorpe, Sedimentary models for extensional tilt-block/half-graben basins, in *Continental Extensional Tectonics*, edited by M.P. Coward, J.F. Dewey, and P.L. Hancock, pp. 139-152, Geological Soceity Special Publication No. 28, 1987.

Leeder, M.R., and J.A. Jackson, The interaction between normal faulitng and drainage in active extensional basins, with examples from the western United States and central Greece, *Basin Research*, *1993* (5), 79-102, 1993.

Leeder, M.R., L.C. McNeill, R.E.L. Collier, C. Portman, P.J. Rowe, J.E. Andrews, and R.L. Gawthorpe, Corinth rift margin uplift: New evidence from Late Quaternary marine shorelines, *Geophysical Research Letters*, *30* (12), 2003.

Leeder, M.R., M.J. Seger, and C.P. Stark, Sedimentation and tectonic geomorphology adjacent to major active and inactive normal faults, southern Greece, *Jour. Geol. Soc. Lond.*, *148*, 331-343, 1991.

Lykousis, V., Sakellariou, D., Papanikolaou, Sequence stratigraphy in the n. margin of the Gulf of Corinth: implications to upper Quaternary basin evolution, *Bulletin of the Geological Society of Greece*, *32* (2), 157-164, 1998.

Martel, S.J., Mechanical controls on fault geometry, *Journal of Structural Geology*, *21*, 585-596, 1999.

McClay, K.R., and P.G. Ellis, Geometries of extensional fault systems developed in model experiments, *Geology*, *15*, 341-344, 1987.

McClusky, S., S. Balassanian, A. Barka, C. Demir, S. Ergintav, I. Georgiev, O. Gurkan, M. Hamburger, K. Hurst, H. Kahle, K. Kastens, G. Kekelidze, R. King, V. Kotzev, O. Lenk, S. Mahmoud, A. Mishin, M. Nadariya, A. Ouzounis, D. Paradissis, Y. Peter, M. Prilepin, R. Reilinger, I. Sanli, H. Seeger, A. Tealeb, M.N. Toksoz, and G. Veis, Global Positioning System constraints on plate kinematics and dynamics in the eastern Mediterranean and Caucasus, *Journal of Geophysical Research*, *105* (B3), 5695-5719, 2000.

McNeill, L., C. Cotterill, A. Stefatos, T. Henstock, J. Bull, R.E. Collier Ll, G. Papatheodorou, A. Georgiopoulou, and G. Ferentinos, A High Resolution Geophysical Study of the Offshore Western Gulf of Corinth - Preliminary Results, in *AGU Fall Meeting*, AGU, San Francisco, 2003.

Moretti, I., D. Sakellariou, V. Lykousis, and L. Micarelli, The Gulf of Corinth: an active half graben?, *Journal of Geodynamics*, *36*, 323-340, 2003.

Morley, C.K., Evolution of large normal faults: Evidence from seismic reflection data, *AAPG Bulletin*, *86* (6), 961-978, 2002.

Ori, G.G., Geologic historyof the extensional basin of the Gulf of Corinth (?Miocene-Pleistocene), Greece, *Geology*, *17*, 918-921, 1989.

Papatheodorou, G., and G. Ferentinos, Sedimentation processes and basin-filling depositional architecture in an active asymmetric graben: Strava graben, Gulf of Corinth, Greece, *Basin Research*, *5*, 235-253, 1993.

Pe-Piper, G., and D.J.W. Piper, *The Igneous Rocks of Greece: the anatomy of an orogen*, Gebruder Borntraeger, 2002.

Perissoratis, C., D.J.W. Piper, and V. Lykousis, Alternating marine and lacustrine sedimentation during late Quaternary in the Gulf of Corinth rift basin, central Greece, *Marine Geology*, *167*, 391-411, 2000.

Persaud, P., J.M. Stock, M.S. Steckler, A. Martin-Barajas, J.B. Diebold, A. Gonzalez-Fernandez, and G.S. Mountain, Active deformation and shallow

structure of the Wagner, Consag, and Delfin Basins, northern Gulf of California, Mexico, *Journal of Geophysical Research*, *108* (B7), 2003.

Pi Alperin, J.M., J.M. Marthelot, A. Galve, M. Sachpazi, B. Taylor, M. Laigle, and A. Hirn, Seismic refraction imaging of the southern Corinth rift shoulder at Derveni, *Comptes Rendus Geosciences*, *336*, 251-257, 2004.

Reilinger, R., S. McClusky, M.B. Oral, R.W. King, and M.N. Toksov, Global Positioning System measurements of present-day crustal movements in the Arabia-Africa-Eurasia plate collision zone, *Journal of Geophysical Research*, *102*, 9983-9999, 1997.

Rietbrock, A., C. Tiberi, F. Scherbaum, and H. Lyon-Caen, Seismic slip on a low angle normal fault in the Gulf of Corinth: Evidence from high-resolution cluster analysis of microearthquakes, *Geophysical Research Letters*, *23* (14), 1817-1820, 1996.

Rigo, A., H. Lyon-Caen, R. Armijo, A. Deschamps, D. Hatzfeld, K. Makropoulos, P. Papadimitriou, and I. Kassaras, A microseismic study in the western part of the Gulf of Corinth (Greece): implications for large-scale normal fault mechanisms, *Geophysical Journal International*, *126*, 663-688, 1996.

Sachpazi, M., C. Clement, M. Laigle, A. Hirn, and N. Roussos, Rift structure, evolution, and earthquakes in the Gulf of Corinth, from reflection seismic images, *Earth and Planetary Science Letters*, *216*, 243-257, 2003.

Sakellariou, D., V. Lykousis, and D. Papanikolaou, Neotectonic structure and evolution of the Gulf of Alkyonides, central Greece, *Bulletin of the Geological Society of Greece*, *32* (1), 241-250, 1998.

Shelton, J.W., Listric Normal Faults: An Illustrated Summary, *Am. Assoc. Pet. Geol. Bull.*, *68* (7), 801-815, 1984.

Sorel, D., A Pleistocene and still-active detachment fault and the origin of the Corinth-Patras rift, Greece, *Geology*, *28* (1), 83-86, 2000.

Stefatos, A., G. Papatheodorou, G. Ferentinos, R. Leeder, and R. Collier, Seismic reflection imaging of active offshore faults in the Gulf of Corinth: their seismotectonic significance, *Basin Research*, *14*, 487-502, 2002.

Vink, G.E., W.J. Morgan, and W.-L. Zhao, Preferential rifting of continents: a source of displaced terrains, *Journal of Geophysical Research*, *89*, 10072-10076, 1984.

Wessel, P., and W.H.F. Smith, New, improved version of Generic Mapping Tools released, *Eos, Transactions American Geophysical Union.*, *79* (47 (November 24)), 579, 1998.

Westaway, R., The mechanical feasibility of low-angle normal faulting, *Tectonophyiscs*, *308*, 407-443, 1999.

Westaway, R., The Quaternary evolution of the Gulf of Corinth, central Greece: coupling between surface processes and flow in the lower continental crust, *Tectonophysics*, *348* (4), 269-318, 2002.

Yilmaz, O., *Seismic Data Analysis*, 1000 pp., SEG, Tulsa, OK, 2001.

Zelt, B.C., B. Taylor, M. Sachpazi, and A. Hirn, Crustal velocity and Moho structure beneath the Gulf of Corinth, Greece, *Geophysical Journal International*, submitted.

Zelt, B.C., B. Taylor, J.R. Weiss, A.M. Goodliffe, M. Sachpazi, and A. Hirn, Streamer tomography velocity models for the Gulf of Corinth and Gulf of Itea, Greece, *Geophy. Jour. Int.*, *in press*, 2004.